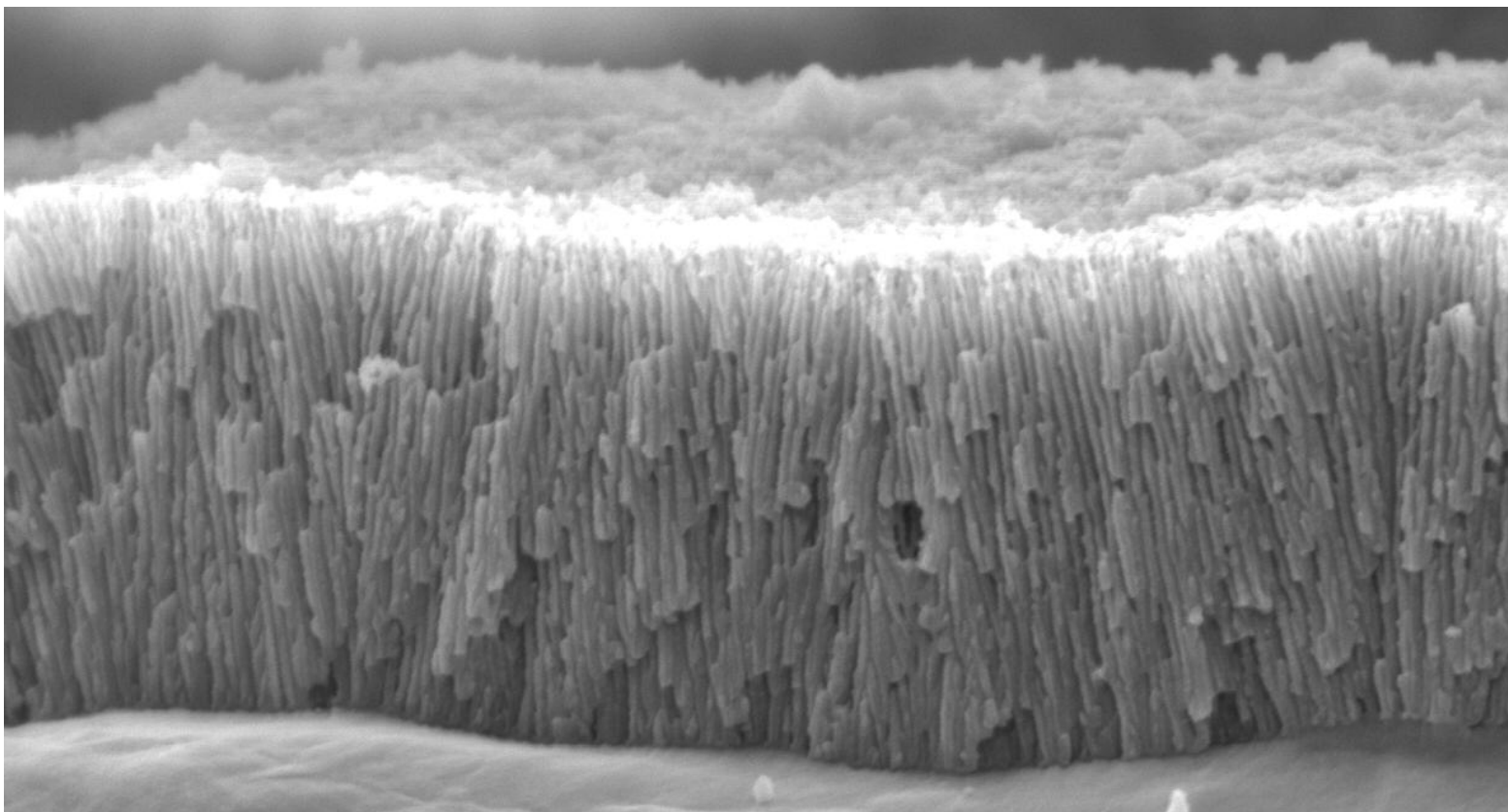




POTENTIODYNAMIC ANODIZING AND ADHESIVE BONDING OF ALUMINUM FOR THE AEROSPACE INDUSTRY

Marloes van Put
Delft University of Technology
December 2013

Supervisors: dr.ir. J.M.C. Mol,
prof.dr. H. Terryn and MSc. S. Abrahami



POTENTIODYNAMIC ANODIZING AND ADHESIVE BONDING OF ALUMINUM FOR THE AEROSPACE INDUSTRY

by

Marloes van Put



Delft University of Technology
Department of Materials Science and Engineering
Mekelweg 2, 2628 CD Delft, The Netherlands

Supervision by: dr.ir Arjan Mol, prof.dr.Herman Tarryn, and MSc Shoshan Abrahami

December 2013

ACKNOWLEDGMENTS

There are so many people I wish to thank for their support throughout this project. First of all, I would like to express my sincere gratitude to Herman Terryn, Arjan Mol and Shoshan Abrahams from the TU Delft for constant guidance and support. Your comments and feedback were always constructive and you definitely helped me to bring the work to a higher level. I had never done a large research project like this before in my life, but under your supervision I felt confident to tackle unfamiliar problems and bring the project to a good end.

Special thanks are directed to Kees Kwakernaak and Frans Oostrum from TU Delft for helping with sample coating of and SEM imaging. The same goes for Jaap Hooijmans from ECN; thank you for allowing me to make use of the surface analysis equipment at ECN. Furthermore, I want to thank Agnieszka Kooijman for her help in the lab, and all other members from the Corrosion Technology and Electrochemistry group for always being open to questions. Also, when I got stuck somewhere in the project, fellow MSE students were always willing to talk it over with me. Tjerk, thank you for dragging me away from my computer from time to time to have a cup of tea or coffee together.

It goes without saying that I would not have been able to do this project without the support of my friends and family. In particular, I want to express my gratitude to my parents Leen and Rita and my dear friends Milou, Floor, Hella, Maryam, Maaïke, Karlijn, Zinzi and Dorinde. Thank you for your constant encouragements and hearing me out when I needed it.

Last, but certainly not least, I would like to thank Bart. You were there for me the whole time and never complained when I was working long hours and messed up our apartment. Also, thank you for listening to the same stories on anodizing systems and oxide layers over and over again. You're the best!



CONTENTS

ACKNOWLEDGMENTS	v
CONTENTS	vii
INTRODUCTION	1
PART A - POTENTIODYNAMIC ANODIZING OF ALUMINUM	3
Scientific paper	4
1. Bibliography	15
1.1 Fundamentals of anodizing	15
1.2 Barrier layer formation	18
1.3 Porous film growth	19
1.4 Potentiostatic and galvanostatic anodizing	24
1.5 Potentiodynamic anodizing	25
2. Research approach	31
2.1 Aim of the project	31
2.2 Voltage and time settings	32
2.3 Overview	34
3. Experimental procedure	36
3.1 Overview	36
3.2 Materials	37
3.3 Process parameters	38
3.4 Surface Analysis	42
4. Results	44
4.1 Limitations of semi-industrial scale system	44
4.2 Current density response	46
4.3 Morphology of anodic film	50
4.4 Anodic oxide formation efficiency	59
5. Discussion	62
5.1 Expected versus measured morphologies	62
5.2 Anodic oxide formation efficiency	69
6. Conclusions part A	71

PART B- ADHESIVE BONDING OF ANODIZED SUBSTRATES	75
7. Bibliography	76
7.1 Theories of fundamental adhesion	76
7.2 Initial bond strength	77
7.3 Durability	78
8. Research approach.....	80
9. Experimental procedure	81
9.1 Overview.....	81
9.2 Materials	82
9.3 Aluminum pretreatment	82
9.4 Primer and adhesive application & curing of the system.....	83
9.5 Analysis.....	83
10. Results	86
10.1 EDX mappings of primed specimens.....	86
10.2 Bell Peel testing of bonded specimens.....	88
10.3 Bond Line Corrosion of bonded specimens	90
10.4 Overview.....	91
11. Discussion	92
11.1 Primer penetration	92
11.2 Initial bond strength.....	92
11.3 Durability of the adhesive bond.....	93
12. Conclusions part B.....	94
 GENERAL CONCLUSIONS	 96
 RECOMMENDATIONS	 100
 REFERENCES	 103
 APPENDICES	 108

INTRODUCTION

Aluminum and its alloys are widely used in the aerospace industry due to their excellent properties like low density, high mechanical strength and relatively high corrosion resistance [1]. Adhesive bonding of aluminum structures is often used to construct components for the aerospace industry. Compared to joining by mechanical fasteners, adhesive bonding increases fatigue resistance of components, improves aerodynamics and saves weight [2].

To achieve successful long-term bonding, pretreatment of the aluminum surfaces is necessary before the application of primers and adhesives. The common pretreatment procedure as it is used today consists of a number of sequential process steps, of which anodizing in chromic acid (CAA) is an important one. During anodizing, the aluminum surface is oxidized electrolytically and a thick, porous alumina (Al_2O_3) film is formed on the surface. However, the electrolyte used in the CAA process contains hexavalent chromium (Cr^{6+}) which is known to be toxic and carcinogenic [3]. Recent EU and global directives have set stringent requirements on manufacturers to ensure that the use of Cr^{6+} is phased out.

Phosphoric sulfuric acid anodizing (PSA) is considered as a promising, less hazardous alternative for the CAA process. Multiple studies have shown that PSA-pretreated films have a similar Al_2O_3 film morphology as CAA-pretreated ones, which might lead to similar strength and durability of adhesive bonds, e.g. [4]. Critchlow et al [5] also reported promising results for sulfuric acid anodizing (SAA) as an adhesive bonding pretreatment.

Previous fundamental research on anodizing has mainly focused on the formation of anodic films under constant voltage conditions (potentiostatic anodizing) or constant current density conditions (galvanostatic anodizing). However, the voltage profiles applied in industry are more complex, combining periods of constant anodizing voltage with gradual changes in voltage. The relation between potentiodynamic voltage cycles and the eventual morphology of the anodic film has not been studied yet in-depth.

Moreover, it is so far unclear what the in-depth morphology of the anodic film should look like to achieve optimum adhesive bond performance. Much work has been done on relating the outer surface morphology to adhesive bond properties, but the fundamental adhesion and corrosion mechanisms of bonded systems are not yet understood

The current project provides more insight into the growth mechanism of oxide layers during potentiodynamic anodizing. Studying the mechanism and the kinetics of oxide growth and the correlation to the anodizing process parameters is an essential step in understanding the complete system. Secondly, aluminum sheets with different anodic film variants, have been used as substrate material for adhesive bonding. Tests that are commonly used in the aerospace industry are employed to test the adhesive bond strength and resistance against corrosion. An attempt is made to relate anodic film characteristics to the performance of the adhesive bond.

This thesis is divided into two main parts. Part A focuses on the effect of a changing anodizing voltage on the morphology of anodic oxide films. Part A starts with a summary of the most important fundamental findings, written in the form of a scientific article. Part B presents a more applicative part of this work: peel testing and corrosion testing of adhesively bonded specimens.

I hope you enjoy reading this thesis as much as I enjoyed working on it.

PART A

POTENTIODYNAMIC ANODIZING OF ALUMINUM

Scientific paper

The key findings of Part A have been summarized in the form of a scientific paper. This paper is presented on the next ten pages.

Potentiodynamic anodizing of AA1050 and AA2024-T3 clad in PSA and SAA for the aerospace industry

M. van Put^a, S. Abrahami^b, J.M.C. Mol^a, H. Terryn^c

^a Delft University of Technology, Department of Materials Science and Engineering, The Netherlands

^b Materials innovation institute (M2i), The Netherlands

^c Vrije Universiteit Brussel, Department Metallurgy, Electrochemical and Surface Engineering, Belgium

Abstract

The aerospace industry progressively develops alternatives for chromic acid anodizing, since Cr^{6+} is known to be toxic and carcinogenic. In this work, anodizing of AA1050 and AA2024-T3 clad was performed in phosphoric sulfuric acid (PSA) and sulfuric acid (SAA). The electrochemical response and porous film growth was studied under potentiodynamic anodizing conditions. It was found that pore, cell and barrier layer dimensions are dependent on the anodizing voltage. Coarse morphologies were developed at higher voltages, and fine morphologies at low voltages. By changing the voltage during the process, differences in morphology were developed across the film thickness. However, the relation between voltage and pore morphology was not always linear for fast voltage changes, and less pronounced for decreasing voltages than increasing voltages due to recovery effects. Moreover, for prolonged anodizing in PSA, coarsening of the upper film part was observed, due to the high solubility of Al_2O_3 in phosphoric acid. The anodic oxide formation efficiency was therefore higher for SAA than for PSA.

1. Introduction

Aluminum and its alloys are widely used in the aerospace industry due to their excellent properties like low density, high mechanical strength and relatively high corrosion resistance [1]. Adhesive bonding of aluminum is often preferred over alternative joining methods, since it offers a higher fatigue resistance of components, improves aerodynamics and saves weight [2]. To achieve successful long-term bonding, pretreatment of aluminum surfaces is necessary before the application of primers and adhesives. Pretreatment procedures consist of a number of sequential process steps, of which anodizing often is an important one. Anodizing is an electrochemical process during which a thick oxide film is formed on the aluminum surface [6]. By appropriate selection of anodizing electrolyte and anodizing voltage or current, porous anodic oxides can be created with a duplex structure: a compact barrier layer on the bottom and a relatively regular porous structure on top [7-10], as shown in Figure 1.

Previous fundamental research on anodizing has mainly focused on the formation of anodic films under constant voltage conditions (potentiostatic anodizing) or constant current density conditions (galvanostatic anodizing). Keller, Hunter and Robinson [10] and O'Sullivan and Wood [8] have performed a tremendous amount of work studying the

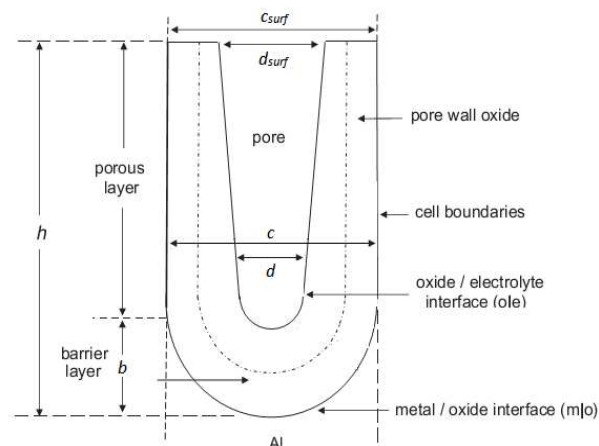


Figure 1. Schematic representation of an ideally hexagonal columnar cell of a porous anodic alumina film

effect of anodizing process parameters on the morphology of the porous layer. It was found that for high purity aluminum, the major film characteristics (pore diameter d , cell diameter c and barrier layer thickness b) are linearly dependent upon the steady-state anodizing voltage. Higher anodizing voltages lead to larger pore and cell diameters, and thicker barrier layers. Also, it has been shown by Rahman et al. [11] and Huang et al. [12] that pore diameters (measured at the outer surface) increase with anodizing time. For potentiostatic anodizing, the pore widening rate was found to be constant over the duration of the anodizing process:

$$d_{surf}(t) = d_{surf,0} + \beta \cdot t, \quad (1)$$

where d_{surf} is the outer surface pore diameter, t the anodizing time and β a linearity constant depending on the chemical nature of the alumina, the electrolyte and the process temperature.

Compared to galvanostatic and potentiostatic anodizing, relatively few researchers have looked into potentiodynamic anodizing. Curioni et al [13-15] recorded the current density response for linear polarization of aluminum in several electrolytes and linked different stages of the recorded i - V curve to growth stages of the porous oxide films. O'Sullivan and Wood [8] recorded the current response after a step-wise increase or decrease in anodizing voltage. They found that the system needs time ('recovery time') after a sudden voltage change to reach the steady state again. Also, they propose that pore widening mechanism after a voltage increase differs significantly from what happens after a voltage decrease.

However, voltage cycles including both gradual voltage changes and periods of constant voltage have not yet been studied in-depth. This is surprising, since such voltage cycles are extensively applied in practice. The most common industrial voltage cycle is the 40min 40/50V cycle, which is applied during chromic acid anodizing (CAA). An initial voltage sweep of 4V/min (linear polarization anodizing) is applied to raise the voltage in 10min to 40V, followed by a period of 20min during which the voltage remains constant. Then, the voltage is gradually increased to 50V in 5min and kept at 50V until the end of the process. It has been shown in practice that this process leads to stable, reproducible and corrosion resistant anodic oxide structures, but the oxide film growth mechanisms are not yet well understood.

The aim of the current work was to study the electrochemical response and porous film growth under potentiodynamic anodizing conditions. Seven different voltage cycles were applied. All cycles started with a linear voltage sweep, followed by a constant voltage or a dynamic voltage. It was investigated whether the linear relation between anodizing voltage and porous film dimensions is still valid under these potentiodynamic conditions. If this is the case, anodic films should be developed with a changing

morphology across the film thickness. Small pores and cells should be formed when the voltage is low, while large pores and cells should form at higher voltages. Pores that are formed first, during the initial voltage sweep, are expected to eventually be close to the film surface, since film growth occurs at the aluminum/oxide interface [7]. Consequently, each oxide film was expected to have a fine-featured surface layer (the "sweep part" of the film). This "sweep part" was expected to be thicker for slow voltage sweeps than for fast voltage sweeps, since slow voltage sweeps last longer. The morphology of the rest of the film should be constant for constant voltages, or changing proportionally to the changing voltage. The barrier layer thickness was expected to be linearly related to final anodizing voltage.

Also, the effect of anodizing time on the film morphology was investigated. It was studied whether pore diameters indeed increase with anodizing time.

2. Experimental

2.1 Potentiodynamic anodizing

Anodizing was conducted on aluminum alloys AA1050 (100x150x2.0mm) and AA2024-T3 clad (100x100x1.0mm) in phosphoric-sulfuric acid (75g/l H_3PO_4 and 50g/l H_2SO_4) and sulfuric acid (50g/l H_2SO_4) at $T=28\pm 1^\circ C$. Chemical compositions of the Al alloys are given in Table 1. Prior to anodizing, the AA1050 specimens were masked with a polymer maskant. An area of 100x100mm was cut out of the mask on both sides of the specimen to reveal the aluminum, while leaving the edges covered. AA1050 specimens were connected to a copper bar (functioning as the anode during anodizing) with two polymer joints and a coated copper wire for electrical connection. AA2024-T3 clad specimens were not masked but directly clamped in a titanium rack, to be able to anodize multiple specimens simultaneously.

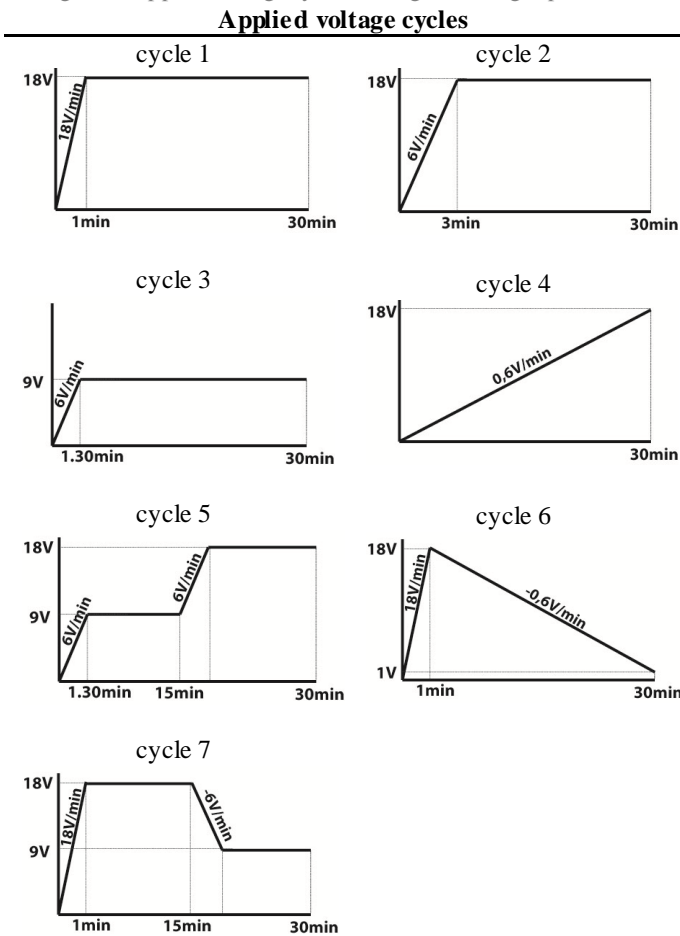
Degreasing was done in Metaclean T2001/4 VP2 (50 g/l), supplied by Chemie-Vertrieb GmbH, at $67.5^\circ C$. Degreasing was followed by etching in P3 Almeco (35 g/l), supplied by Henkel, for 5min at $35^\circ C$. After etching, any

smut present on the specimens was removed by immersion in Desoxin AL (150g/l), supplied by Enthone, for 15min at

Aluminum alloy 1050											
Element	Al	Si	Fe	Cu	Mn	Mg	Zn	Ti	others each	others total	
min. (wt %)	99.5	-	-	-	-	-	-	-	-	-	
max. (wt %)	-	0.25	0.4	0.05	0.05	0.05	0.07	0.05	-	-	
Aluminum alloy 1230 (clad layer of 2024-T3 clad)											
Element	Al	Si + Fe		Cu	Mn	Mg	Zn	Ti	others each	others total	
min. (wt%)	99.3	-		-	-	-	-	-	-	-	
max. (wt %)	-	0.70		0.10	0.05	0.05	0.10	0.03	0.03	-	
Aluminum alloy 2024 (base of 2024-T3 clad)											
Element	Al	Si	Fe	Cu	Mn	Mg	Cr	Zn	Ti	others each	others total
min. (wt%)	-	-	-	3.8	0.30	1.2	-	-	-	-	-
max. (wt %)	-	0.50	0.50	4.9	0.9	1.8	0.10	0.25	0.15	0.05	0.15

Table 1. Specifications of the chemical compositions of AA1050, AA1230 and AA2024

Figure 2. Applied voltage cycles during anodizing experiments



30°C. Etching and pickling/de-smutting steps were only included for AA2024-T3 clad specimens.

First experiments were done using a three-electrode set-up, with four stainless steel plates as counter electrodes (CE) and a Saturated Calomel Electrode (SCE) as reference electrode. The potential difference between SCE and CE was found to be only 0.15V, which can be considered negligible. The remainder of the tests was therefore done using a two-electrode cell without a SCE. The anodizing voltage cycle was programmed with an Aucos software system. Seven different voltage cycles were applied, displayed in Figure 2. The total anodizing time was 30min for all cycles. Additionally, with cycles 1, 2 and 3 treatment has been conducted for 5min and 15min. All cycles were used for AA1050 anodizing, against five cycles (2, 4, 5, 6 and 7) for AA2024-T3 clad. An XL 120 datalogger from Yokogawa was used for recording the voltage and current flow during anodizing. After anodizing, the specimens were dried in an oven at 55°C.

After each chemical treatment the specimen was spray rinsed with de-ionized water above the bath (≤ 30 sec) and subsequently immersion rinsed in de-ionized water for 4.30 min at ambient temperature. After pickling/de-smutting and anodizing, specimens were even rinsed two times 4.30min, in separate tanks.

2.2 Surface analysis

The outer surface of the anodic film was studied with a Jeol 6500-F FE-SEM. Image capturing occurred at an accelerating voltage of 5.0-6.0 keV at a working distance of 4.0-9.4mm.

Cross-sections of AA1050 specimens were obtained by making a small cut in the specimen, cooling the specimen in liquid nitrogen and breaking it manually along the cut. A Pt coating of 2nm was applied on the cross section to prevent charging. Of AA2024-T3 specimens, mirror-like cross sections were prepared by a Hitachi IM4000 ion milling system. The morphology of these cross-sections was studied with a Hitachi SEM SU-70, suitable for non-conducting samples. Image capturing occurred at an accelerating voltage of 2.0 keV, a current of 19-20 μ A and a working distance of 2.0-3.4mm. No Pt coating was applied.

For coating weight measurements, specimens were cut to a size of 75x75mm. Stripping the oxide film was done by immersing the specimen in a gently boiling ($\pm 100^\circ\text{C}$) phosphoric-chromic acid solution for 5 min. The solution consisted of 20g/l chromic acid and 35g/l phosphoric acid. Weight loss was determined with an accuracy of 0.1mg.

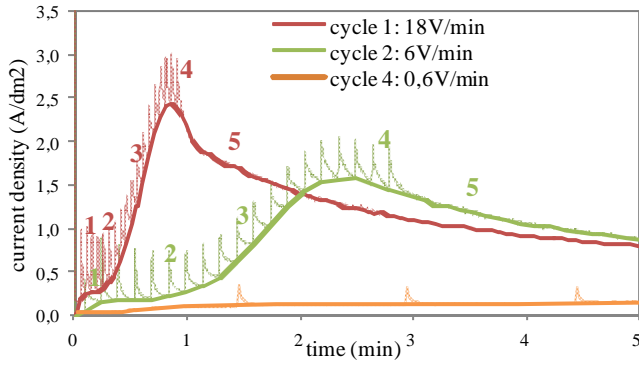
3. Results

3.1 Current density response

Figure 3 shows the recorded current densities of voltage cycles 1, 2 and 4 (first 5min), during which the voltage was raised to 18V at different sweep rates: 18V/min, 6V/min and 0.6V/min, respectively. The current density response showed a step-wise behavior during the sweep period, because the system could only increase the voltage in *steps of ± 1 V* instead of linearly. To clarify the general trend of the curve, trendlines have been drawn in the graphs (through the bottom points of the peaks). In this manuscript only these general trendlines will be discussed. As indicated in Figure 3(a), the current response of voltage cycles 1 and 2 (sweep rates 18V/min and 6V/min, respectively) consists of five different stages:

- 1) Rise in current during the first seconds.
- 2) A 'current plateau' during which the current remains constant. The plateau is found at higher current densities for 18V/min than for 6V/min.
- 3) Rise in current up to a peak value. The peak is higher and reached earlier in time for 18V/min than for 6V/min.
- 4) Slowly decreasing current just before the final voltage has been reached
- 5) As soon as the voltage has reached 18V, the current decreases exponentially until it eventually becomes constant (steady-state current).

(a) PSA - different voltage sweep rates



(b) SAA - initial voltage sweep rate (5min)

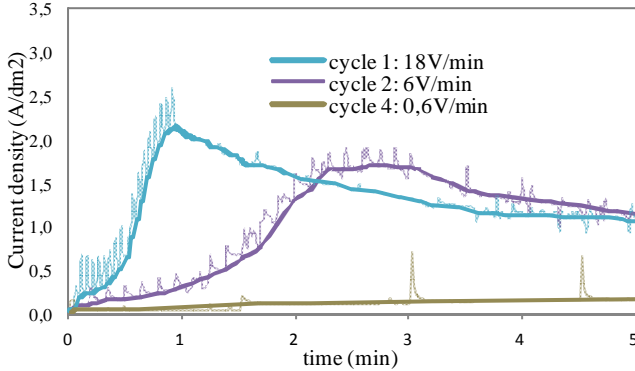


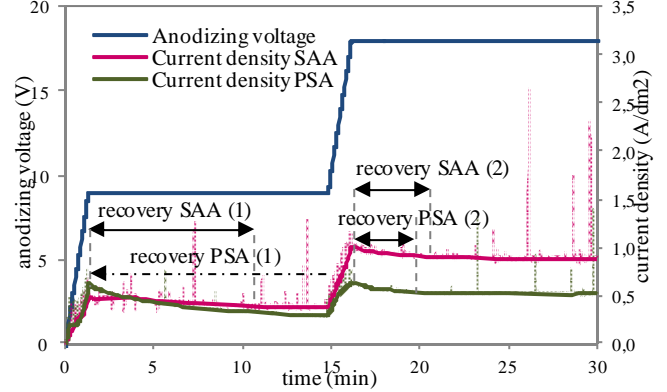
Figure 3. Different initial voltage sweep rates: current density anodizing response of AA1050 at 28°C, voltage cycles 1, 2 and 4 for 5min in (a) phosphoric-sulfuric acid and (b) sulfuric-acid

When the voltage is increased very slowly at 0.6V/min (cycle 4), no clearly defined stages are recognized in the current curve.

At the end of cycles 1, 2 and 4 ($t=30\text{min}$, $E=18\text{V}$, not visible in Figure 3) the steady-state current densities were $\pm 0.50\text{A/dm}^2$ for PSA and $\pm 0.93\text{A/dm}^2$ for SAA. The steady-state current density was thus independent of the initial voltage sweep rate. During cycles 3, 5 and 7, the steady state current density at 9V was measured and found to be $\pm 0.23\text{A/dm}^2$ for PSA and $\pm 0.38\text{A/dm}^2$ for SAA. So, steady state current densities are lower for PSA than for SAA, and current densities at 18V are more than twice as high as at 9V.

During voltage cycle 5 (Figure 4(a)) the anodizing voltage was increased from 9V to 18V (rate 6V/min) after 15min of anodizing. The current signal shows much noise, which is due to of penetration of the electrolyte under the polymer maskant during anodizing. Looking at the trend line of the current curve, it is interesting to note that no current plateau is recorded during the voltage step, while it can be observed during the initial voltage sweep. Also, the recovery time (time until steady state is reached) is much shorter after the voltage step than after the initial voltage sweep. The effect of a voltage *decrease* instead of increase is shown in Figure 4(b). The voltage decrease is accompanied by a fast decrease in current density for both PSA as well as SAA. Recovery

(a) PSA and SAA: half-way voltage step 9 → 18V



(b) PSA and SAA: half-way voltage step 18 → 9V

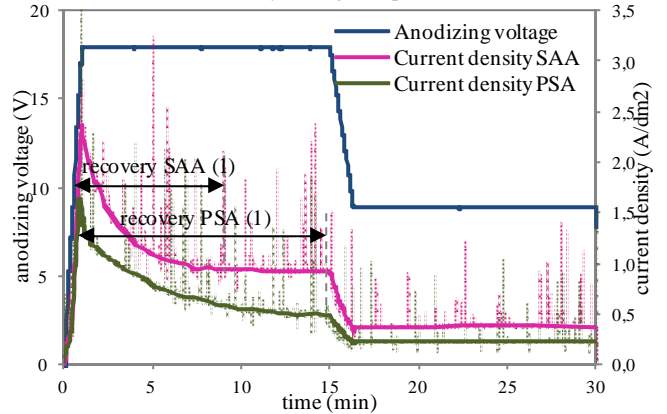


Figure 4. Half-way voltage step: potentiodynamic anodizing response of AA1050 at 28°C in phosphoric-sulfuric acid and sulfuric acid using (a) voltage cycles 5 and (b) voltage cycle 7

after the voltage decrease (18→9V) is so fast that it can hardly be recognized in the curve.

3.2 Film morphology

Figure 5 displays cross sections of anodic films on AA1050 after 30min of anodizing at 28°C, using different voltage cycles. Morphologies as obtained with PSA are shown on the left, those from SAA on the right, but note that the magnification is not the same for all images. Some general differences between the PSA- and SAA films are the following:

- SAA films are thicker than PSA films;
- SAA pores and cells are smaller than PSA pores and cells;
- the surface roughness of SAA films seems lower than that of PSA films;
- the SAA morphology is more constant throughout the film thickness.

It is especially interesting to compare the films of voltage cycle 5, Figure 5(b,e), and cycle 7, Figure 5(c,f). During cycle 7, the voltage was decreased from 18V to 9V half-way the process. The resultant film shows to exist of two distinct regions: a layer with coarse pores on top of a thin layer with

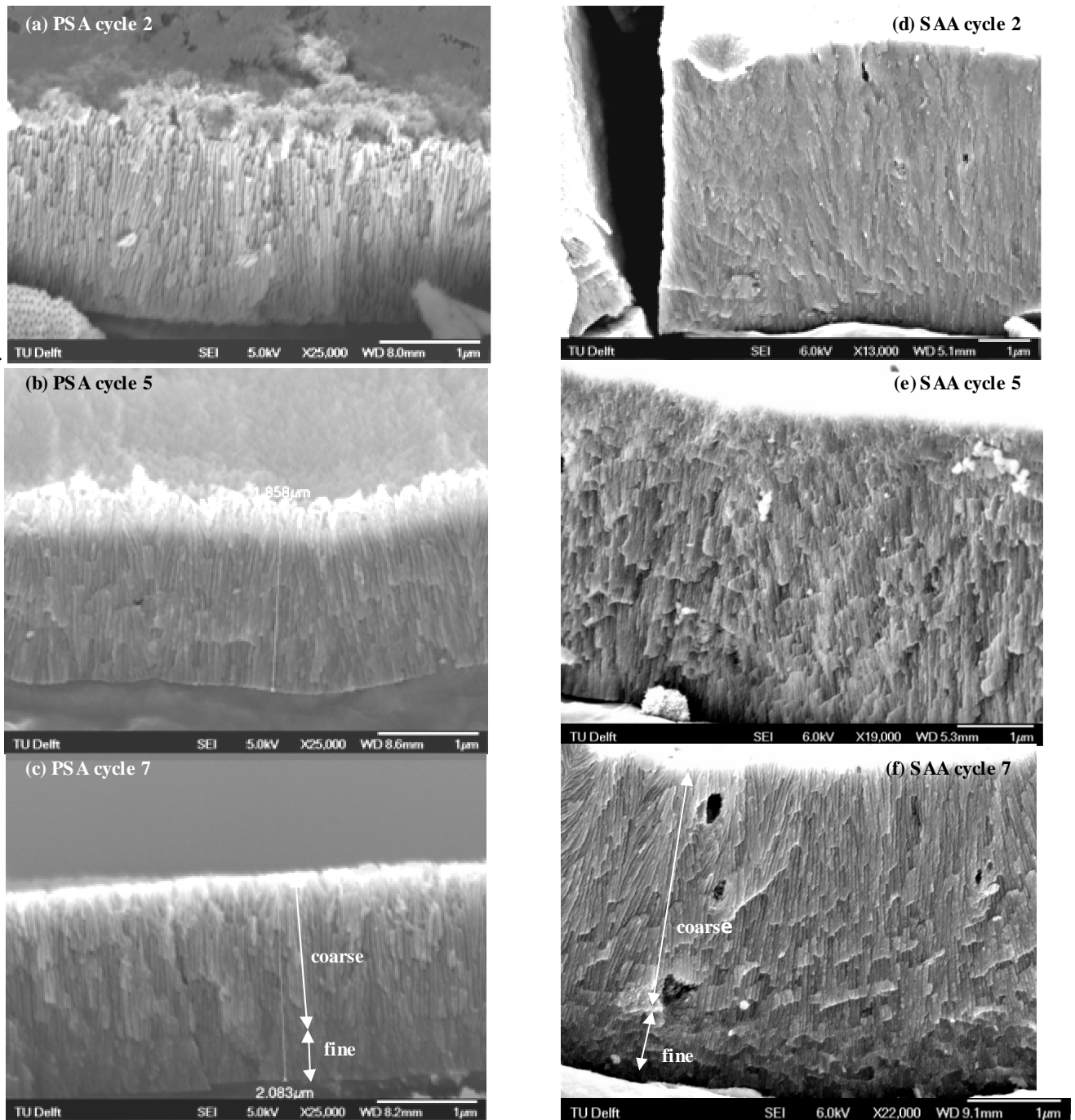


Figure 5. FE-SEM cross-sectional images of AA1050 specimens, anodized in PSA and SAA for 30min, voltage cycles 2, 5 and 7

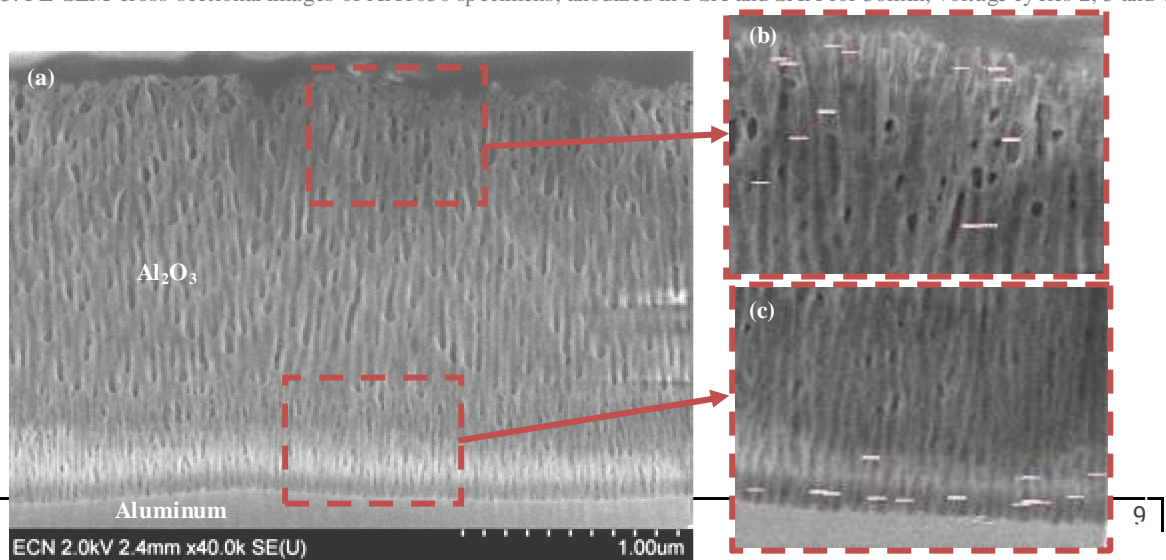


Figure 6. SEM images of ion milled cross section of AA2024-T3 clad anodized in PSA for 30min, voltage cycle 2 (a) whole layer, (b) top part and (c) bottom part

Table 2. Morphological features measured from AA2024-T3 clad film cross sections after 30min of PSA anodizing at T=28°C

Cycle nr.	Anodizing voltage			Barrier layer thickness (nm)		Pore diameter top (nm)		Pore diameter bottom (nm)		Cell diameter top (nm)		Cell diameter bottom (nm)	
	Initial sweep rate (V/min)	Average voltage (V)	Voltage at t=30min (V)	mean	σ	mean	σ	mean	σ	mean	σ	mean	σ
2	6	17,1	18	16	1	33	6	15	3	53	15	44	5
4	0,6	9,0	18	20	1	24	3	20	3	41	8	52	9
5	6	13,1	18	20	2	24	4	17	3	51	8	52	6
6	18	9,5	1	6	1	29	6	12	4	42	6	28	5
7	18	13,4	9	16	3	30	4	11	2	47	7	25	4

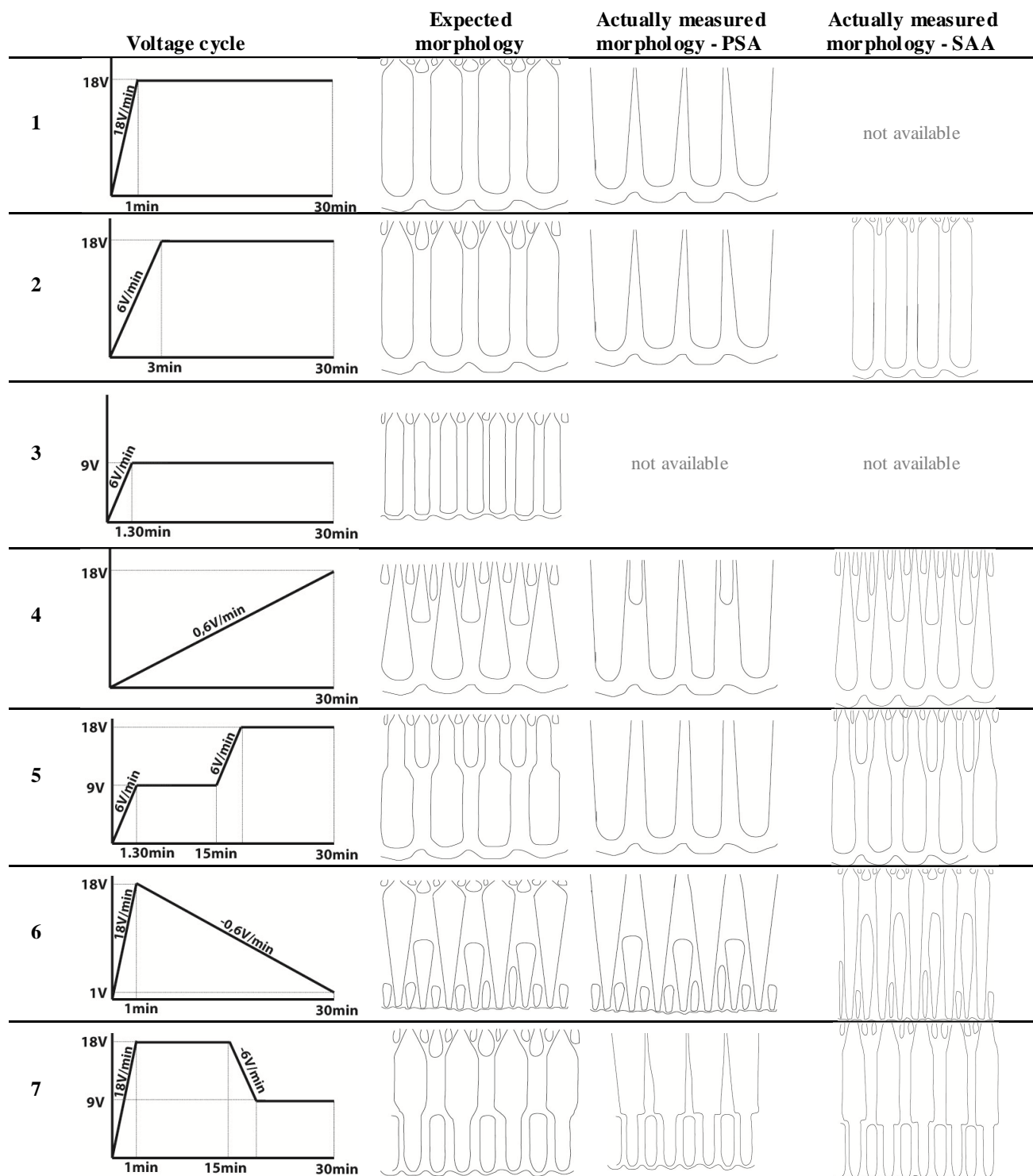


Figure 7. Expected and measured morphologies, schematic representations of anodic film cross sections

much finer pores. For cycle 5 (from 9V to 18V half-way the process), it would be logical to find a morphology opposite to that of cycle 7. However, a distinct border between a fine-featured region and a coarse region is absent for the cycle 5 film. A complete overview of expected and measured film morphologies on AA1050 for all voltage cycles is given in Figure 7. The PSA anodic film morphologies on AA2024-T3 clad showed to be very similar to those on AA1050. For instance, the ion milled cross section of the AA2024-T3 clad cycle 7 specimen is displayed in Figure 6(a). For all AA2024-T3 specimens, the image software system *AnalySiS* was used to measure pore diameters, cell diameters and the barrier layer thickness. Measurements were done at two locations: close to the outer surface and close to the barrier layer, as shown in Figure 6(b,c). Measurement data is given in Table 2.

Besides the cross section morphology, the surface morphology (top view) of all specimens was studied with FE-SEM. Pore and cell diameters as obtained with PSA on AA1050 were again similar to those on AA2024-T3 clad. When PSA is compared to SAA, differences were especially large when the anodizing time was longer. Figure 8 displays the pore and cell diameters (PSA and SAA) versus anodizing time. After 5 min of anodizing, the dimensions measured for PSA and SAA were still within the same order of magnitude (pore diameter 10-15nm, cell diameter 17-27nm). For prolonged anodizing, however, PSA dimensions increased significantly, while SAA dimensions remained the same. The ‘pore widening effect’ in PSA is more pronounced for voltage cycles 1 and 2 (final voltage 18V) than for voltage cycle 3 (final voltage 9V). Similar trends were observed for the cell diameter vs time, so the cell diameter was dependent on time for PSA, but independent of time for SAA.

PSA and SAA: pore diam vs time

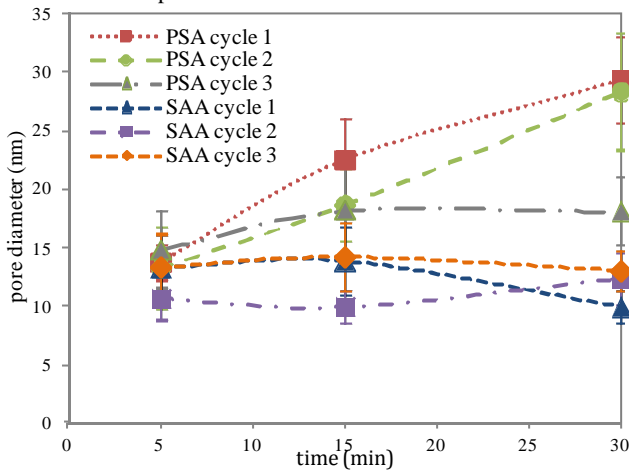


Figure 8. Pore diameter at outer surface of AA1050 vs anodizing time for PSA and SAA, voltage cycles 1, 2 and 3. Error bars represent $\pm 1 \sigma$.

PSA: pore diam vs anodizing voltage & sweep rate

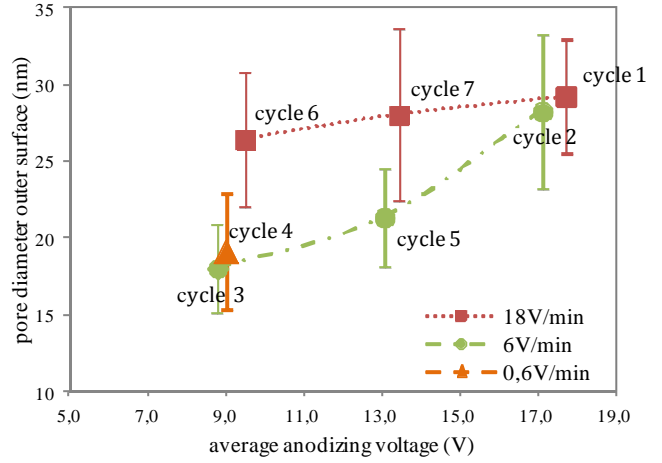


Figure 9. Pore diameter after 30 min PSA anodizing of AA1050 vs. the average anodizing voltage during a cycle. Error bars represent $\pm 1 \sigma$.

In Figure 9, PSA pore and cell diameters after 30 min of anodizing are plotted against the average anodizing voltage during a cycle. The initially applied sweep rate of a cycle (18V/min, 6V/min or 0.6V/min) is also indicated. Like observed before in Figure 8, pore diameters were larger when the average voltage was higher. However, the initial voltage sweep seems to play even a bigger role. All specimens that were anodized with an initial voltage sweep of 18V/min have larger surface pores and cells than the other specimens (6V/min and 0.6V/min initial sweep rates). Again, a similar relation was found for PSA cell diameters.

For SAA, the relation between surface morphology and anodizing voltage is not displayed. Differences between pore and cell diameters of the different samples were so small that it could not be identified whether differences were due to measurement errors or due to changing process parameters.

3.3 Anodic oxide formation efficiency

The anodic oxide formation efficiency η_{ox} is the ratio of the measured film mass to the theoretical mass calculated from the charge passed:

$$\eta_{ox} = \frac{m_2 - m_3}{\eta_{charge} \cdot \frac{M_{ox} \cdot Q(t)}{n_{ox} \cdot F}} \quad (2)$$

where m_2 and m_3 are the weights of the specimen after anodizing (g dm^{-2}) and after oxide removal (g dm^{-2}), respectively, η_{charge} the charge efficiency, M_{ox} the molar mass of Al_2O_3 (102 g mol^{-1}), $Q(t)$ the cumulative charge transferred per dm^2 , n_{ox} is the number of electrons associated with oxide formation (6) and F is the Faraday's constant (96500 C mol^{-1}). Since for small anodizing systems the charge efficiency η_{charge} is usually close to 1.0, this value will be used for further calculations. For calculation of SAA

efficiencies, both the charge and coating weight were determined from AA1050 specimens. For calculation of PSA efficiencies, however, the charge passed Q during an AA1050-run was used while the coating weight was measured on an AA2024-T3 clad specimen. This is not ideal, but since current densities as well as anodic films on both alloys have shown to be almost identical, this procedure will give a very good indication of the 'real' efficiencies. As shown in Figure 10, the anodizing efficiency of SAA-anodizing is much higher than that of PSA-anodizing, for all voltage cycles. Also, it was found that the anodizing efficiency is positively related to the average anodizing voltage of a cycle. However, when the voltage cycle includes a period of decreasing voltage, the efficiency is always lower than when the voltage is increased, even though the average voltages are equal. This is clearly seen when cycle 4 is compared to cycle 6, and cycle 5 to cycle 7.

PSA and SAA: efficiency vs anodizing voltage

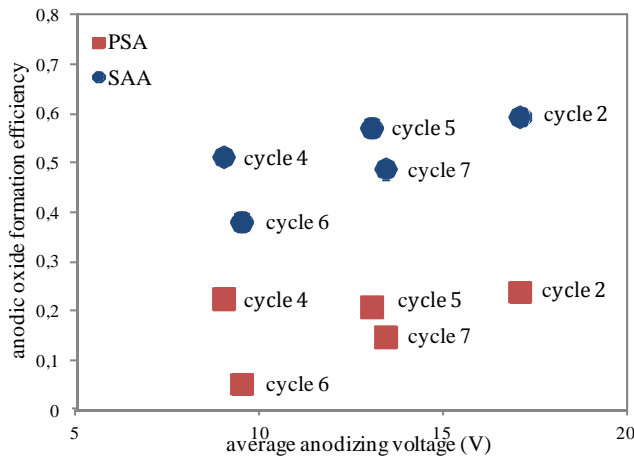


Figure 10. Anodic oxide formation efficiencies versus the average anodizing voltage, for PSA and SAA, anodizing time 30min

4. Discussion

For SAA anodizing, a high resemblance was found between expected and measured film morphologies (Figure 7). The only significant difference is found in cycle 5, where the expected 'transition layer' between the coarse region and the

fine region is absent. For PSA films, little resemblance is observed for all cycles. Only the bottom film sections - close to the barrier layer - are in most cases consistent with the predictions. As for the outer surface morphology it was expected for pore diameters to increase linearly with anodizing time. This showed to be the case for PSA, but not for SAA (Figure 8). The same was found for the effect of anodizing time on surface cell diameters.

Since the only difference between PSA and SAA is the presence of phosphoric acid in the electrolyte, differences are likely to be caused by dissolution of the outer pore walls in phosphoric acid. Previous work has shown that the chemical dissolution rate of Al_2O_3 depends on the concentration of phosphoric acid in the electrolyte [16]. In contrast, the solubility of Al_2O_3 in sulfuric acid has found to be very low [17]. The fact that both pore diameters and cell diameters increase with time, indicates that pore walls do not only get thinner but completely dissolve in the electrolyte. If only pore wall thinning would occur, the distance between two pores would not be changing (Figure 11). Oxide film dissolution in phosphoric acid thus causes complete or partial disappearance of the fine-featured section that was formed during the initial voltage sweep.

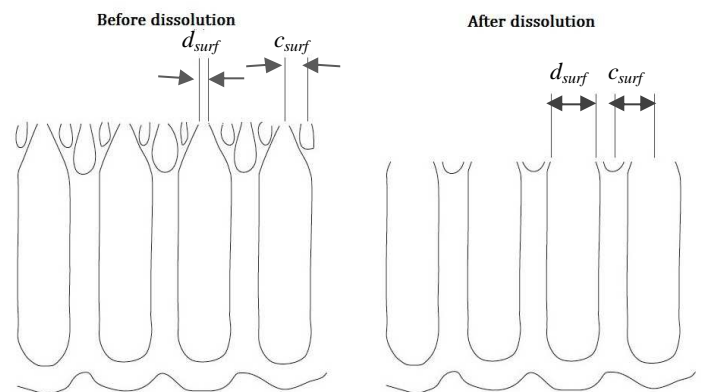


Figure 11. Dissolution of outer pore walls in phosphoric acid after prolonged anodizing in PSA

Since film growth occurs at the aluminum/film interface, the recently formed bottom part of the anodic film has been in contact with the electrolyte only for a very short

Table 3. Anodic oxide formation efficiencies

Anodizing voltage				Electro-lyte	Material	Coating weight m_{ox} (mg/dm ²)	Charge passed Q (C/dm ²)	Anodic oxide formation efficiency η_{ox} (%)
Cycle nr.	Initial sweep rate (V/min)	Average voltage (V)	Voltage at t=30min (V)					
2	6	17,1	18	PSA	AA2024-T3 clad&AA1050	46.2	1092	24
2	6	17,1	18	SAA	AA1050	98.0	1719	59
4	0,6	9,0	18	PSA	AA2024-T3 clad&AA1050	21.4	537	23
4	0,6	9,0	18	SAA	AA1050	40.3	819	51
5	6	13,1	18	PSA	AA2024-T3 clad&AA1050	31.8	864	21
5	6	13,1	18	SAA	AA1050	65.5	1195	57
6	18	9,5	1	PSA	AA2024-T3 clad&AA1050	8.0	841	5
6	18	9,5	1	SAA	AA1050	31.8	870	38
7	18	13,4	9	PSA	AA2024-T3 clad&AA1050	22.6	866	15
7	18	13,4	9	SAA	AA1050	64.8	1383	49

period and is, as such, less affected by dissolution. This explains why PSA films resemble expected morphologies more in the bottom section than in the top section.

In literature, different opinions exist on the influence of the electric field on the oxide dissolution rate. It was suggested by some that the dissolution rate increases in the presence of a high external electric field at the tips of pores [8, 18], but experimental evidence for this has not been demonstrated [19]. Though no electric field strengths were calculated in this study, the results do suggest that the dissolution rate depends on the anodizing voltage, so most probably on the electric field as well. Faster pore widening was namely observed for cycles with a high average anodizing voltage.

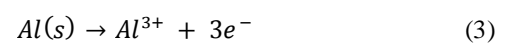
However, the initial voltage sweep rate showed to influence pore and cell diameters even more than the average anodizing voltage. For all cycles with an 18V/min or 6V/min initial voltage sweep followed by a period of constant voltage, the *i-t* curve consisted of several different stages (Figure 3). Based on previous work by Ha and Jeong [20] and Curioni et al [13], it is proposed that the current plateau stage represents barrier layer growth, and pores are thus not yet present at this point. This is evidenced by the fact that a current plateau is only seen during the first voltage sweep and *not* when a second voltage sweep is applied half-way the process. As soon as the current plateau ends, pore formation is thought to commence. For PSA anodizing, the current plateau of an 18V/min sweep ends at $t \approx 12\text{sec}$ at an anodizing voltage of 4.4V. For a 6V/min sweep the current plateau ends at $t \approx 41\text{sec}$, also at an anodizing voltage of 4.4V. Differences in outer pore diameter are thus not caused by a difference in pore formation voltage. A more reasonable explanation is that slower voltage sweeps last longer, which makes that a thicker part of the anodic film is formed during the sweep period. These 'sweep parts' of the anodic film exist of smaller pores and cells than the rest of the film, since they are formed at lower voltages. A thin sweep part is dissolved quicker in the electrolyte than a thick sweep part. So, pore widening due to dissolution is expected to be less pronounced for low initial voltage sweep rates than for high initial sweep rates.

Now, voltage cycles 5 and 7 will be discussed. O'Sullivan and Wood [8] previously described that immediately after a fast voltage change ($dV/dt \rightarrow \infty$), the barrier layer is thinner or thicker than its equilibrium value. Therefore, the current will temporarily exceed or drop below the steady state value. The barrier layer needs to grow thicker or dissolve in the electrolyte, before the current can stabilize again. Also, pore diameters have to adapt to the new voltage. Pore widening after a voltage increase is proposed to happen through dissolution of the pore base, with coalescence of the growing pores which reduces the

number of pores and increases the pore diameter. On the contrary, no mechanism exists for decreasing pore sizes after a voltage decrease. This means that new pores with smaller diameters have to develop below existing pores. Considering the current density response curves and film cross sections of voltage cycles 5 and 7, O'Sullivan and Wood's ideas correspond to the gradual voltage changes of 6V/min applied in this study. After an increase in voltage, a gradual transition is observed between the 9V- and 18V-region, since pores are slowly widened by dissolution. Such a transition region in the morphology is not seen after a decrease in voltage, since the pore diameter of existing pores remains unaltered after a voltage change. Once the barrier layer has become thinner, new pores with a smaller diameter begin to grow below the larger existing pores. A clear border thus develops between the pores formed at 18V and those at 9V.

In previous studies, e.g. [8], recovery times were found to be much shorter after a voltage increase than after a voltage decrease. The process of barrier layer thickening (oxide growth) was thought to be several orders of magnitude faster than barrier layer thinning (oxide dissolution) [21]. In this study the opposite was found: recovery times were longer after an increase in anodizing voltage instead of after a decrease. Possibly, when the process starts with a voltage of 9V, the pores are so small that electrolyte flow within the pores is difficult. When the voltage is subsequently increased to 18V, diffusion of water and oxygen towards the barrier film/electrolyte interface is limited, which slows down anodic film growth and increases the recovery time. In previous studies the anodizing voltages, and thus pore diameters were much higher so diffusion limits probably did not play a role. Limited diffusion of electrolyte in the pores might also explain why the recovery time is longer for SAA (small pores) than for PSA (large pores) after a half-way voltage step. After the initial voltage sweep, however, the recovery is longer for PSA. This could be due to higher oxide dissolution rate of anodic oxide in PSA, which makes that the system initially needs more time to find the balance between oxide growth and oxide dissolution.

If the film growth rate is high compared to the rate of dissolution, the efficiency of anodic oxide formation is high. The current density is a direct measure of the oxide growth rate, since it represents the number of aluminum atoms being transformed into the corresponding cations, according to [22]:



The more aluminum cations are available for anodic film production, the faster the anodic film grows. When the anodizing voltage is high, the current density is usually also

high. However, it was suggested that the oxide dissolution rate depends on the anodizing voltage. The results of this study indicate that the effect of an increased voltage is larger on the oxide growth rate than on the oxide dissolution rate. Otherwise, the anodic oxide formation efficiency would not be higher for increasing anodizing voltages.

The recovery effect could be an explanation for the lower efficiency of processes including a voltage decrease instead of a voltage increase. After a decrease in anodizing voltage, the current density was temporarily lower than the steady state value. For an increase in anodizing voltage, the opposite was found. On average, the current density of the whole process is thus lower when the process includes a voltage decrease, leading to a lower oxide growth rate.

5. Conclusions

This work has shown that anodic film morphologies can be 'customized' in sulfuric acid (SAA) and phosphoric-sulfuric acid (PSA) by choosing specific anodizing process parameters. It was found that pore, cell and barrier layer dimensions are dependent on the anodizing voltage. At high voltages coarse morphologies were formed, compared to fine morphologies at low voltages. However, the relation between voltage and porous dimensions was not always linear under potentiodynamic anodizing conditions. A recovery period, during which the current density was temporarily lower or higher than the steady-state value was observed after fast voltage changes. In contrast to results previously found by other authors, the recovery effect was more pronounced after a voltage increase than after a voltage decrease. The high solubility of Al_2O_3 in phosphoric acid also significantly affected the film morphology. For prolonged anodizing, coarsening of the upper film part was observed for PSA, but not for SAA. The amount of coarsening showed to be dependent on the initial voltage

sweep rate. When the initial voltage sweep is very fast, the 'voltage sweep part' of the oxide (composed of small pores, formed at low voltages) is thought to be very thin. Thin 'sweep parts' are dissolved quicker than thick 'sweep parts', which could explain the more pronounced pore widening effect at the outer surface for high voltage sweeps. Since film growth occurs at the aluminum/film interface, the bottom part of the anodic film had been in contact with the electrolyte only for a very short period and was, as such, less affected by dissolution. Finally, it was found that the anodic oxide formation efficiency was higher for SAA than for PSA. This can again be attributed to the fast oxide dissolution rate of Al_2O_3 in phosphoric acid. The anodizing efficiency was also positively related to the average anodizing voltage of a cycle. However, when the voltage cycle includes a period of decreasing voltage, the efficiency is always lower than when the voltage is increased, even though the average voltages are equal. This is due to recovery effects, since the current density is temporarily lower than the steady state value after a voltage decrease, compared to a temporarily higher current after voltage increases.

Acknowledgements

The authors gratefully acknowledge Ing. C. Kwakernaak (TU Delft), F.G.C. Oostrum (TU Delft) and dr. Jaap Hooijmans and coworkers (ECN) for valuable help in making SEM images, and J. Koning (Fokker Aerostructures BV) for helpful discussion.

References

For a list of references, the reader is referred to the end of this report (pages 103-107).

1. Bibliography

1.1 Fundamentals of anodizing

1.1.1 Electrochemical process

Aluminum has an inherent resistance to atmospheric corrosion due to the presence of a protective oxide (Al_2O_3) or hydroxide ($Al_2O_3 \times H_2O$) on the surface. This native oxide film is about 2,5 to 10nm thick [23]. Anodizing is an electrochemical process during which a much thicker oxide film (several μm) is formed [6]. This is done by placing an aluminum part in an electrolyte and contacting it to the anode of an electrical circuit, while a counter electrode in the electrolyte is contacted to the cathode, see Figure 12. The cathode is a plate or rod of carbon, lead, nickel, stainless steel or any other electronic conductor that is inert in the anodizing electrolyte.

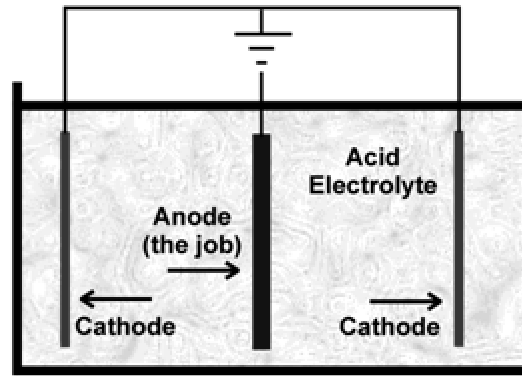
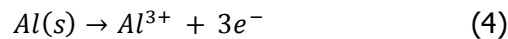
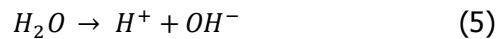


Figure 12. A typical anodizing cell [24]

When a current is passed through the cell, the aluminum is anodically polarized. This leads to anodic dissolution of aluminum to form the corresponding cations [22]:



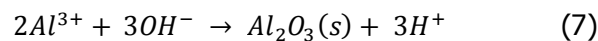
Negatively charged anions from the electrolyte migrate to the anode. In aqueous solutions those anions usually contain oxygen, formed by dissociation of water molecules:



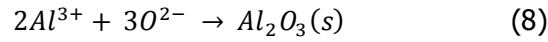
and



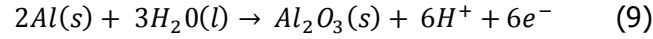
The possible reactions between the aluminum cations and oxygen-containing anions are given by:



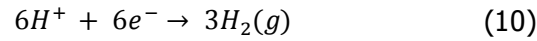
and



The net reaction of oxide growth at the anode electrode is usually given as follows:



The generated hydrogen anions move to the cathode which leads to the evolution of hydrogen gas:



1.1.2 Barrier-type film vs. porous-type film

The first important theory concerning the mechanism of anodic oxidation was put forward by Setoh and Miyata in 1932 [9]. Already in those early years it was shown that, depending on the anodizing conditions, both non-porous and porous oxide films can be produced. A non-porous film (Figure 13(a)) is often called a barrier film and is thin, strongly adherent and practically non-conducting. Barrier films are formed when the anodic oxide is essentially insoluble in the electrolyte [1, 7].

Porous-type anodic films (Figure 13(b)) have a duplex structure with a compact barrier layer on the bottom and a relatively regular porous structure on top [7-10]. Porous anodic films can be created when the anodic oxide is sparingly soluble in the electrolyte [1, 7]. For adhesive bonding, porous oxide layers are generally preferred, so the focus in this report will be only on porous anodic films.

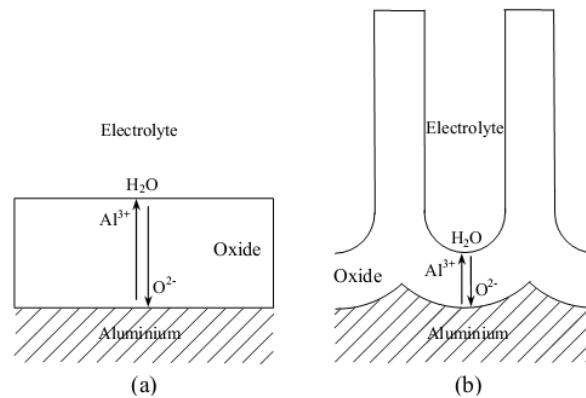


Figure 13. Schematic representation of the cross section of (a) a barrier-type anodic film and (b) a porous-type anodic film [25]

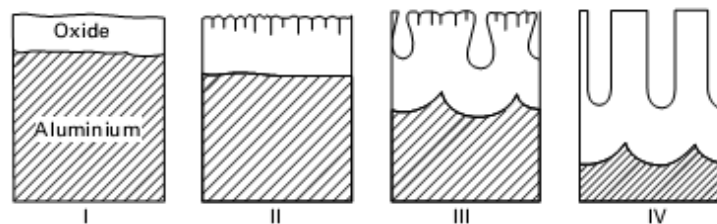


Figure 14. Four growth stages of porous-type anodic films [26]

The growth process of porous anodic films can be divided in four growth stages [1, 22, 26] as illustrated in Figure 14:

- 1) Barrier layer formation
- 2) Pore initiation
- 3) Pore formation
- 4) Steady-state growth

More details on these growth stages will follow in §1.2-§1.5

1.1.3 Commonly applied electrolytes

Many types of electrolytes can be used for anodizing; acidic, alkaline or relatively neutral pH salt solutions all belong to the possibilities. Choosing the right electrolyte is essential to achieve the desired anodic film characteristics. For the formation of porous oxide layers, acidic electrolytes are generally preferred [22, 27] to facilitate oxide dissolution and thus pore formation.

Chromic acid anodizing (CAA) was developed in 1923 by Bengough and Stuart. They were the first ones to patent an anodizing process for protecting aluminum and its alloys from corrosion [28].

Phosphoric Acid Anodising (PAA) is also extensively used in aerospace applications [29, 30]. PAA was introduced by Boeing as a pre-treatment for adhesive bonding in the mid 70's [31, 32]. Numerous studies have compared the performance of CAA and PAA bonded joints. It is generally regarded that CAA bonded joints perform better than PAA when exposed to corrosive environments. Nevertheless, the American aerospace sector still prefers the PAA process [33], since the US government has already set rules for minimizing the amount of Cr^{6+} in the 1970's.

Anodizing in sulfuric acid is also possible. Worldwide, sulfuric acid anodizing (SAA) even is the most widely used solution to produce anodic coatings [1, 34]. However, SAA is not yet applied as a pretreatment for adhesive bonding, because the pore diameters of SAA-oxides are generally smaller than those of CAA- and PAA-oxides. Sulfuric acid anodizing is generally called out for decorative purposes [35], where the anodic oxide layer serves well as a base for dye application. Nevertheless, Yendall and Critchlow [33] have recently shown that SAA could be a possible replacement for CAA when choosing the right process parameters.

Within the Airbus chrome-free program, phosphoric sulphuric acid anodizing (PSA) was developed as an alternative process for chromic acid anodizing for structural bonding [36]. The first publication on PSA originates from 1993 [37], when Koch from the Deutsche Aerospace Airbus GmbH filed a patent for the process. In the patent, it is explained that PSA films have a morphology similar to that of CAA-formed oxides. It lies in-between the thick, densely packed SAA oxide and thin, open PAA-oxide.

1.2 Barrier layer formation

1.2.1 Electric field during barrier layer formation

As soon as a voltage is applied to the anodizing cell, a potential gradient over the air-formed oxide film is set-up, giving rise to a constant electric field [38]:

$$E = -\frac{d\varphi}{dh}, \quad (11)$$

where φ is the potential difference across the film and h is the film thickness (Figure 15). Potential differences at the metal/film and film/electrolyte interfaces are neglected in Figure 15.

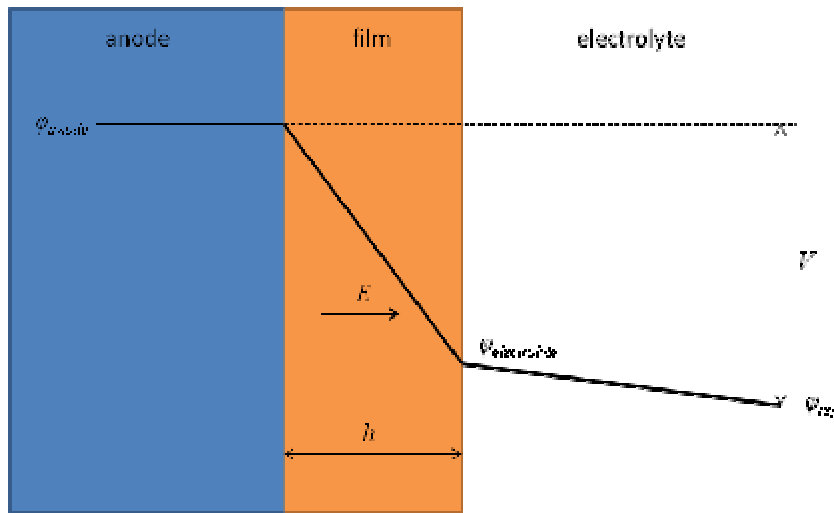


Figure 15. Potential profile of an ideal anodic film

The actual potential difference across the film is called the *anodic potential* or *anodic voltage* ($\varphi_{anode} - \varphi_{electrolyte}$). The potential difference that you apply to the whole cell is called the *anodizing potential* or *anodizing voltage*. The anodizing voltage is larger than the anodic voltage due to potential losses at the interfaces and in the electrolyte.

Since the electronic conductivity of aluminum oxide is very low, the driving force for film growth is high field ionic conduction (anion and cation transport). The relationship between the ionic current, i , and the strength of the electric field, E , may be expressed by the Guntherschultze-Betz equation [39]:

$$i = A \cdot \exp(BE), \quad (12)$$

assuming that the electric field strength is high enough to prevent movement of cations against the field direction. A and B are temperature- and metal-dependent parameters. For aluminum oxide, the electric field E and parameters A and B are in the range of 10^6 to 10^7 V/cm, 1×10^{-16} to 3×10^{-2} mA/cm² and 1×10^{-7} to $5,1 \times 10^{-6}$ cm/V, respectively [40].

1.2.2 Thickness of barrier layer

The thickness of the barrier layer is found to depend linearly upon the potential drop across the oxide [8]. The anodizing ratio is defined as the oxide thickness formed per anodizing volt (nm/V) [41]. In aggressive, pore-forming electrolytes, the anodizing ratio decreases with temperature and even more with acidity of the electrolyte [8], see Table 4.

Phosphoric acid concentration (M)	Electrolyte temperature (°C)	Anodizing ratio at constant voltage (nm/V)
0.4	20	1.14
0.4	25	1.09
0.4	30	1.04
0.4	25	1.09
1.5	25	1.04
2.5	25	0.82

Table 4. Variation of barrier layer thickness with acid concentration and temperature for constant voltage PAA-anodizing [8]

1.3 Porous film growth

1.3.1 Pore initiation and formation mechanism

At a certain point, growth of the barrier layer terminates and pores start to form in the anodic oxide film. The morphology of the barrier layer beneath the pores changes from a flat layer into a scalloped layer as shown in Figure 16. The electric field distribution in the scalloped barrier oxide at pore bases is inhomogeneous [26]. The maximum electric field becomes concentrated at the pore centre and decreases towards the pore walls (Figure 16).

The role of the inhomogeneous electric field with respect to the pore initiation and formation mechanisms is still unclear. Earlier theories suggest that the generation of pores is due to rapid, thermally assisted dissolution of the alumina enhanced by the high electric field at the pore base [27]. More recent theories are proposed by Zhu et al., who associate the porous structure with evolution of oxygen [42, 43], and Garcia-Vergara et al., who suggest that the generation of pores arises from the field-induced flow of alumina from the pore bottom towards the cell walls, driven by compressive stresses between neighboring cells [44, 45].

Terryn [46] found that the initiation of incipient pores is related with the aluminium substrate morphology, induced by the pretreatment process. For rolled aluminium, pore initiation occurs above lines present on the rolled surface. Because of this, pores have a linear arrangement at the outer surface of the oxide film (Figure 17).

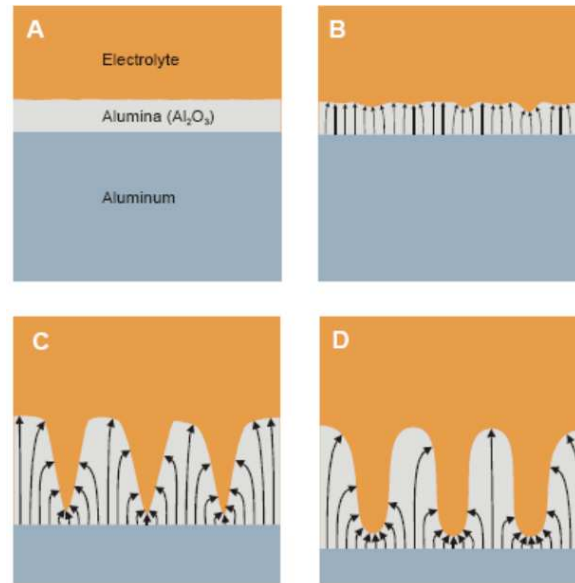


Figure 16. Electric field distribution during different stages in development of anodic alumina film

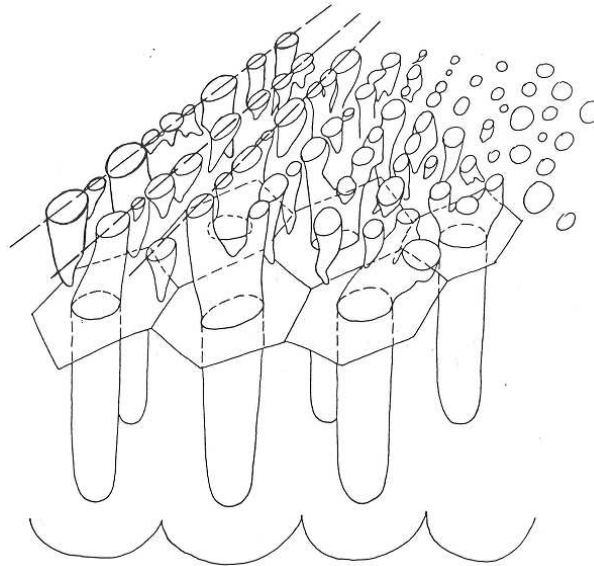


Figure 17. Schematic representation of porous film on rolled Al [46]

It is beyond the scope of this literature review to discuss all existing theories on pore initiation and formation. In general, it can be stated that many aspects of the chemical reactions and transport processes during anodizing have been identified, but that the initiation and self-assembly of pores are not yet well understood [47].

1.2.2 Location of film growth

There has been done considerable work investigating whether film growth occurs at the metal/film interface, at the film/electrolyte interface or within the film. Two concepts are of main importance when determining the location of film growth.

Firstly, the growth location depends on the ionic transport processes within the oxide film. If outward migration of Al^{3+} cations through the film is dominant, growth is more likely to occur at the film/electrolyte interface. If inward migration of oxygen-bearing anions is dominant, film growth is more likely to occur at the metal/film interface [7].

Marker and tracer studies performed by the UMIST group [48, 49] have shown that not just the cations or just the anions are mobile in the film, but that both oxygen bearing ions and aluminum ions move simultaneously through the anodic film (Figure 18). As for the oxygen bearing ions, O^{2-} is found to be more mobile in the film than OH^- [6, 27].

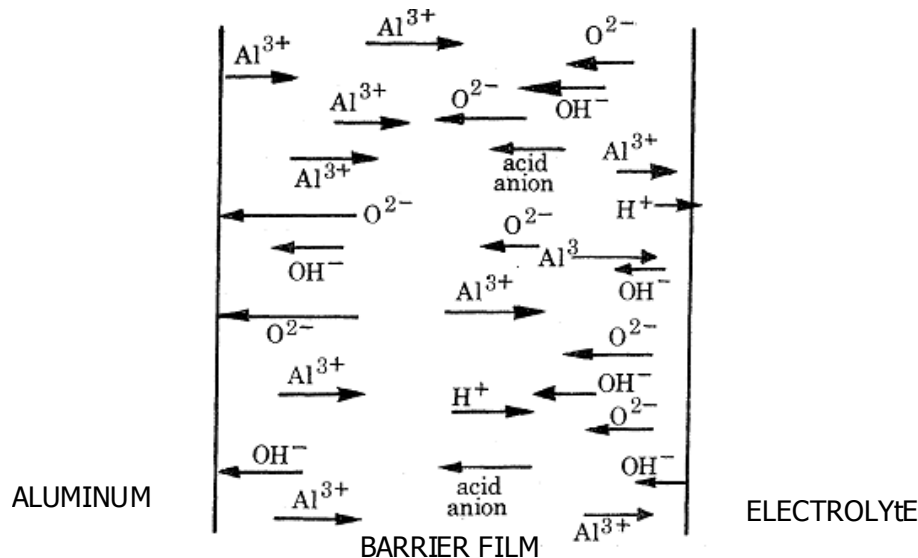


Figure 18. Sketch illustrating ion transport through the oxide film [8]

Secondly, the location of film growth is determined by the current efficiency [7] or anodic oxide formation efficiency. The current efficiency is defined as the ratio of the amount of aluminum oxide generated to the charge passed [50]. A low current efficiency practically means that many outwardly migrating aluminum ions are directly ejected to the electrolyte and as such do not contribute to the oxide growth [14]. The lower the pH of the electrolyte, the more easily aluminum ions are ejected to the electrolyte and the lower the current efficiency. The same behavior is revealed for anodizing at low current densities [7].

When the pH and current density reach a critical low value, alumina film material only develops at the metal-film interface through O^{2-}/OH^- ingress. Al^{3+} cations that move outwardly mobile are now directly ejected to the electrolyte, so no solid alumina is formed at the film-electrolyte interface [7].

1.3.2 Morphology of porous layer

The morphology of a porous anodic film is defined by the cell diameter, pore diameter, shape of the pore, height of the pore and the barrier layer thickness (Figure 19).

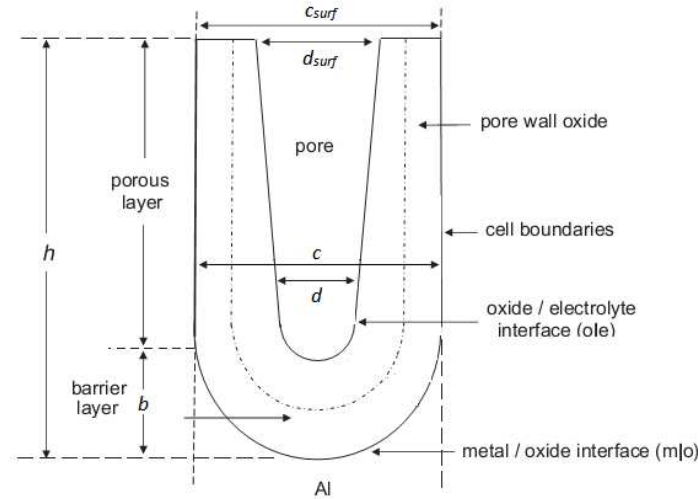


Figure 19. Schematic representation of an ideally hexagonal columnar cell of a porous anodic alumina film [27]

Keller, Hunter and Robinson [10] and O'Sullivan and Wood [8] have performed a tremendous amount of work studying the effect of anodizing process parameters on the morphology of the porous layer. It was found that for high purity aluminum, the major film characteristics (pore diameter d , cell diameter c and barrier layer thickness b) are directly dependent upon the steady-state anodizing voltage:

$$d = \delta * V \quad (13)$$

$$c = \varepsilon * V \quad (14)$$

$$b = \gamma * V \quad (15)$$

in which V is the anodizing voltage and γ , δ , and ε proportionally constants. The values of γ , δ , and ε depend slightly on temperature and electrolyte, but not on the aluminum substrate morphology [8, 10, 46, 51]. For instance, for anodizing of electropolished aluminum in 0,4M phosphoric acid at 22°C, it was found that $\delta = 0,80\text{nm/V}$, $\varepsilon = 2,71\text{nm/V}$, and $\gamma = 0,96\text{nm/V}$ [8]. For rolled or electrograined instead of electropolished aluminum, almost identical values were found [46].

However, when anodizing in an aggressive electrolyte, the morphology of the film may be variable across the film thickness due to attack of the outer surface by the acid [6]. The pore diameters at the outer surface will in such a case be larger than predicted by O'Sullivan and Wood's relations due to dissolution of pore walls in the electrolyte. This 'pore widening' effect becomes more pronounced for higher electrolyte temperatures [52]. The chemical nature of the electrolyte and the alumina also play an important role [11].

It has been shown that for anodizing at a constant voltage, the pore widening rate is constant over the duration of the anodizing process. In other words, the pore diameter increases linearly with time [11, 12]:

$$d(t) = d_0 + \beta t, \quad (16)$$

where the linearity constant β depends only on the chemical nature of the alumina and the electrolyte and on the process temperature.

The attack of the outer surface can be severe after prolonged anodizing times, such that the cells walls of the outer pores will get very thin. If these very thin filaments become too long, their stiffness will be insufficient and the filaments will tumble over, resembling a 'birds nest' [52, 53], as displayed in Figure 20(j,m,n,o) and Figure 21(j,m,n,o). The arrow in Figure 20 indicates a distortion in the film which was probably caused by temporary oxygen evolution.

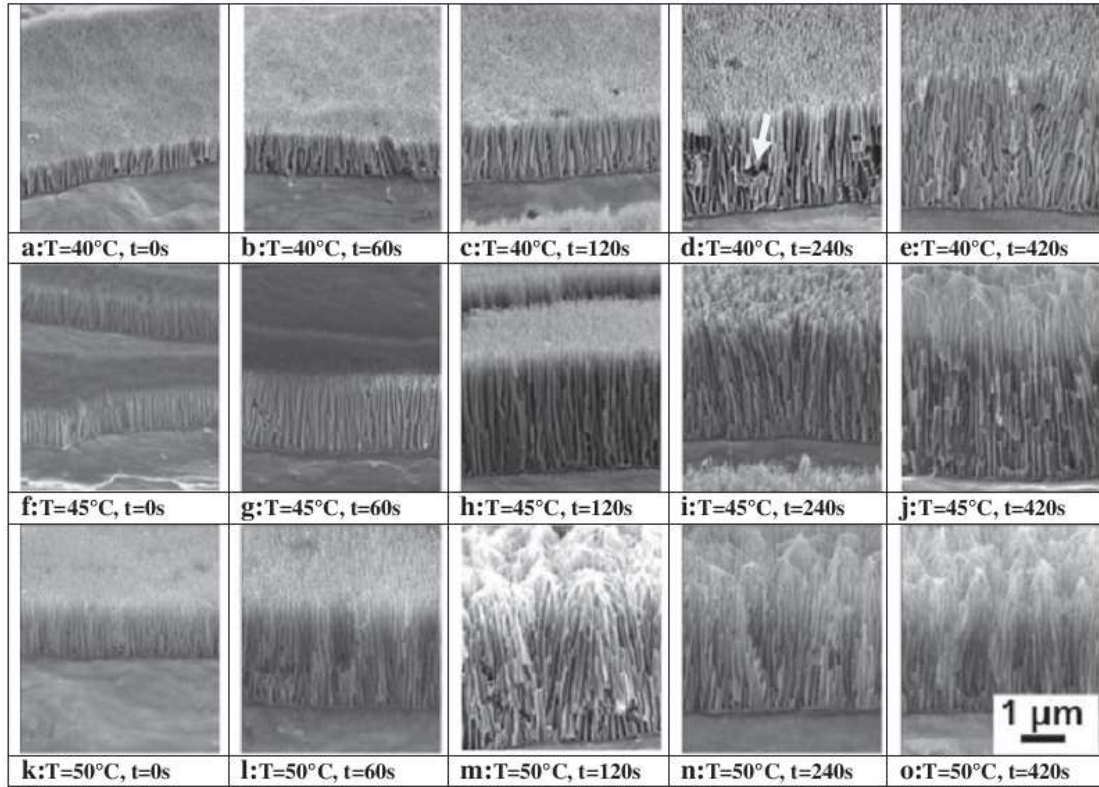


Figure 20. Morphology of oxide layer (cross sections) on AA1050 as a function of electrolyte temperature and anodizing time (anodizing voltage = 50V) [52]

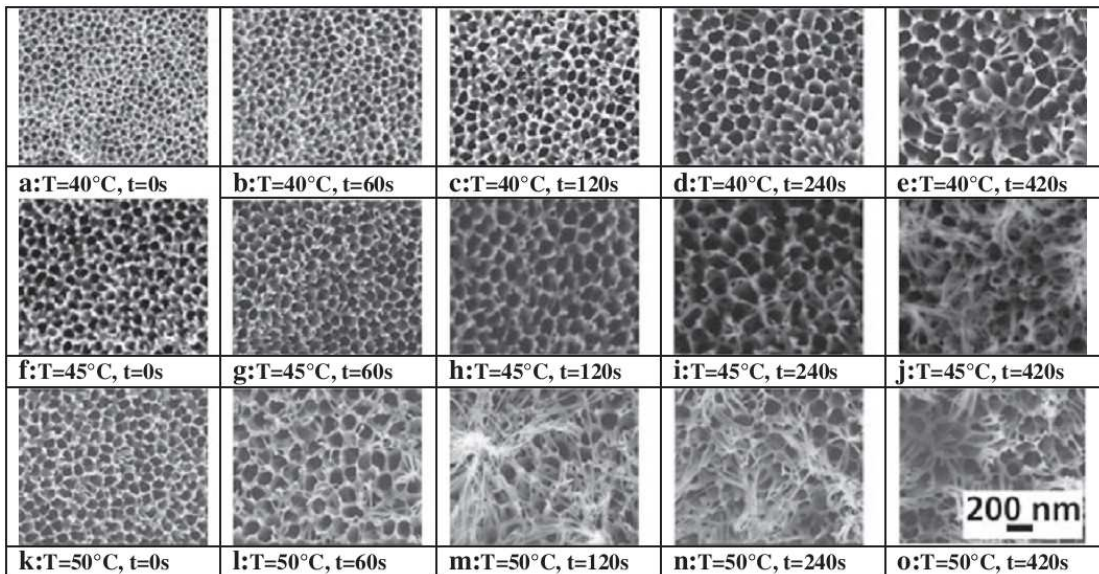


Figure 21. Morphology of oxide layer (top surface) of PAA-anodized aluminum (20 w t% H_3PO_4) depending on electrolyte temperature and anodizing time (anodizing voltage = 50V) [52]

1.4 Potentiostatic and galvanostatic anodizing

Typically, the anodizing process is studied by applying a constant current density (galvanostatic anodizing) or a constant voltage (potentiostatic anodizing) on the electrochemical cell. Typical V/t or i/t curves that are recorded during galvanostatic and potentiostatic anodizing, respectively, of high purity aluminum are shown in Figure 22. These curves reveal the course of porous film development [6, 26].

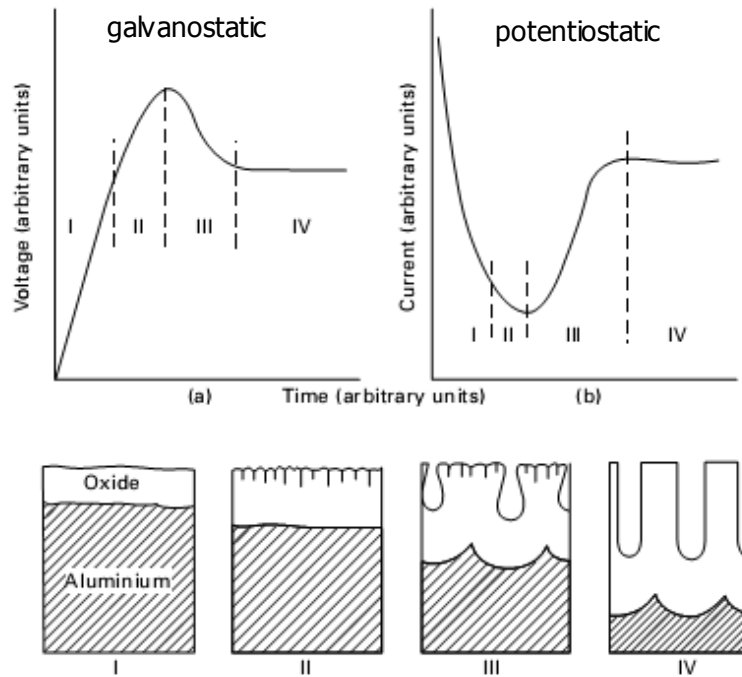


Figure 22. Schematic diagrams showing the development of porous oxide growth on aluminum during (a) galvanostatic and (b) potentiostatic anodizing [26]

During the first stage of anodization (stage I in Figure 22) a barrier film is grown on the aluminum surface. In the case of galvanostatic anodizing, the measured voltage rises linearly with time as the relatively compact film thickens uniformly with time [7]. Similarly, for potentiostatic anodizing the current decreases linearly with time during the initial thickening of the oxide, as a result of the oxide's increasing resistance.

At a certain point in time, growth of the barrier layer terminates and pores start to form in the anodic oxide film (stage II in Figure 22). The onset of pore formation can be recognized in the curve as the point from which the linear relation ceases [46]. The curve then slowly moves towards a maximum (galvanostatic anodizing) or minimum (potentiostatic anodizing) [54].

Further anodizing results in the development of penetration paths through the barrier layer the formation of pores (stage III in Figure 22). The electric field concentrates beneath these pores and the voltage decreases again (galvanostatic anodizing) or the current flow rises (potentiostatic anodizing).

The final stage (stage IV in Figure 22) is the quasi-steady state stage in which the oxide film steadily grows thicker. Since only the pore walls elongate and the barrier layer thickness does not change during the quasi-steady state stage, it is expected that the electrical resistance and anodic potential (for galvanostatic anodization) over the oxide

film remain constant. In reality, however, the anodic potential sometimes slightly rises with time in the final stage, as has been shown for instance by Abdel Rahim [27]. A possible explanation for this is the limited flow of electrolyte within long pores [20], limiting the amount of oxygen available for oxide growth.

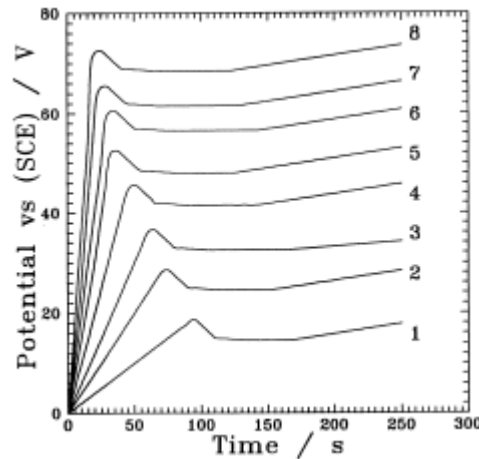


Figure 23. Galvanostatic anodization of aluminum in 1,0 M sulfuric acid at 30°C and at different current densities: (1) 5, (2) 15, (3) 25, (4) 35, (5) 45, (6) 75, (7) 65 and (8) 55 mA cm⁻² [55].

1.5 Potentiodynamic anodizing

Anodizing under potentiodynamic conditions means that the anodizing voltage is changed during the process. Anodizing in industrial environments is mostly performed in this way. One, or multiple, voltage ramps (also called: sweeps) are applied to slowly raise the potential to the desired level. As such, the risk of extremely high initial current flow is minimized.

Despite the extensive application of potentiodynamic anodizing in practice, relatively few studies are available on the growth of anodic films under potentiodynamic conditions [14]. This is especially surprising since the part of the oxide that develops during the initial voltage sweep will eventually be at the outer surface of the anodic layer – provided no dissolution occurs. As such, this part of the oxide will be in contact with the adhesive primer later on.

1.5.1 Linear polarization anodizing

Figure 24 shows the current response recorded by Curioni et al. [14] for linear polarization anodizing of high purity aluminum. Curioni et al. stopped the process at each voltage level and made TEM images of the films at each point. As such they were able to link the different stages seen in the i/V curve to growth stages of the porous oxide films:

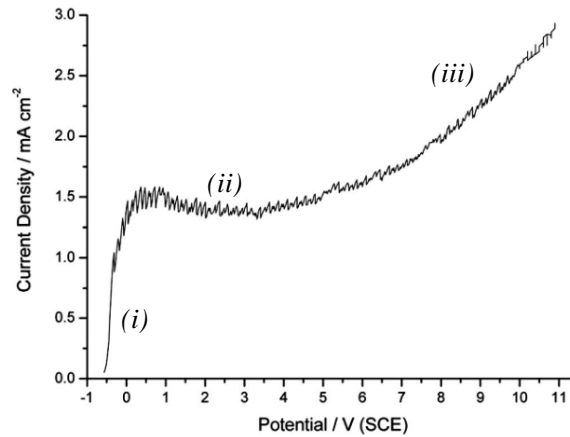


Figure 24. *I-V* response of high purity aluminum in 0.46 M H₂SO₄ under potentiodynamic conditions: linear polarization anodizing at a sweep rate of 14.4 V/min [14]

- During stage (i), the current rises rapidly due to ionic conduction across the thin, pre-existing air-formed film. Aluminum ions start to move outward and oxygen ions migrate inward.
- After the initial current rise, stage (ii) commences and a 'current plateau' is seen in the *i/V* curve. Here, constant thickening of the barrier film takes place.
- As soon as pores start to form at the surface of the barrier film, the system moves from stage (ii) to stage (iii). During this final stage the barrier layer and porous layer thicken simultaneously, though not at the same rate.

For anodizing in sulfuric electrolyte, the morphology of porous anodic films formed by linear polarization anodizing is variable across the film thickness. A fine-featured morphology (small pore diameters) is found in the outer regions of the anodic film and a relatively coarse morphology (large pore diameters) in the inner regions (Figure 25) [13, 15].

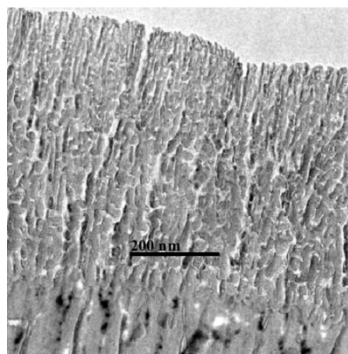


Figure 25. Transmission electron micrograph of the anodic film generated by increasing linear polarization from the OCP to 14.4 V (SCE), 1 V/min, in 0.46 M H₂SO₄ [56]

Curioni et al. [13] recently performed linear polarization experiments up to much higher voltages (>200V) in a wide spectrum of electrolytes (Figure 26). The initial current plateaus that occur at low anodizing potentials cannot be recognized in these curves due to the large scale of the graph. In some electrolytes, especially in the chromic acid, an unexpected second current plateau is found at higher voltages. The authors were not able to explain this effect.

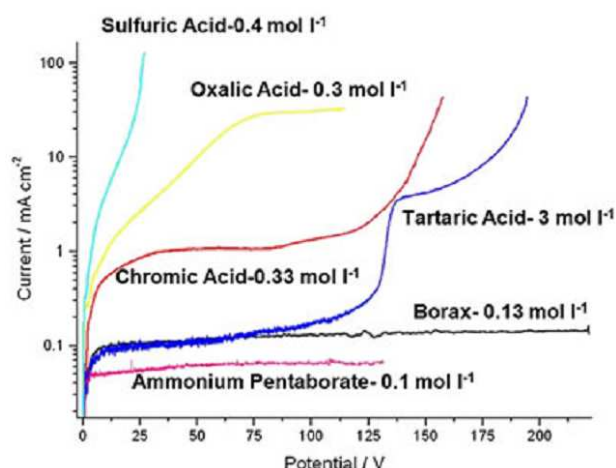


Figure 26. Linear polarization anodizing (sweep rate 1 V/min) of high purity aluminum in selected electrolytes [13]

1.5.2 A sudden change in anodizing voltage: recovery effect

O'Sullivan and Wood [8] recorded the current response after a step-wise increase in anodizing voltage (Figure 27). They first formed an anodic film at a voltage of 85V for 30min, then broke the circuit, quickly adjusted the circuit to the new voltage (115V) and completed the circuit again. The resulting film morphology is shown in Figure 28.

According to the authors, several phenomena play a role after the sudden voltage increase. First, the anodizing current increases very quickly according to the high field equation (see also §1.2.1). This leads to a higher oxide growth rate, thereby producing rapid barrier layer thickening at the oxide/aluminum interface. The barrier layer continues to thicken until it approaches the barrier layer thickness/voltage ratio. As a result of the barrier layer thickening, the current drops again as the resistance against current flow is increased. Now, the film morphology temporarily looks like the morphology shown in Figure 28. The barrier layer has thickened to its new steady state value, but pores still have diameters which are characteristic of the lower voltage. For this reason, the current has not reached its steady state value yet. Pores close to the barrier layer first have to grow larger before enough the steady state current is reached. Pore widening is proposed to be happen by field-assisted dissolution of pore walls, due to the increased electric field at the pore base. The time needed for the system to achieve its steady state again after a sudden change in anodizing voltage is called the 'recovery time' [1].

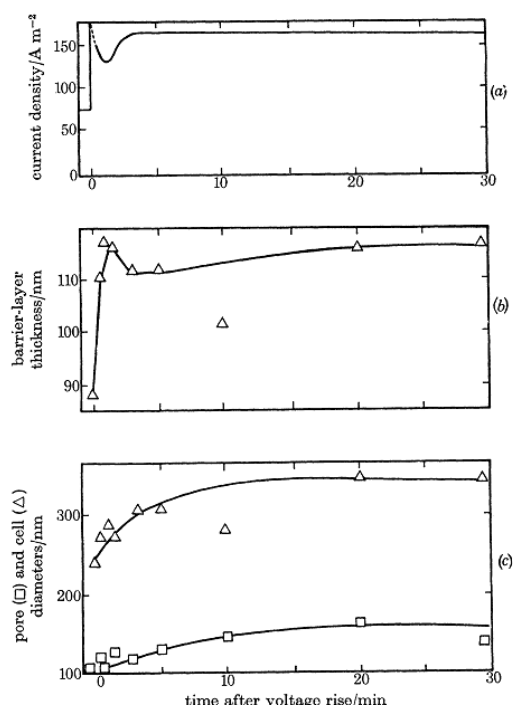


Figure 27. Effect of a sudden rise in anodizing voltage from 85 to 115V in 0,4 M phosphoric acid at 25 degr C upon (a) current density, (b) barrier-layer thickness and (c) pore and cell diameters [8]

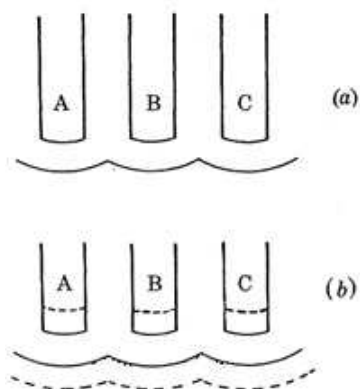


Figure 28. Schematic representation of (a) the equilibrium morphology and (b) the situation after a sudden increase in anodizing voltage, where the barrier layer has already thickened but pores have not yet redistributed [16]

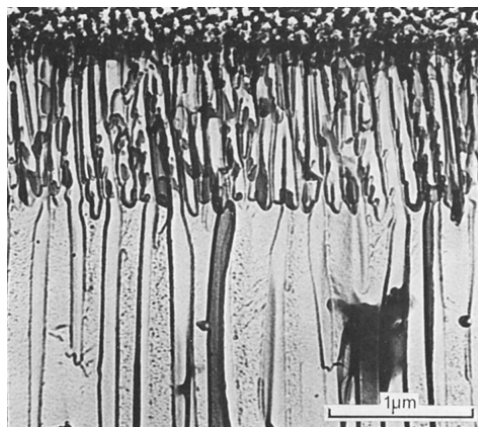


Figure 29. SEM micrograph of the section of a film grown in 0.4 M phosphoric acid at 25°C for 30 min at 85V, followed by 20min at 115V

Now, the reverse case is discussed, where the voltage is decreased instead of increased. More researchers have examined the effect of a decreasing anodizing voltage [8, 14, 56-61], compared to that of an increasing voltage

The current response measured for a sudden drop in voltage is displayed in Figure 30. Just after the voltage is dropped, the barrier layer is thicker than its equilibrium value. The resistance of the thick barrier layer is so high that current flow is blocked, so the current drops to a very low value. Barrier-layer thinning, by means of field-assisted dissolution and chemical dissolution, must first take place before substantial current can pass again.

When the barrier layer has thinned, the pore diameters are still larger than the equilibrium pore diameter. Since no mechanism exists for reducing the diameter of existing pores [8], new pores with smaller diameters have to develop below existing pores. The newly developed pores have a diameter proportional to the new anodizing voltage. As soon as small pores have been developed, the current stops increasing and reaches the steady-state value.

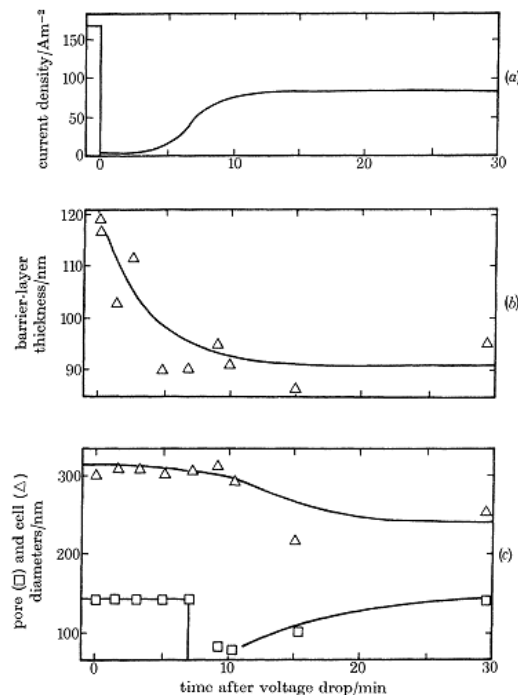


Figure 30. Effect of a sudden decrease in anodizing voltage from 85 to 115V in 0,4 M phosphoric acid at 25 degr C upon (a) current density, (b) barrier-layer thickness and (c) pore and cell diameters [1]

In the study by O'Sullivan and Wood[8], the recovery time was longer after a decrease in anodizing voltage than after an increase. According to Wernick and Pinner [1], the recovery time after a change in anodizing voltage (from V_1 to V_2) is not affected by agitation of the electrolyte nor by the thickness of the anodic coating. Factors that do effect the recovery time are the following [1]:

- The values of V_1 and V_2 as well as the difference $V_1 - V_2$
- The sweep rate dV/dt when changing from V_1 to V_2

- The concentration of the electrolyte in which the anodic coating at V_1 was formed. The concentration of the electrolyte in which recovery takes place has little effect.
- The temperature of the electrolyte in which recovery takes place.
- The treatment of the anodic coating between the time V_1 was switched off and V_2 applied.

2. Research approach

2.1 Aim of the project

Compared to *galvanostatic* (constant current) and *potentiostatic* (constant voltage) anodizing, relatively few researchers have looked into *potentiodynamic* (changing voltage) anodizing. This is surprising, since potentiodynamic anodizing is widely applied in industry. The most common cycle is the 40/50V cycle displayed in Figure 31. It starts with linear polarization anodizing, followed by a period of 40V and after a while the voltage is gradually increased again and kept at 50V until the end of the process. Statistically it has been shown that for CAA, this voltage cycle eventually leads to the best adhesive bond performance. However, no in-depth information of the influence of a dynamic voltage on the growth process is available. As discussed in §1.5, some studies are available on linear polarization anodizing or sudden increases/decreases in anodizing voltage, but no in-depth work has been found on the voltage cycles that resemble industrial cycles.

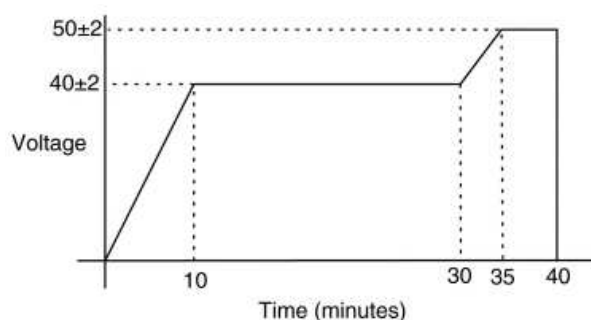


Figure 31. Time/voltage diagram of 40/50V CAA process

For *potentiostatic* anodizing, several relations between anodizing process parameters and the resultant oxide film morphology have been found by other authors. Knowing the relation between process parameters and film morphology is very useful, since it makes it possible to 'design' anodic films morphologies by choosing the right process parameters. For adhesive bonding, it is reasonable to assume that the anodic film morphology influences the corrosion resistance and bond strength of the bonded system. This will be discussed in more detail in *Part B – Adhesive bonding of anodized substrates*.

The first purpose of the present work (part A) was to test whether phenomena that have been proven for *potentiostatic anodizing* also apply to *potentiodynamic anodizing*. Based on previous work on potentiostatic anodizing [8, 10-12], two hypotheses are formulated for potentiodynamic anodizing. **These hypotheses were tested by potentiodynamically anodizing high purity aluminum in two electrolytes: sulfuric acid (SAA) and phosphoric-sulfuric acid (PSA).**

Hypotheses:

- 1) The thickness of the barrier layer, pore diameters and the cell diameters are linearly related to the anodizing voltage. Pore and cell diameters should thus be constant throughout the film thickness when the anodizing voltage is kept constant, or different across the film thickness proportionally to the changing voltage. The barrier layer thickness should be linearly related to final anodizing voltage.
- 2) 'Pore widening' effect: pore walls dissolve in the acid electrolyte after prolonged anodizing, which leads to a linear increase in pore diameter with anodizing time.

The second purpose of this work was to study the effect of a dynamic anodizing voltage on the anodic oxide formation efficiency of SAA- and PSA-anodizing. The anodic oxide formation efficiency η_{ox} is the ratio of the measured film mass to the theoretical mass calculated from the charge passed during anodizing.

The choice was made for PSA and SAA, because both are considered as promising alternatives for chromic acid anodizing (CAA) (see §1.1.3). Also, by comparing PSA and SAA it is possible to independently study the effects of phosphoric and sulfuric acid on the process.

The majority of the experiments was performed on aluminum sheet material alloy AA1050. This is a high purity alloy ($\geq 99,5$ wt% Al), which makes it unlikely that elements other than aluminum itself influence the fundamental anodizing process. The alloy AA2024-T3 clad (material of clad layer: AA1230) was also included in the test program, since this alloy is widely used in the aerospace industry. Since the composition of the AA1230 clad layer is almost identical to AA1050 (see §3.2), no significant differences are expected between the anodizing behavior of AA1050 and AA2024-T3 clad.

The morphology of anodic film cross sections was studied with the SEM. Cross sections were obtained either by breaking the specimen or by ion milling. Ion milling gives better results, but since it is an expensive and time consuming procedure only the AA2024-T3 clad specimens were selected for ion milling, since AA2024-T3 clad was used later on in the work (Part B) as a substrate for adhesive bonding tests. AA2024-T3 clad also received a more extensive pretreatment prior to anodizing to make the sheets suitable for bonding.

2.2 Voltage and time settings

Two process parameters were varied during the anodizing experiments:

- 1) voltage cycle (section 2.2.1);
- 2) anodizing time (section 2.2.2);

2.2.1 Voltage cycles

Seven different voltage cycles were applied which are displayed in Figure 32. These voltage cycles are based on common industrial voltage cycles. Voltage cycle 2 (6V/min up to 18V, total anodizing time 30min) is the cycle that Airbus currently applies during PSA anodizing, so this cycle is considered as a promising one. The effect of a faster

(18V/min) or slower (0,6V/min) initial voltage sweep was studied by means of cycles 1 and 4, respectively. By adding cycle 3 (sweep rate 6V/min up to 9V), the effect of the final voltage is taken into account as well.

During the current 40/50V process the voltage is increased from 40V to 50V after a 30min of anodizing (Figure 31), so two-step voltage cycles were included in the test matrix as well. Increasing the voltage halfway the process (cycle 5) was compared to decreasing the voltage halfway (cycle 7).

Curioni et al. [56] suggested better performance of adhesively bonded joints when negative polarization anodizing (linearly decreasing voltage) was applied. This is the reason that voltage cycle 6 was also included in the program. Due to limitations of the power supply, it was not possible to start immediately at the highest voltage, so the voltage was raised as quickly as possible (18V/min) to the final value, after which it was slowly decreased again.

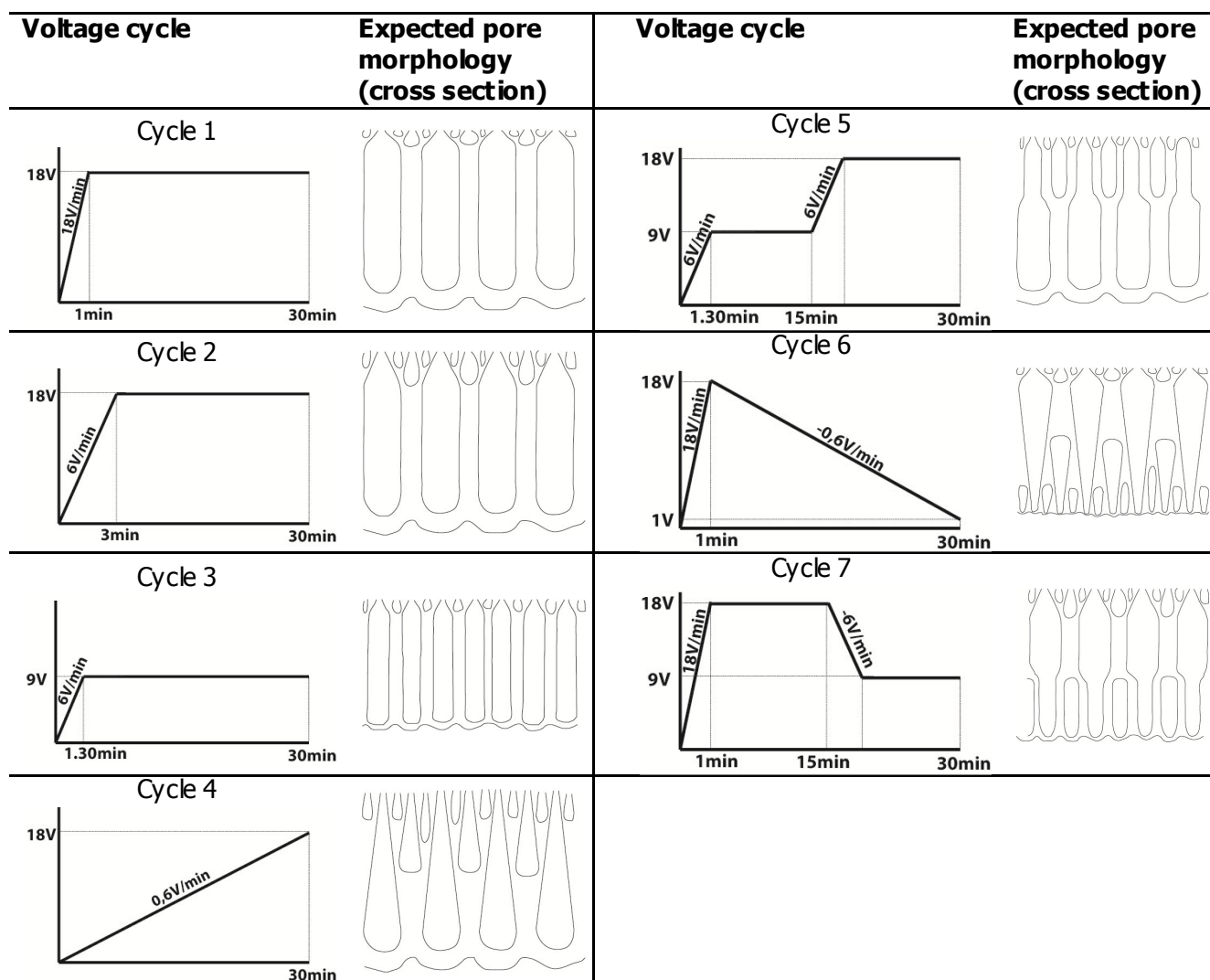


Figure 32. Applied voltage cycles and expected pore morphologies based on theory O'Sullivan and Wood

As mentioned before, it was shown in previous work [8, 10] on *potentiostatic* anodizing that the thickness of the barrier layer, pore diameter and interpore distances are linearly related to the anodizing voltage. If these relations also apply to the *potentiodynamic* processes tested in this study, the resultant pore morphologies should look roughly like

the pictures shown in Figure 32. Each film would have a surface layer with fine pores, formed during the initial voltage sweep. For lower voltage sweep rates, this surface layer would be thicker since the anodizing voltage is low for a longer period. The morphology of the rest of the film should be constant for constant voltages, or changing proportionally to the changing voltage. The barrier layer thickness should be linearly related to final anodizing voltage ($\pm 1,1 \text{ nm/V}$).

2.2.2 Anodizing time

To investigate whether the surface pore diameter increases with anodizing time voltage cycles 1, 2 and 3 were stopped after 5min, 15min and 30min to study changes in surface morphology with time.

2.3 Overview

An overview of the materials, electrolytes, voltage cycles and time settings that were used for each experiment is shown in Table 5. Also, this Table provides an overview of where to find results and discussion of each subject in the remainder of this report.

Section in report		How is the ...	Influenced by...	Applied settings															
				Voltage cycles ¹							Anodizing time (min)			Electrolyte		Al alloy			
Results	Discussion			1	2	3	4	5	6	7	5	15	30	PSA	SAA	1050	2024 ²		
4.2	5.1	ANODIZING CURRENT DENSITY	- initial voltage sweep rate					X		X			X	X	X	X			
			- half-way voltage step	X	X	X		X		X			X	X	X	X	X		
			- steady-state anodizing voltage	X	X		X						X	X	X	X	X	X	
4.3.1	5.1	CROSS SECTION MORPHOLOGY	- initial voltage sweep rate	X	X		X	X	X	X			X	X	X ³	X			
			- half-way voltage step					X		X			X	X	X	X	X		
			- stead-state anodizing voltage		X			X		X			X	X					X
4.3.2	5.1	OUTER SURFACE MORPHPHOLOGY	- initial voltage sweep rate	X	X	X	X	X	X	X			X	X	X	X	X		
			- average anodizing voltage	X	X	X	X	X	X	X			X	X	X	X	X	X	
			- anodizing time	X	X	X							X	X	X	X	X	X	
4.4	5.2	ANODIZING EFFICIENCY	- half-way voltage step					X		X			X	X ⁴	X ⁴	X ⁴	X ⁴		
			- average anodizing voltage		X		X	X	X	X			X	X ⁴	X ⁴	X ⁴	X ⁴	X ⁴	

Table 5. Overview of voltage cycles, anodizing times, electrolytes and time settings used for different experiments

¹ Voltage cycles displayed in Figure 32

² AA2024-T3 with AA1230 clad layer

³ No cross section was made of SAA-specimen voltage cycle 1

⁴ For PSA: oxide film weight after anodizing was determined from AA1230 specimens, while the charge used for calculating the theoretical oxide mass was recorded during AA1050 anodizing. For SAA

3. Experimental procedure

3.1 Overview

A schematic overview of the experimental work performed in this part of the study is given in Figure 33.

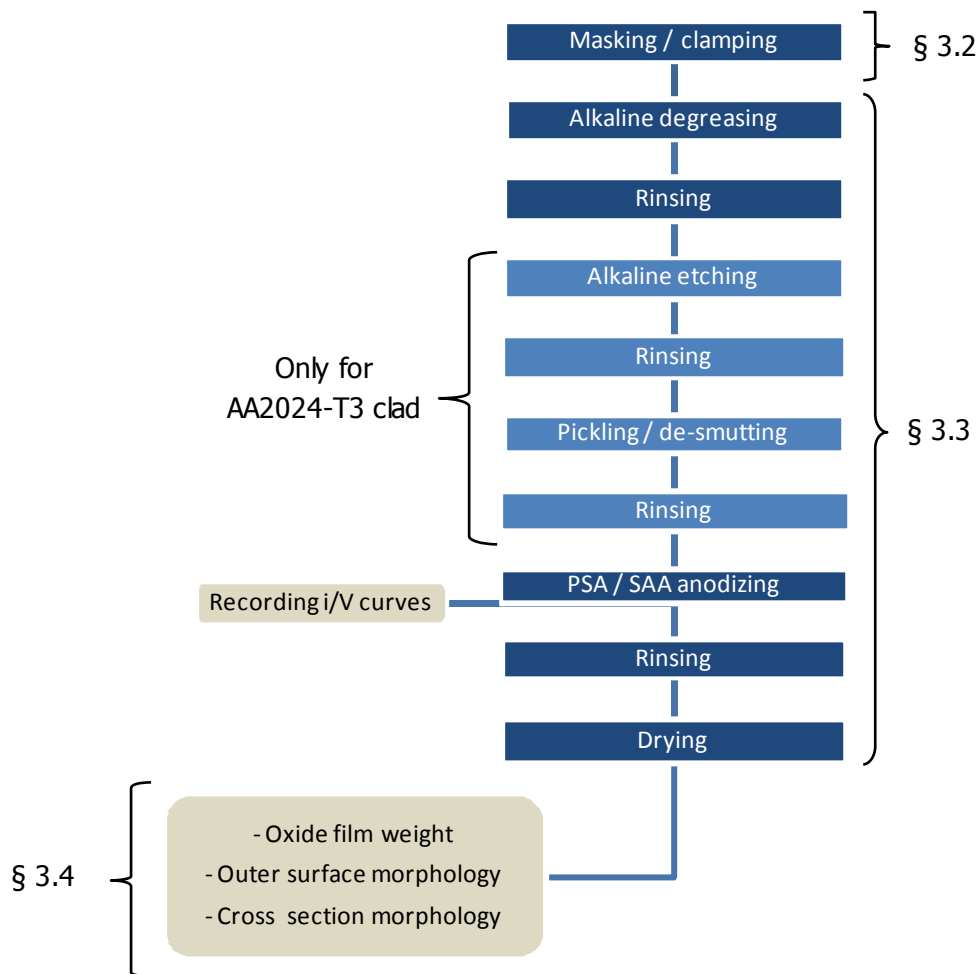


Figure 33. Overview of experimental work Part B

3.2 Materials

Tests were performed on two different aluminum alloys:

- Aluminum alloy AA1050;
 - Chemical composition: see Table 6
 - Supplier: Salomon's Metalen, Groningen
 - Batch number: unknown
 - Specimen size: 100x150x2.0mm
- Aluminum alloy AA2024-T3 clad (clad layer AA1230)
 - Chemical composition: see Table 6
 - Material specification: AIMS 03-04-014
 - Supplier: AMAG
 - Batch number: V132652569
 - Specimen size: 100x100x1.0mm

Aluminum alloy 1050											
Element	Al	Si	Fe	Cu	Mn	Mg		Zn	Ti	others each	others total
min. (wt %)	99,5	-	-	-	-	-		-	-	-	-
max. (wt%)	-	0,25	0,4	0,05	0,05	0,05		0,07	0,05	-	-
Aluminum alloy 1230 (clad layer of 2024-T3 clad)											
Element	Al	Si + Fe		Cu	Mn	Mg		Zn	Ti	others each	others total
min. (wt%)	99,3	-		-	-	-		-	-	-	-
max. (wt%)	-	0,70		0,10	0,05	0,05		0,10	0,03	0,03	-
Aluminum alloy 2024 (base of 2024-T3 clad)											
Element	Al	Si	Fe	Cu	Mn	Mg	Cr	Zn	Ti	others each	others total
min. (wt%)		-	-	3,8	0,30	1,2	-	-	-	-	-
max. (wt%)		0,50	0,50	4,9	0,9	1,8	0,10	0,25	0,15	0,05	0,15

Table 6. Chemical compositions of AA1050, AA1230 and AA2024 [62, 63]

3.2.1 Preparation of AA1050 plates

Before further processing of the AA1050 specimens, an electrical wire was connected to the top each panel. Subsequently, the specimens were masked with a one component polymer maskant. An area of 100x100mm was cut out of the mask on both sides of the specimen. The edges remained covered with the maskant material as displayed in Figure 34(b).

A layer of silicon-free maskant tape was put on the coating/aluminum interface (Figure 34(a)), to prevent electrolyte from moving under the coating. The AA1050 test plates were connected to a copper bar (functioning as the anode during anodizing) with two polymer joints. A stripped end of the electrical wire was fixed to the bar with aluminum tape (Figure 34(a)) for electrical connection.

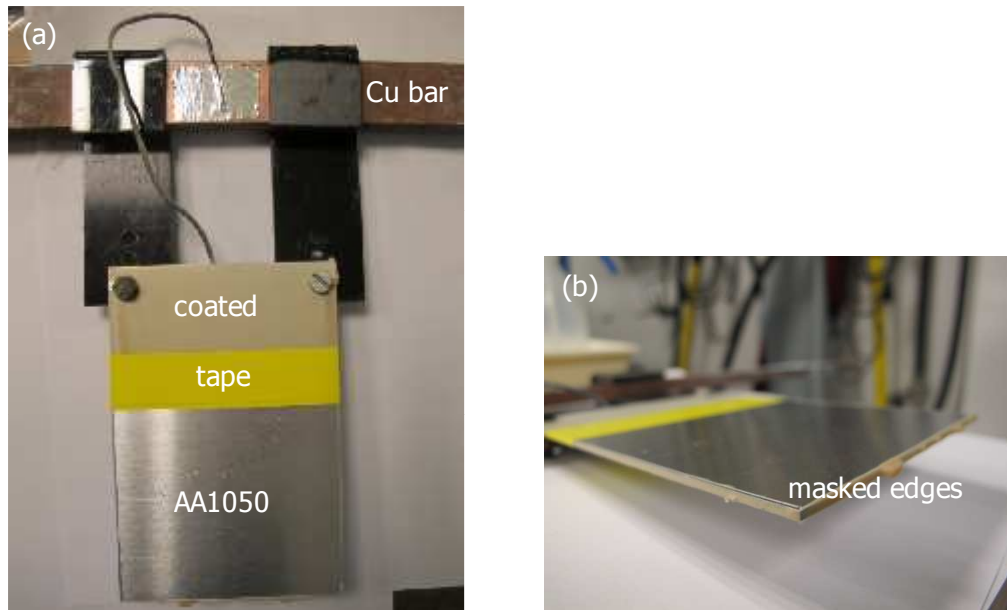


Figure 34. AA1050 specimen with 100x100mm exposed area, connected to copper bar and (b) masked edges

3.2.2 Preparation of AA2024-T3 plates

The steps undertaken for preparation of AA1050 are not applied to AA2024-T3 clad. AA2024-T3 clad specimens were directly clamped in a titanium rack as displayed in Figure 35. Per run, four AA2024-T3 panels (2 pieces 100x100x1.0mm, 1 piece 255x120mm and 1 piece 300x120mm) were pretreated simultaneously. One piece of each run (size 100x100x1.0mm) was used for study of the anodic film morphology (part B of this report) and the other three panels were used for later analysis, as will be explained in part C.

3.3 Process parameters

An overview of all the surface treatment steps, including anodizing, is given below. After each step the specimen was spray rinsed with de-ionized water above the bath (≤ 30 seconds) and subsequently immersion rinsed in de-ionized water for 4.30 min at ambient temperature. After pickling/de-smutting and anodizing, specimens were rinsed two times 4.30min, in separate tanks.

3.3.1 Degreasing

Alkaline degreasing was performed in Metaclean T2001/4 VP2 (50 g/l) at 67,5°C. Supplier of Metaclean: Chemie-Vertrieb GmbH). For AA1050 plates the degreasing time was 5min and for AA2024-T3 clad plates (in the titanium rack) 15 min.

3.3.2 Alkaline etching

Alkaline etching was included only for AA2024-T3 clad plates. Alkaline etching was done for 5 min at 35 °C in P3 Almeco 51 (35 g/l). Supplier of P3 Almeco51: Henkel, Germany.



Figure 35. AA2024-T3 clad panels clamped in titanium rack

3.3.2 Pickling/de-smutting

Pickling/de-smutting was included only for AA2024-T3 plates. Pickling/de-smutting was done for 15 min at 30°C in Desoxin AL (150 g/l). Supplier of Desoxin AL: Enthone GmbH, Germany.

3.3.3 Anodizing PSA or SAA

Anodizing was performed under potentiodynamic conditions, either in phosphoric-sulfuric acid (75 g/l H_3PO_4 and 50 g/l H_2SO_4) or in sulfuric acid (50 g/l H_2SO_4) at 28°. The anodizing time was 5min, 15min, 16.30min or 30min. A detailed test matrix, giving the time and voltage settings of each specific run, is given in Table 7.

First experiments were done using a three-electrode set-up, shown in Figure 36. In this set-up the aluminum specimen functioned as the working electrode (WE), four stainless steel plates as counter electrodes (CE) and a Saturated Calomel Electrode (SCE) as reference electrode. The SCE was placed close to, but not in contact with the working electrode. It was found that the potential between SCE and CE was only 0,15V, which can be considered negligible. The remainder of the tests was therefore done using a two-electrode cell without a SCE.

The anodizing voltage cycle was programmed and recorded with a software system. Since the data acquisition rate of this software was very low, a separate datalogger (type XL 120 from Yokogawa) was used for recording the voltage and current flow during anodizing. The datalogger registered one to five data points per second.

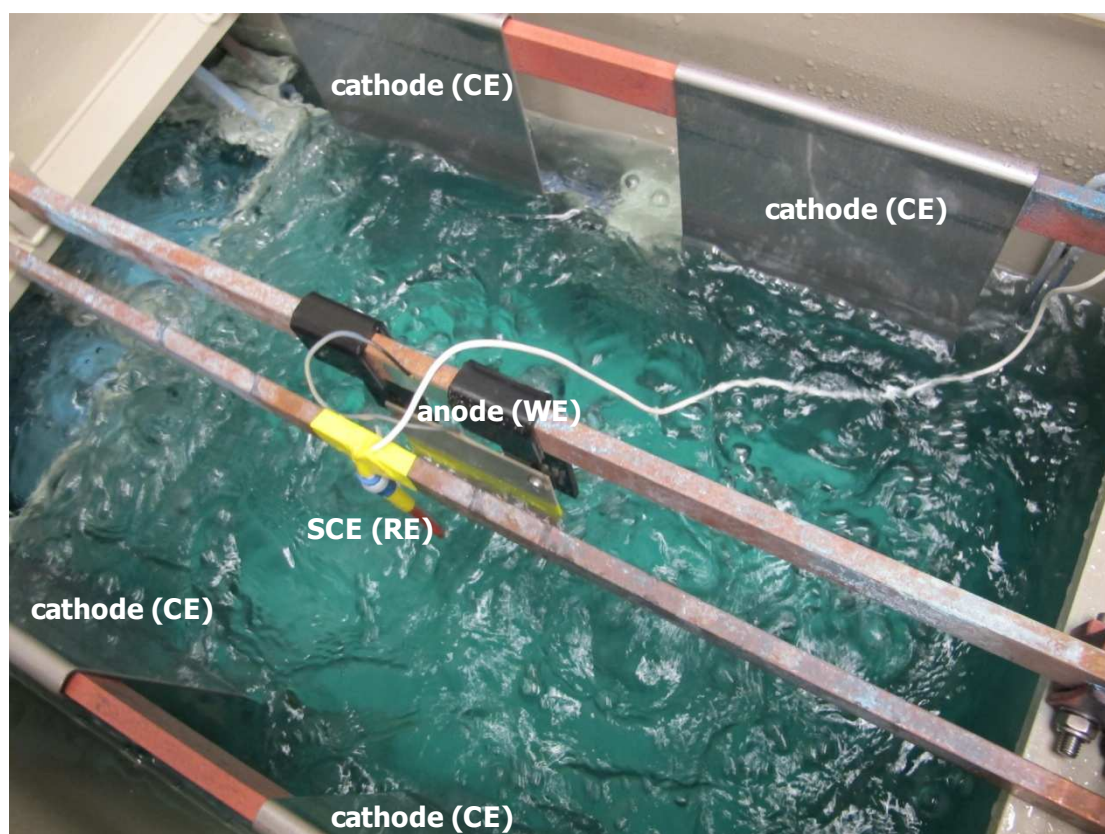
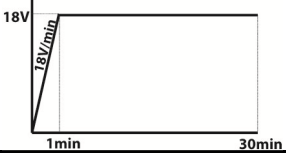
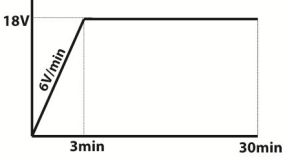
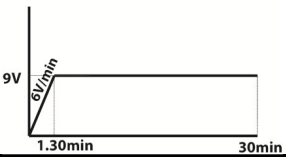
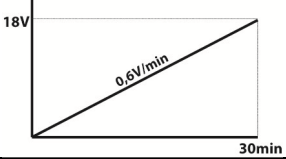
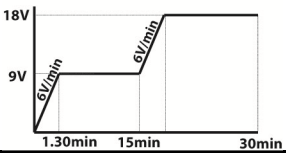
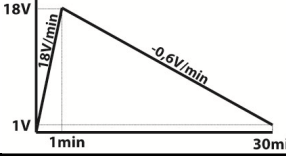
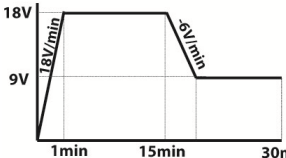


Figure 36. Experimental anodizing set-up: three-electrode cell with an AA1050 specimen as anode (working electrode), four stainless steel plates as cathodes (counter electrode) and an SCE electrode (reference electrode)

3.3.4 Drying

After anodizing and rinsing, the specimens were dried in an oven at 55°C. For AA1050 plates the drying time was 10min and for AA2024-T3 clad plates (in the titanium rack) 20 min.

Table 7. Anodizing test matrix

Voltage cycle	Al alloy	Electrolyte	Stop anodizing after ... min
Cycle 1 	AA1050	PSA	5
	AA1050		15
	AA1050		30
	AA1050	SAA	5
	AA1050		15
	AA1050		30
Cycle 2 	AA1050	PSA	5
	AA1050		15
	AA1050		30
	AA2024-T3 clad	PSA	30
	AA1050		5
	AA1050		15
Cycle 3 	AA1050	PSA	5
	AA1050		15
	AA1050		30
	AA1050	SAA	5
	AA1050		15
	AA1050		30
Cycle 4 	AA1050	PSA	30
	AA2024-T3 clad	PSA	30
	AA1050	SAA	30
Cycle 5 	AA1050	PSA	30
	AA2024-T3 clad	PSA	30
	AA1050	SAA	30
Cycle 6 	AA1050	PSA	30
	AA2024-T3 clad	PSA	30
	AA1050	SAA	30
Cycle 7 	AA1050	PSA	30
	AA2024-T3 clad	PSA	30
	AA1050	SAA	30

3.4 Surface Analysis

3.4.1 Coating weight measurements

The coating weight is given by the difference in specimen weight before and after chemically dissolving the oxide film. Coating weight measurements were performed on samples that were cut to a size of 75x75mm. The accuracy of the analytical balance used for weight measurements was 0,1mg. Stripping the oxide film was done by immersing the specimen in a gently boiling (approximately 100°C) phosphoric-chromic acid solution for 5 minutes. The solution consisted of $20 \pm 0,5$ g chromic acid and $35 \pm 0,5$ ml phosphoric acid (85%, density 1,69), dissolved in 1 liter distilled water.

3.4.2 Morphology surface anodic film

Images of the anodic film outer surface were collected with a Jeol 6500-F FE-SEM at Delft University of Technology. Image capturing occurred at an accelerating voltage of 5,0-6,0keV at a working distance of 4,0-9,4mm.

Since aluminum oxide is a non-conducting material, the samples were coated with a thin Pt layer of 2,0nm to prevent charging [64].

3.4.3 Morphology cross sections anodic film

Cross-sections of AA1050 anodic films were obtained by making a small cut in the specimen, cooling the specimen in liquid nitrogen and then breaking it in the direction shown in Figure 37. A Pt coating of 2nm was applied on the cross sectional surfaces immediately after breaking. Broken surfaces were stored at room temperature in a dry environment for a maximum period of one week before SEM analysis.

For analysis of AA1050 cross sections, the same SEM settings were used as described above in §3.4.2.

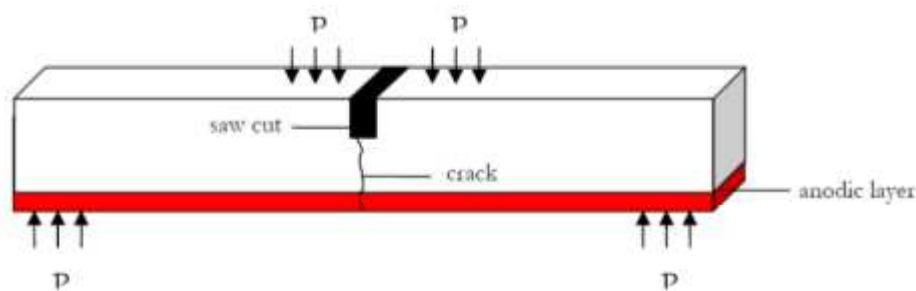


Figure 37. Breaking an anodized specimen to study film cross section [65]

Although broken surfaces can provide basic information on cross-section morphology, these surfaces cannot be used for accurate measurements of pore diameters and interpore distances. The reason for this is that the fracture mode of an unknown anodic film cannot be predicted at forehand. Several possible cleavage planes for anodic oxide films are shown in Figure 38. For anodizing in phosphoric acid cleavage along AA planes was found (Figure 38 (a)) [8], but for sulphuric acid anodizing cleavage rather occurred along cell walls (Figure 38 (b)) [66]. For PSA anodizing, it is thus hard to predict the cleavage plane which would be obtained upon fracturing a porous anodic film.

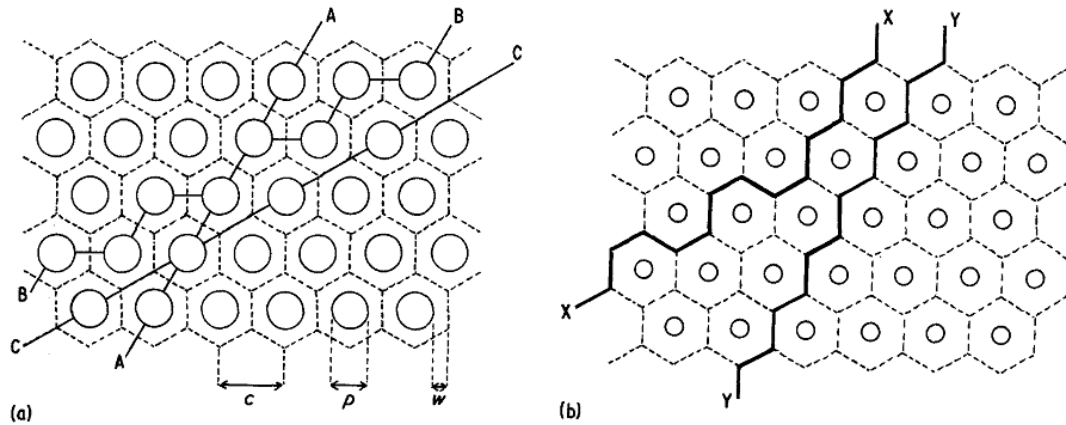


Figure 38. (a) Possible cleavage planes as suggested by Booker et al. [67] and (b) cleavage planes obtained by Arrowsmith, Clifford and Moth upon fracturing films formed in sulfuric acid [66]

Therefore, cross sections of the AA2024-T3 clad samples, which would be used to measure pore diameters, cell diameters and barrier layer thicknesses, were prepared by a Hitachi IM4000 ion milling system at the Energy Centre of the Netherlands (ECN). During this process, an argon ion beam gradually removes sample material, so that a mirror-surface quality cross sectional plane is formed (Figure 39). Preferential cleavage planes do not play a role during this process.

The morphology of ion milled cross sections was studied also at ECN with a Hitachi SEM SU-70, suitable for non-conducting samples. Image capturing occurred at an accelerating voltage of 2,0 keV at a working distance of 2,0-3,4mm. No Pt coating was applied.

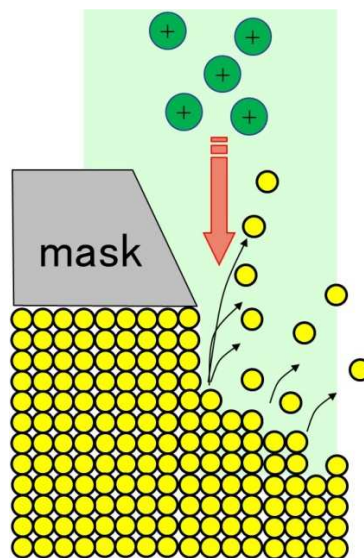


Figure 39. Schematic representation of cross section ion milling

4. Results

4.1 Limitations of semi-industrial scale system

To be able to interpret results from the anodizing experiments correctly, it is necessary to first discuss some limitations of working with semi-industrial scale equipment instead of a lab-scale set-up.

4.1.1 Temperature measurements and control

Only the temperature of the electrolyte bath could be measured and not the temperature of the actual aluminum specimen. Figure 40 gives a typical example of a temperature profile that was recorded during a typical anodizing run. Many fluctuations are seen in the profile, which indicates that the cooling/heating system did not always manage to keep the temperature exactly at 28°C. However, not all fluctuations are thought to reflect actual differences in temperature. Sudden peaks, like around $t = 6\text{min}$ and $t = 28\text{min}$ are attributed to malfunction of a coax cable in the system and not to actual differences in temperature.

From the measurement data, the average electrolyte temperature during each experiment was calculated. It turned out that the average temperature was never lower than 27,2°C and never higher than 29,1°C For a complete overview of temperature measurements, the reader is referred to Appendix 1.

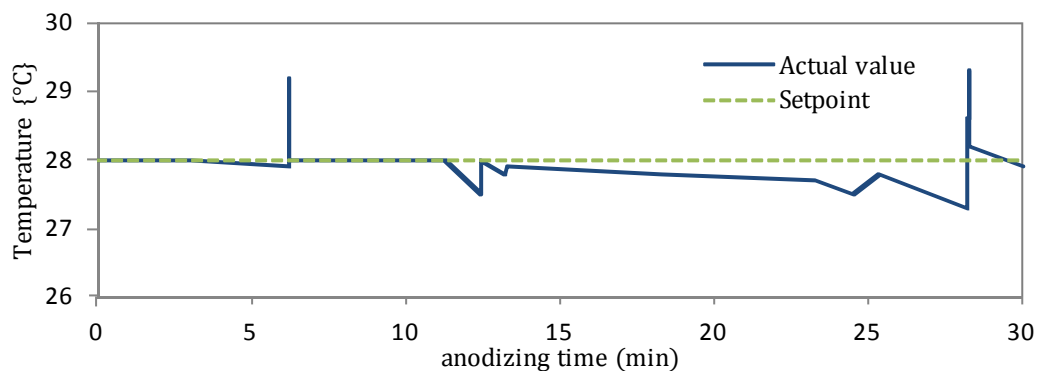


Figure 40. Temperature fluctuations during PSA anodizing of AA 1050, voltage cycle 2

4.1.2 Voltage programming and current density measurements

Figure 41 displays the V/t and i/t curves of AA1050 anodizing in PSA, voltage cycle 2.

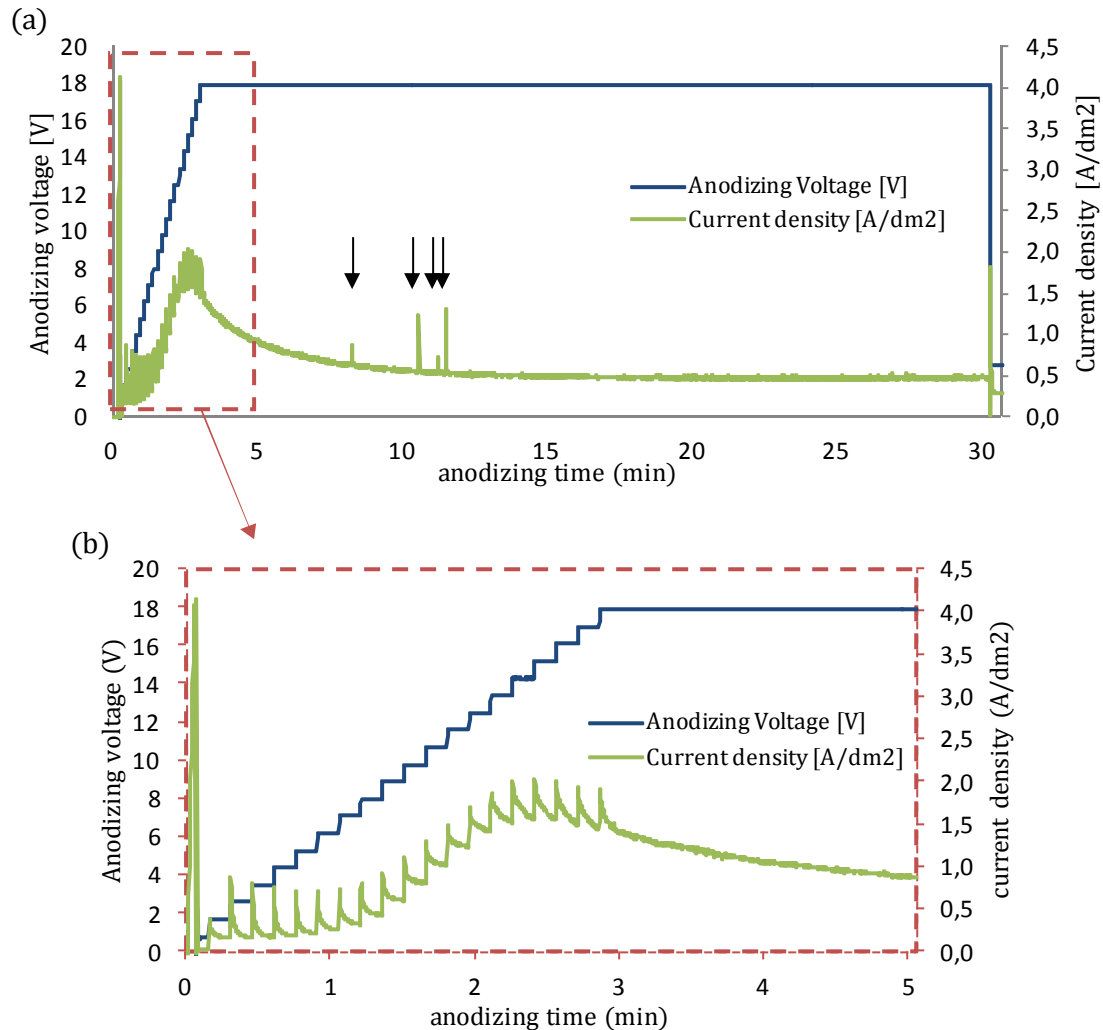


Figure 41. Current density and voltage recorded during PSA anodizing of AA1050, voltage cycle 2, for (a) 30min and (b) 5 min.

A first important observation is that when the system was programmed to *linearly* increase the voltage during the first minutes ($0 < t < 3\text{min}$), the voltage actually increased in *steps of $\pm 1\text{V}$* . Because of this step-wise voltage increase, the current density curve also showed a step-wise behavior during the sweep period. Immediately after each voltage step the current increases quickly, followed by an exponential decrease in current. This behavior is consistent with the theory found in literature, described in §1.5. As soon as the voltage is risen, the barrier layer is thinner than the equilibrium value. Therefore, the resistance against current flow is low which causes the current to rise quickly. The subsequent current decrease is caused by barrier layer thickening. The voltage steps are taken so quickly after each other that the system does not have enough time to reach its steady-state in-between two steps.

Secondly, at the beginning ($t = 0\text{min}$) and end ($t = 30\text{min}$) of each anodizing cycle a large current peak was recorded. These peaks are attributed to (1) the capacitive behavior of the electrical wiring system of the anodizing bath and (2) the charging characteristic between anode and cathode. The capacitive nature of the thin oxide film

on the aluminum anode is not expected to play a role, since the data recorder used in this study only had an acquisition rate of $\leq 5\text{Hz}$. The capacitive response of a porous oxide film is much faster [68], which makes it unlikely that charging/discharging of the oxide film is recorded.

A third observation is that even when the voltage is kept constant, some randomly occurring current peaks are recorded (e.g. around $t = 10\text{min}$ in Figure 41(a), indicated with arrows). These peaks are a result of penetration of the electrolyte under the polymer coating during the anodizing process.

The three effects described above (step-wise instead of linear increase in voltage, large current peak at beginning and end, current peaks due to penetration of electrolyte) are not expected to significantly influence the overall anodizing process. Therefore, from now on the beginning and end peak will be left out of the graphs and current peaks due to penetration will be neglected. The same goes for the steps in the voltage and current curves during voltage sweeps. An example of a 'simplified' curve is given in Figure 42.

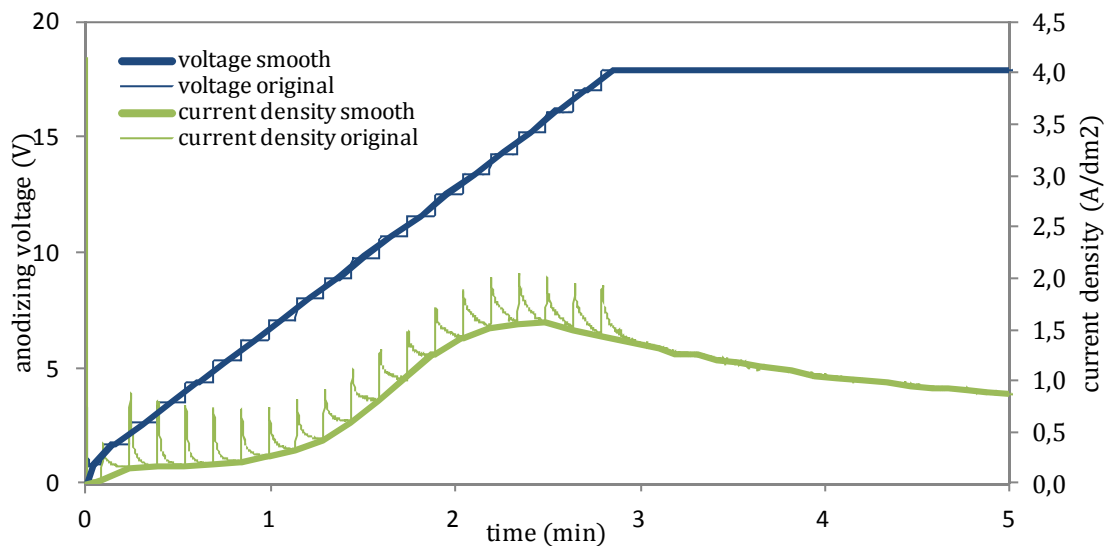


Figure 42. Smoothened voltage and current density curves for $0 < t < 5\text{ min}$ of PSA anodizing of AA1050, voltage cycle 2

4.2 Current density response

In this section, the effect of the anodizing voltage (steady or non-steady) on the anodizing current density is reported. It must be emphasized that the current densities recorded as a function of time must be regarded as average values of the complete anode surface area. As such, curves give no information about local morphological changes but a general representation of oxide film formation.

4.2.1 Steady state anodizing voltage

During voltage cycles 1, 2, 3, 5, and 7, the anodizing voltage was kept constant long enough for the system to reach its steady state (constant current density). Measured current densities at steady-state are reported in Table 8. Steady state current densities were $0,50 \pm 0,03\text{ A/dm}^2$ at 18V and $0,23 \pm 0,01\text{ A/dm}^2$ at 9V for all cycles. For SAA, the current density was $0,92 \pm 0,03\text{ A/dm}^2$ at 18V and $0,38\text{ A/dm}^2$ at 9V. So, steady state

current densities for PSA anodizing are lower than for SAA anodizing and current densities at 18V are more than twice as high as at 9V.

Voltage cycle	Steady-state voltage (V)	Steady state current density (A/dm ²)	
		PSA	SAA
1	18	0,52	0,93
2	18	0,48	0,90
3	9	0,24	0,38
5	9	not steady yet	0,38
	18	0,53	0,89
7	18	0,48	0,94
	9	0,22	0,38

Table 8. Steady-state current densities for PSA and SAA anodizing of AA1050 at 28°C

4.2.2 Initial voltage sweep rate

To study the effect of the initial sweep rate, voltage cycles 1, 2 and 4 are compared. During these cycles the voltage is risen to 18V at different sweep rates: 18V/min (cycle 1), 6V/min (cycle 2) and 0,6V/min (cycle 4). Figure 43 shows the recorded current densities for both PSA and SAA.

As shown in Figure 43(b), five different stages can be identified during the first minutes of cycles with fast sweep rates (18V/min and 6V/min):

- 6) Rise in current during the first seconds.
- 7) A 'current plateau' during which the current remains almost constant. The plateau is found at higher current densities for 18V/min than for 6V/min.
- 8) Rise in current up to a peak value. The peak is higher and reached earlier in time for 18V/min than for 6V/min.
- 9) Slowly decreasing current just before the final voltage has been reached
- 10) As soon as the voltage has reached 18V, the current decreases exponentially until it eventually becomes constant (steady-state current).

When the voltage is increased very slowly at 0,6V/min, no clearly defined stages are recognized in the current density curve. Instead, the quasi-steady-state current is reached very quickly, within 2 sec, after each voltage increase.

4.2.3 Half-way voltage step

Figure 44 displays the electrochemical response of the system when the anodizing voltage is (a) increased or (b) decreased half-way the process.

First, the current response of voltage cycle 5 will be discussed (Figure 44(a)), where the voltage is increased from 9V to 18V (rate 6V/min) after 15min of anodizing. For SAA, the voltage increase between $t=15\text{min}$ and $t=16.30\text{min}$ leads to a linear increase in current density. For the PSA process, the increase in current slows down towards to end of the sweep period. No current plateau, like identified during the initial voltage sweep (§4.2.2), is recorded during a voltage step.

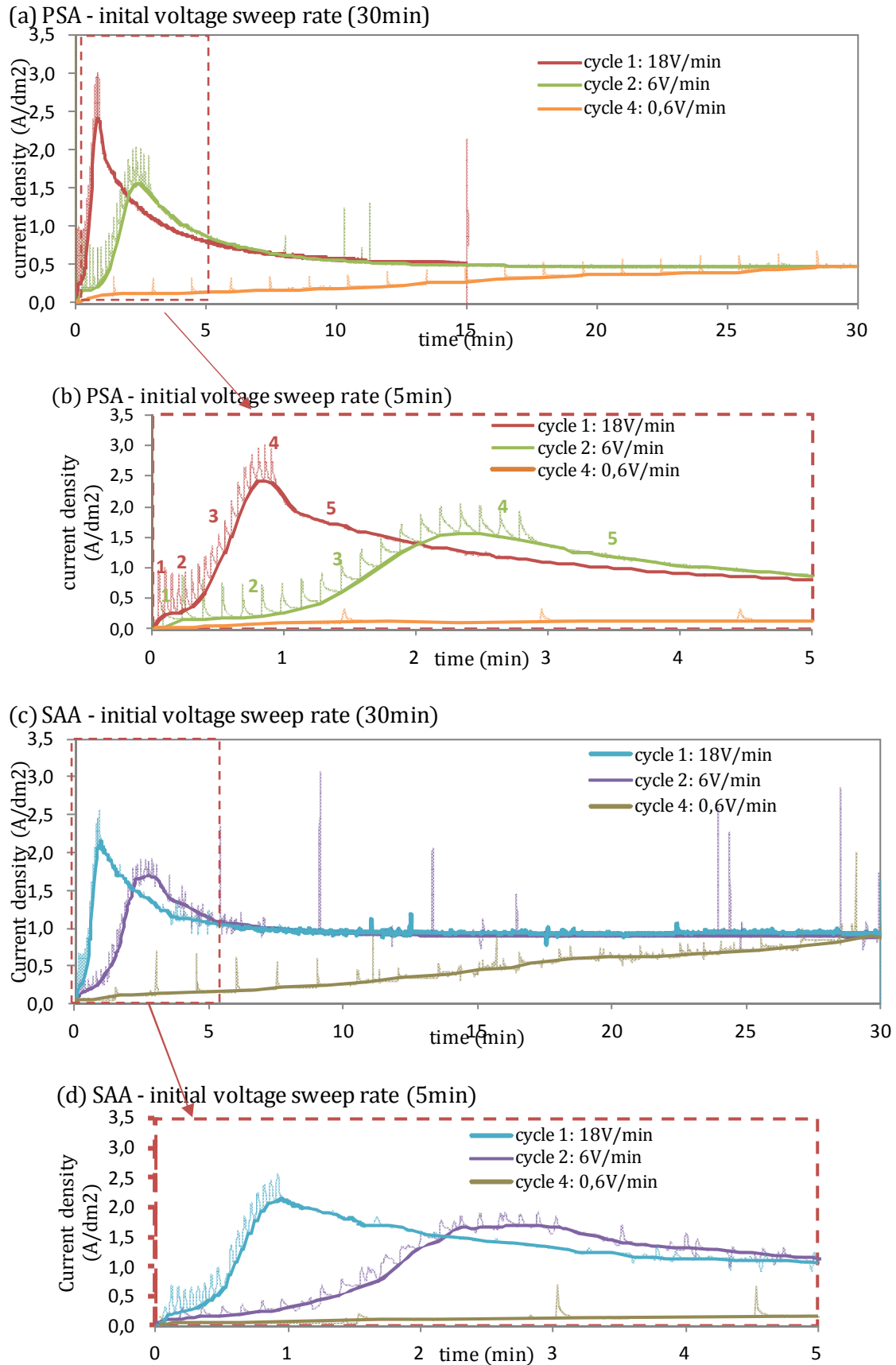
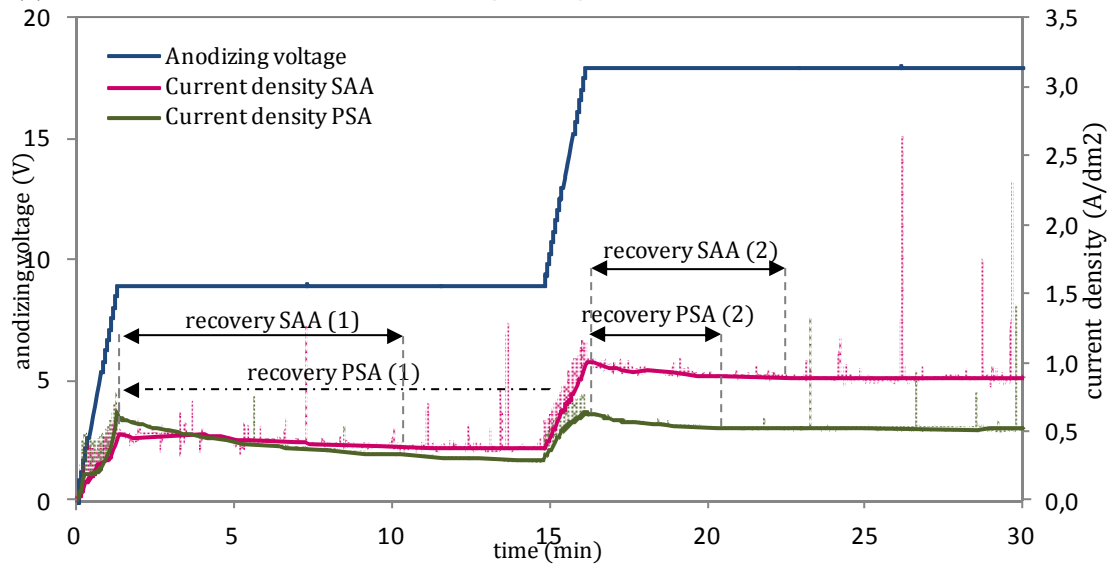


Figure 43. Current density recorded during potentiodynamic anodizing of AA1050 at 28°C. Applied voltage cycles were cycle 1 (sweep rate 18V/min up to 18V), cycle 2 (6V/min) and cycle 4 (18V/min) in PSA for 30min (a) and 5min (b) and in SAA for 30min (c) and 5min (d). Please note that the 18V/min curve for PSA is from the 15min cycle, because the one from the 30 min cycle was not recorded properly.

(a) SAA and PSA - increase in anodizing voltage



(b) SAA and PSA - decrease in anodizing voltage

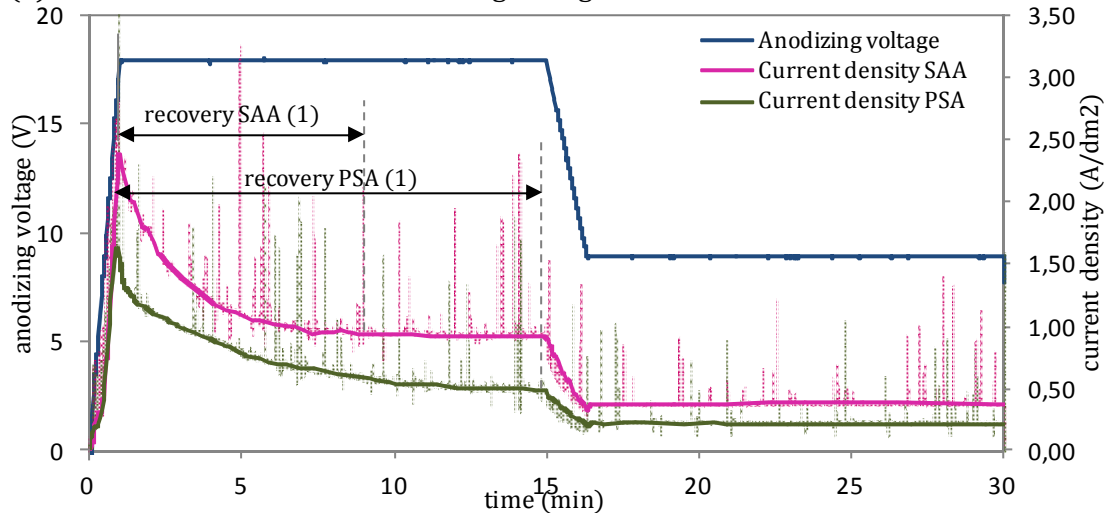


Figure 44. Potentiodynamic anodizing of AA1050 in PSA and SAA at 28°C with (a) increasing the voltage halfway the anodizing process and (b) decreasing the voltage halfway the process

After the voltage step, the recovery time (time until steady state is reached) is much shorter than after the initial voltage sweep. Interestingly, the recovery time was longer in PSA than in SAA after the initial voltage sweep, while it is the other way around after the voltage step.

The effect of a voltage *decrease* instead of increase was studied by applying voltage cycle 7, see Figure 44(b). After 15 min of anodizing, the voltage was decreased from 18 V to 9 V (at -6 V/min). This is accompanied by a fast, almost linear decrease in current density for both PSA as SAA. As soon as the voltage reaches 9 V, the current density increases again slightly towards the new steady state value. Recovery after the downwards voltage step is so fast for both PSA and SAA that it can hardly be recognized in the curve.

4.3 Morphology of anodic film

4.3.1 Cross section morphology

The morphology of anodic film cross sections was studied with the SEM. As described in §3.4.3, cross sections were obtained either by breaking the specimen (all specimens) or by ion milling (only AA2024-T3 clad specimens) An overview of the collected SEM images can be found Appendix 2.

Figure 45 shows FE-SEM images of three film cross sections (broken surfaces): (a) a PSA film on AA1050, (b) a PSA film on AA2024-T3 clad and (c) an SAA film on AA1050. All films were produced under the same conditions: $T=28^{\circ}\text{C}$, $t=30\text{min}$ and voltage cycle 2. Please note that the magnification of the PSA images (25 000x) differs from that of the SAA image (13 000x). The PSA films on AA1050 and AA2024-T3 clad are similar, except for the high roughness of the outer surface of the AA1050 film. Larger differences exist between the PSA and SAA films. First of all, the SAA film is more than twice as thick ($5,7\text{ }\mu\text{m}$) as the PSA films ($2,2$ to $2,5\text{ }\mu\text{m}$). Due to this thickness, the SAA film is heavily charged with electrons in the SEM and some areas are displayed completely white. Secondly, the SAA pores and cells are much smaller. Thirdly, the pore morphology of the SAA-film seems to be more constant throughout the film thickness. Though no exact pore diameters can be determined of these broken surface images (see §3.4.3), PSA pores seem to be larger in the top section than in the bottom section, while SAA pores are similar in both regions. A last observation is that the outer surface of the PSA film on AA1050 is very rough, while that of the SAA film on AA1050 is quite smooth.

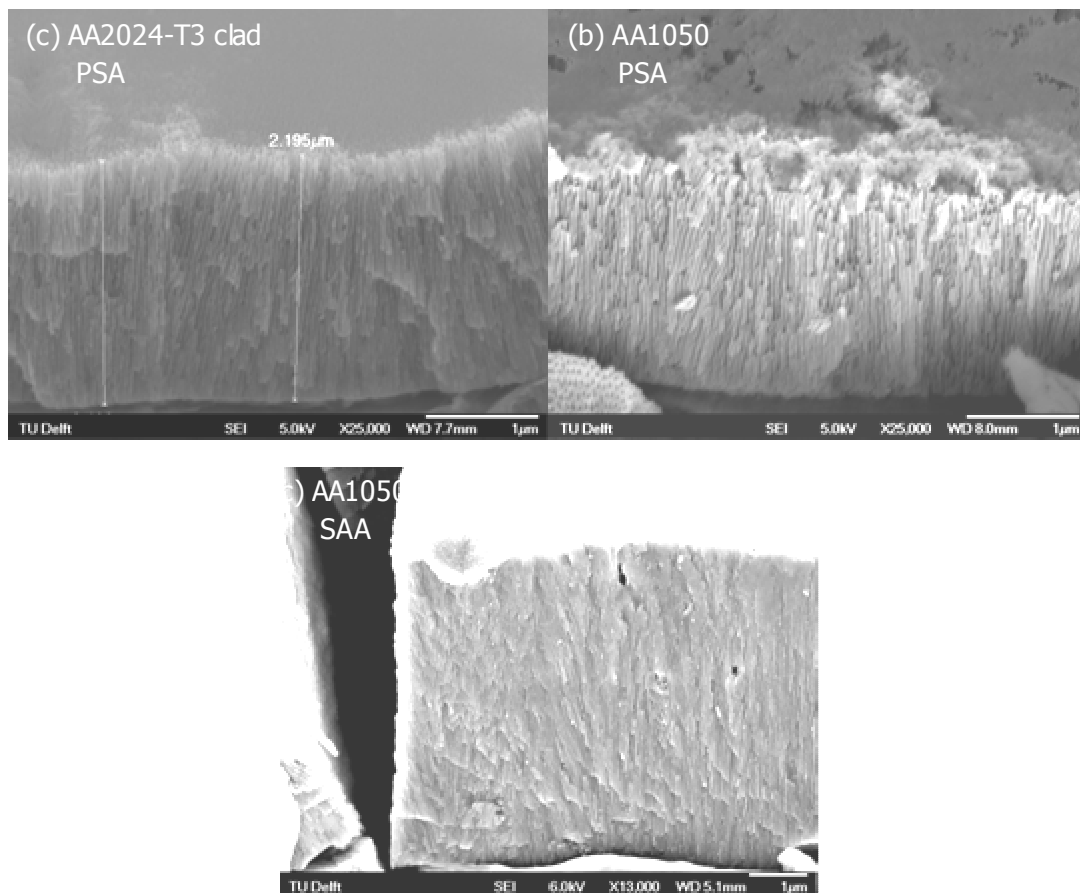


Figure 45. FE-SEM images of oxide films (cross-section) formed by anodizing for 30min at $T=28^{\circ}\text{C}$, using voltage cycle 2 (a) AA1050 in PSA, (b) AA2024-T3 clad in PSA and (c) AA1050 in SAA.

Another interesting comparison is that of film morphologies formed by voltage cycle 7 (*decreasing* the voltage half-way the process) with cycle 5 (*increasing* the voltage half-way the process), see Figure 46.

When voltage cycle 7 (*decrease* in voltage) is applied, the resultant oxide film shows to exist of two distinct regions: a layer with coarse pores on top of a layer with much finer pores (Figure 46(a&b)). The layer with coarse pores is thicker than the layer with fine pores. This result is found both for PSA and SAA films, on both AA1050 and AA2024-T3 clad alloys.

When the voltage is suddenly *increased* during the process (cycle 5), it would be logical to find a morphology opposite to that of a decreasing voltage (cycle 7). For SAA, indeed it seems like a thin, fine-featured layer indeed exists on top of a thicker layer with a coarse morphology. However, no distinct border is seen between the fine-featured and the coarse film region. For the PSA film, no different regions are observed at all.

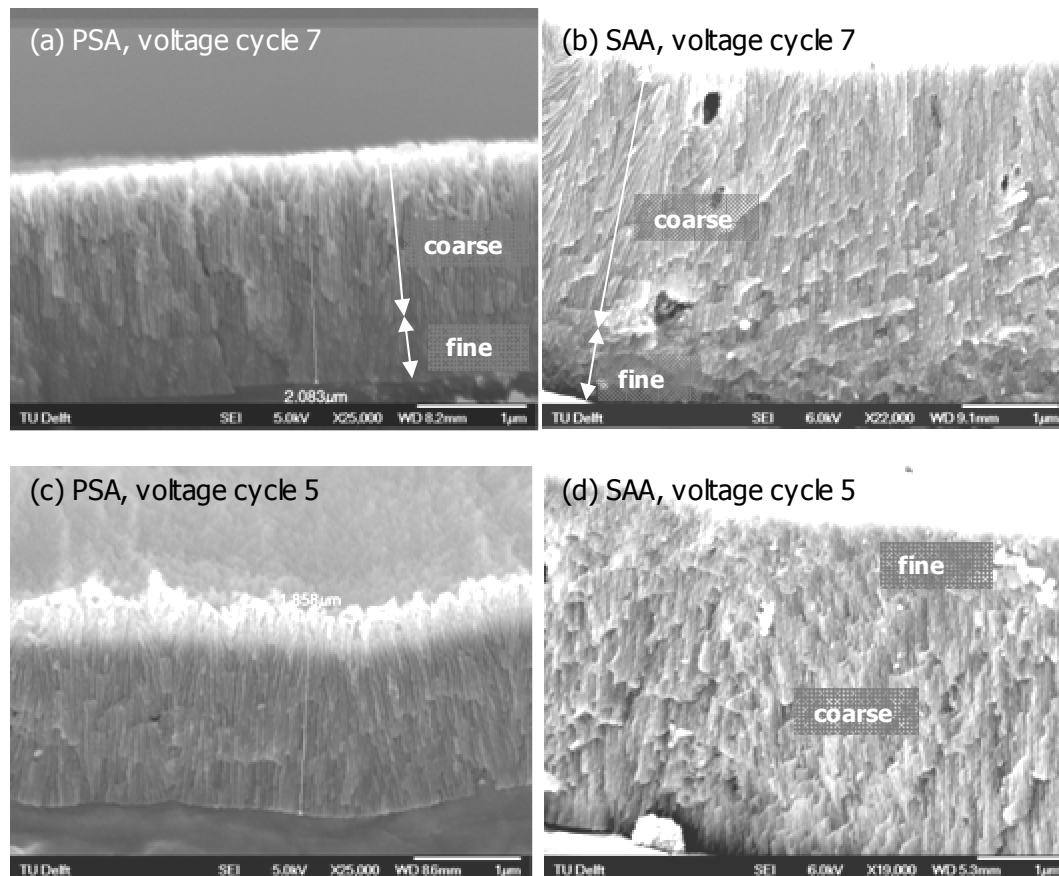


Figure 46. FE-SEM images of oxide films (cross-section) formed on AA1050 by anodizing for 30min in (a) PSA, voltage cycle 7, (b) SAA, voltage cycle 7, (c) PSA, voltage cycle 5 and (d) SAA, voltage cycle 5.

Ion milled cross section of five AA2024-T3 specimens (voltage cycle 2, 4, 5, 6 and 7) were studied at ECN with an advanced type of SEM which decelerates the electrons before they hit the specimen surface. This technique reduces charging of non-conducting samples and as such the ion milled cross sections did not have to be coated, which minimizes the effect of the coating on the morphology. Figure 47(a) displays the ion milled cross section of an AA2024-T3 clad specimen which was anodized for 30min in PSA using voltage cycle 2. While the voltage remained constant at 18V during almost the

whole anodizing cycle (except for a voltage sweep during the first 3 min), the pore morphology changes a lot across the film thickness. Close to the barrier layer, small pores are found, while pores get larger as we move towards the surface of the anodic film. The image software system *AnalySIS* was used to measure pore and interpore distances (equal to cell diameters) close to the outer surface and close to the barrier layer, as shown in Figure 47(b&c).

For the cycle 2-film shown in Figure 47, the average pore diameter in the top region of the film was two times as large as in the bottom section (33nm vs 15nm). The difference between the average cell diameter in the top (53nm) and bottom (44nm) is smaller. The barrier layer was found to have an average thickness of 16nm.

Pore diameters, cell diameters and barrier layer thicknesses measured from other ion milled cross sections are given in Table 9. For all PSA samples, pores close to the surface are larger than those in the bottom section. For cell diameters, this is not the case.

However, it must be emphasized that during ion milling, pores are probably not cut exactly through the middle. This means that actual diameters might be somewhat larger than the measured diameters. To minimize this effect, only large pores were used for determination of the pore diameter since those are more likely to be representative of the real pore diameter. Also, it is expected that the measurement error due to this problem is roughly the same for all specimens, so comparing the data of different specimens is still valid.

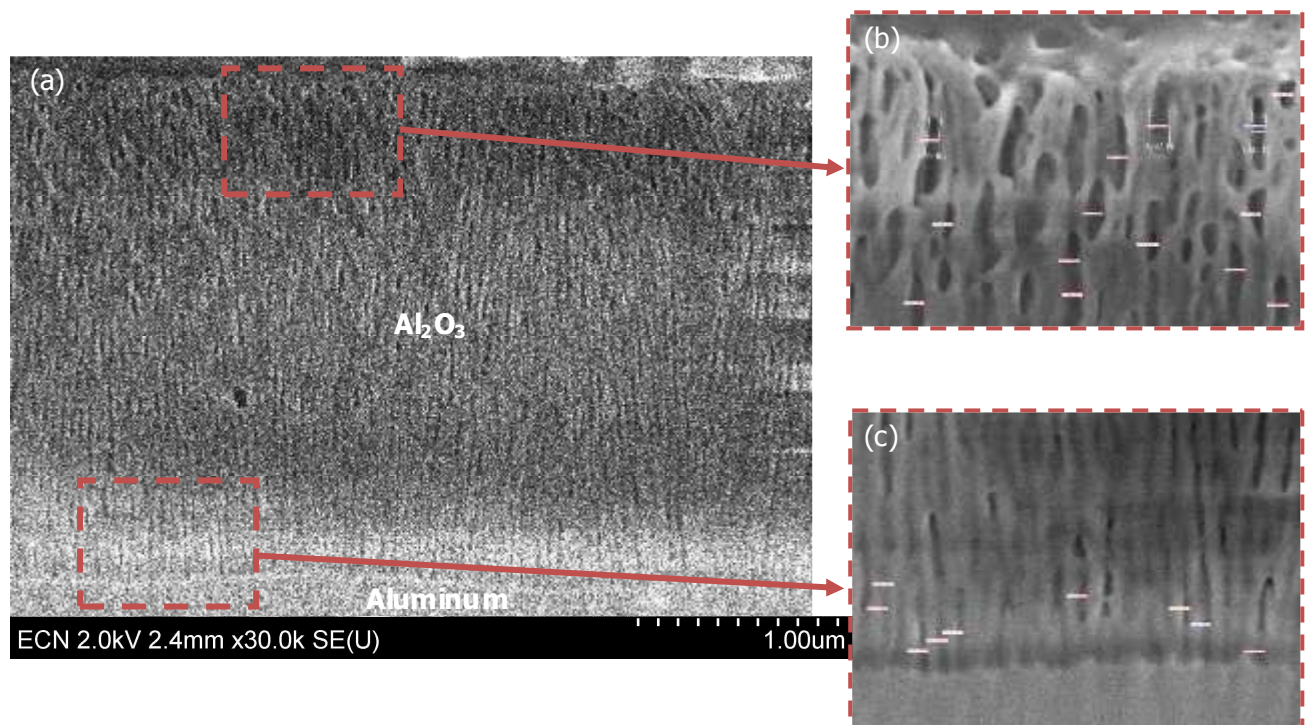


Figure 47. Ion milled cross section of AA2024-T3 clad samples anodized in PSA for 30min voltage cycle 2 (a) whole layer, (b) top part and (c) bottom part of the film.

Anodizing voltage				Electro-lyte	Material	Barrier layer thickness (nm)		Pore diameter top (nm)		Pore diameter bottom (nm)		Cell diameter top (nm)		Cell diameter bottom (nm)	
Cycle nr.	Initial sweep rate (V/min)	Average voltage (V)	Voltage at t=30min (V)			mean	σ	mean	σ	mean	σ	mean	σ	mean	σ
2	6	17,1	18	PSA	AA2024-T3 clad	16	1	33	6	15	3	53	15	44	5
4	0,6	9,0	18	PSA	AA2024-T3 clad	20	1	24	3	20	3	41	8	52	9
5	6	13,1	18	PSA	AA2024-T3 clad	20	2	24	4	17	3	51	8	52	6
6	18	9,5	1	PSA	AA2024-T3 clad	6	1	29	6	12	4	42	6	28	5
7	18	13,4	9	PSA	AA2024-T3 clad	16	3	30	4	11	2	47	7	25	4

Table 9. Morphological features measured from film cross sections after 30min of anodizing at T=28°C

Anodizing voltage				Electro-lyte	Material	Pore diameter outer surface $d_{surf}(\text{nm})$						Cell diameter outer surface $c_{surf}(\text{nm})$					
Cycle nr.	Initial sweep rate (V/min)	Average voltage (30min) (V)	Voltage at t=30min (V)			After 5min anodizing		After 15min anodizing		After 30min anodizing		After 5min anodizing		After 15min anodizing		After 30min anodizing	
						mean	σ	mean	σ	mean	σ	mean	σ	mean	σ	mean	σ
1	18	17,7	18	PSA	AA1050	14	2	23	4	29	4	27	4	35	5	58	8
1	18	17,7	18	SAA	AA1050	13	2	14	3	10	1	25	7	20	4	17	3
2	6	17,1	18	PSA	AA1050	13	4	19	3	28	5	23	4	30	5	49	8
2	6	17,1	18	PSA	AA2024-T3 clad	-	-	-	-	32	4	-	-	-	-	45	5
2	6	17,1	18	SAA	AA1050	11	2	10	1	12	2	18	2	17	3	19	3
3	6	8,8	9	PSA	AA1050	15	3	18	4	18	3	25	4	29	4	33	4
3	6	8,8	9	SAA	AA1050	13	3	14	3	13	2	21	3	24	3	24	5
4	0,6	9,0	18	PSA	AA1050	-	-	-	-	19	4	-	-	-	-	32	6
4	0,6	9,0	18	PSA	AA2024-T3 clad	-	-	-	-	17	3	-	-	-	-	30	6
4	0,6	9,0	18	SAA	AA1050	-	-	-	-	15	3	-	-	-	-	22	5
5	6	13,1	18	PSA	AA1050	-	-	-	-	21	3	-	-	-	-	40	10
5	6	13,1	18	PSA	AA2024-T3 clad	-	-	-	-	17	3	-	-	-	-	35	7
5	6	13,1	18	SAA	AA1050	-	-	-	-	19	3	-	-	-	-	29	7
6	18	9,5	1	PSA	AA1050	-	-	-	-	27	4	-	-	-	-	44	6
6	18	9,5	1	PSA	AA2024-T3 clad	-	-	-	-	34	4	-	-	-	-	47	6
6	18	9,5	1	SAA	AA1050	-	-	-	-	12	2	-	-	-	-	19	4
7	18	13,4	9	PSA	AA1050	-	-	-	-	28	6	-	-	-	-	49	10
7	18	13,4	9	PSA	AA2024-T3 clad	-	-	-	-	33	5	-	-	-	-	46	9
7	18	13,4	9	SAA	AA1050	-	-	-	-	14	3	-	-	-	-	22	5

Table 10. Morphological features measured from outer film surfaces

Anodizing voltage				Electro-lyte	Material	Coating weight m_{ox} (mg/dm ²)	Charge passed Q (C/dm ²)	Anodic oxide formation efficiency η_{ox} (%)
Cycle nr.	Initial sweep rate (V/min)	Average voltage (V)	Voltage at t=30min (V)					
2	6	17,1	18	PSA	AA2024-T3 clad& AA1050 ⁵	46,2	1092	24
2	6	17,1	18	SAA	AA1050	98,0	1719	59
4	0,6	9,0	18	PSA	AA2024-T3 clad& AA1050 ⁵	21,4	537	23
4	0,6	9,0	18	SAA	AA1050	40,3	819	51
5	6	13,1	18	PSA	AA2024-T3 clad& AA1050 ⁵	31,8	864	21
5	6	13,1	18	SAA	AA1050	65,5	1195	57
6	18	9,5	1	PSA	AA2024-T3 clad& AA1050 ⁵	8,0	841	5
6	18	9,5	1	SAA	AA1050	31,8	870	38
7	18	13,4	9	PSA	AA2024-T3 clad& AA1050 ⁵	22,6	866	15
7	18	13,4	9	SAA	AA1050	64,8	1383	49

Table 11. Anodic oxide formation efficiencies

⁵ For calculation of the theoretical mass the charge passed Q during an AA1050-run was used, while the actual coating weight was measured on AA1230.

4.3.2 Outer surface morphology

Besides the cross section morphology, the surface morphology (top view) of all specimens was studied with FE-SEM. Due to the small size of the pores in the anodic films, magnifications of up to 300 000x had to be used to clearly display all surface features. However, it proved difficult to collect sharp images at large magnifications with a FE-SEM due to the high roughness of the surface and charging of the non-conducting oxide films. As shown in Figure 48, the quality of the surface images went down when studying thicker oxide layers. A more advanced type of SEM, or a Transmission Electron Microscope (TEM) would have been more appropriate to retrieve high magnification images of thick oxide films, but this type of equipment was not available for this study.

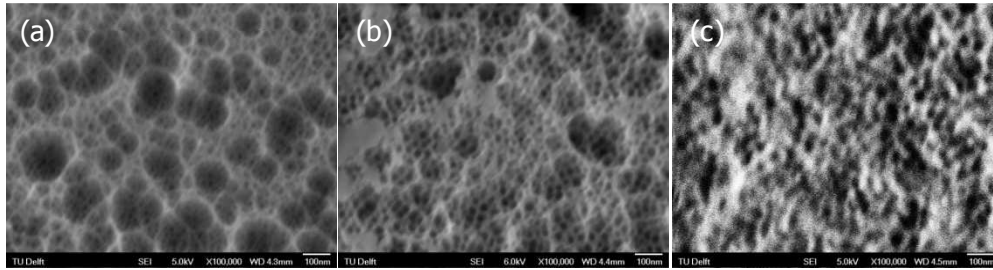


Figure 48. FE-SEM surface images (100 000x) of AA1050, PSA anodized at 28°C, voltage cycle 2 (a) after 5min anodizing, thickness=0.2μm, (b) after 15min anodizing, thickness=1.5μm, and (c) after 30min anodizing, thickness=2.5μm

An overview of all SEM surface images can be found in Appendix 3. Despite the fact that the images are not all perfectly sharp, they could be used for measurements of pore and cell diameters. The measurement error is expected to be larger for SAA than for PSA specimens, since SAA pores were much smaller and therefore even harder to display than PSA pores. Figure 49 shows how the image software system *AnalySIS* was used to measure the area of pores and interpore distances. At least ten pore areas and interpore distances were measured on each specimen. The interpore distance is equal to the cell diameter c . From the pore surface area A , the pore diameter d could be calculated:

$$d = 2 \cdot \sqrt{\frac{A}{\pi}} \quad (17)$$

An overview of the average pore and cell diameters of each specimen is given in Table 10 on page 54.

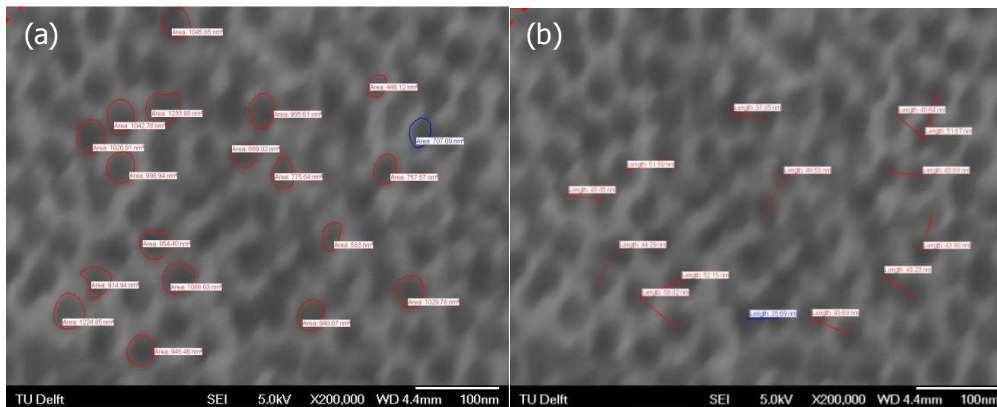


Figure 49. Measurements of outer surface (a) pore diameters and (b) cell diameters (equal to interpore distance) with AnalySIS software.

A first conclusion that can be drawn from the values shown in Table 10 is that PSA pore and cell diameters measured on AA1050 are roughly equal to those measured on AA2024-T3 clad.

Secondly, pore and cell diameters are larger for PSA than for SAA, especially when the anodizing time is longer. Figure 50 displays the pore and cell diameters (PSA and SAA) versus anodizing time for voltage cycle 1, 2 and 3. After 5 minutes of anodizing, the dimensions measured for PSA and SAA within the same order of magnitude (pore diameter 10-15nm, cell diameter 17-27nm), but for prolonged anodizing PSA pores and cells become much larger. For instance, after 30 min of anodizing (voltage cycle 1) the average pore diameter was 29nm for PSA, compared to only 10nm for SAA (Figure 50(a)). This 'pore widening effect' is more pronounced for voltage cycles 1 and 2 (final voltage 18V) compared to voltage cycle 3 (final voltage 9V).

(a) pore diameter outer surface vs anodizing time

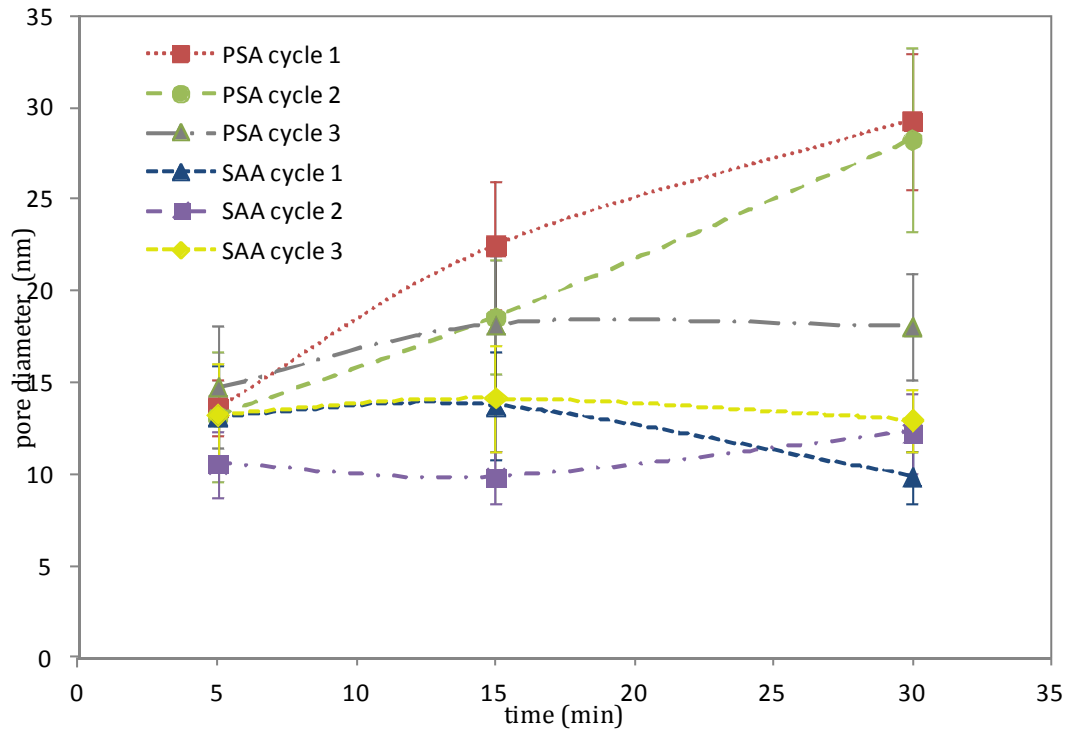


Figure 50(a) Pore diameter at outer surface of AA1050 vs anodizing time for both PSA and SAA, voltage cycles 1, 2 and 3

(b) cell diameter outer surface vs anodizing time

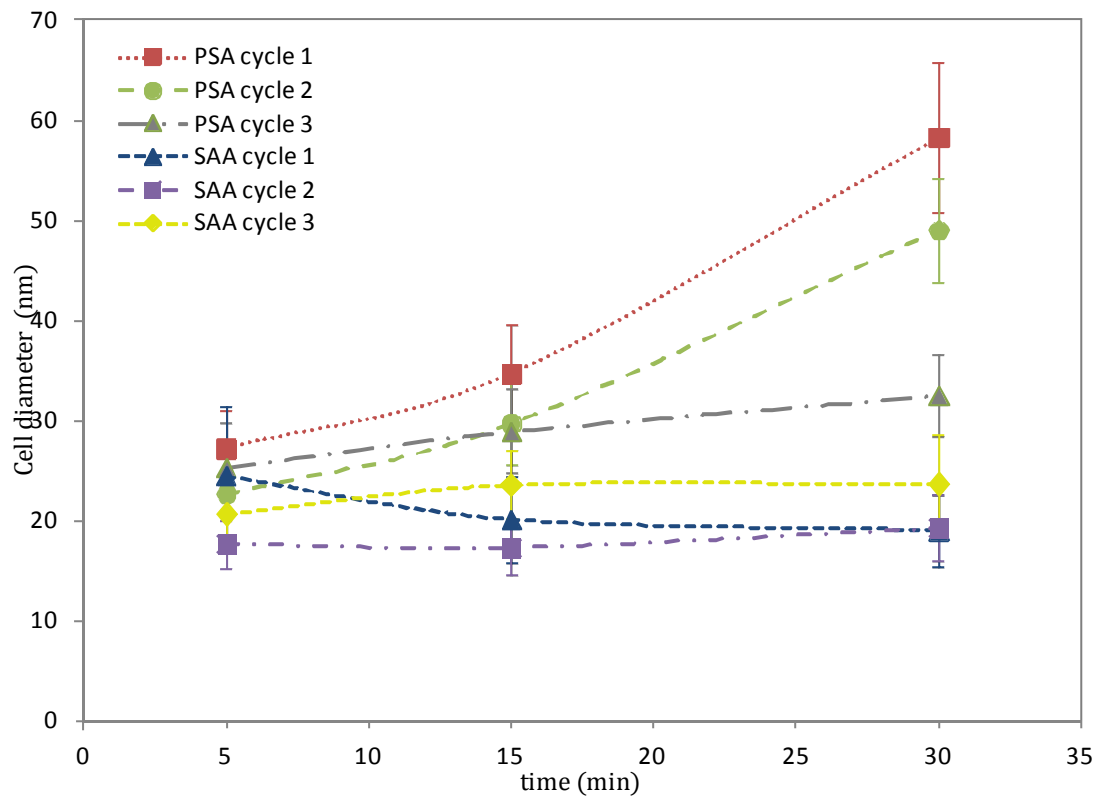
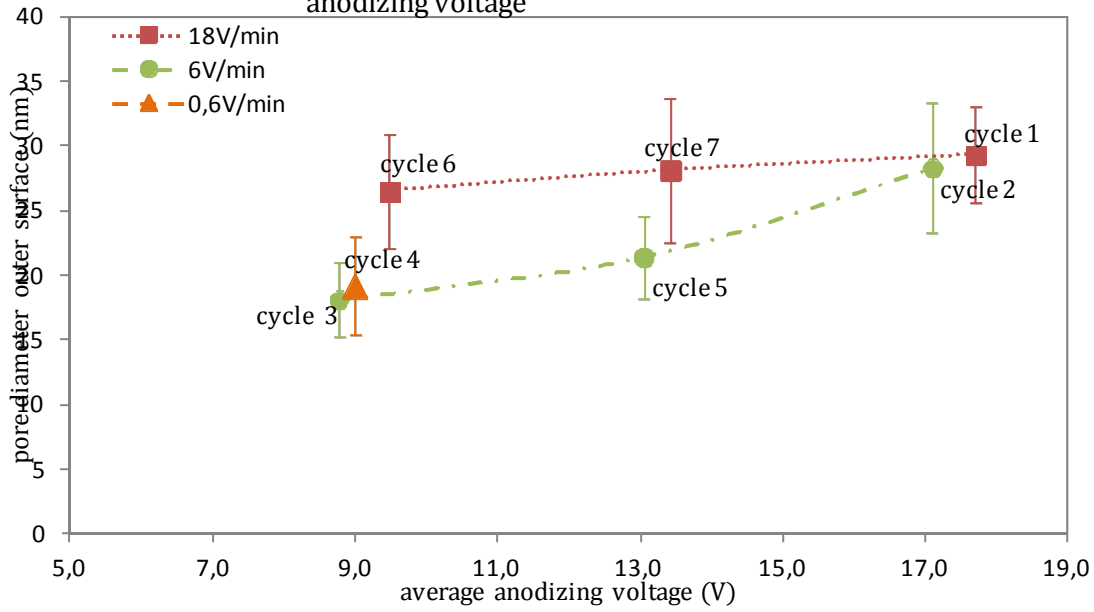


Figure 50(b) Cell distance at outer surface of AA1050 vs anodizing time for both PSA and SAA, voltage cycles 1, 2 and 3

Let's take a further look at the relation between anodizing voltage and surface morphology. In Figure 51, PSA pore and cell diameters after 30 min of anodizing are plotted against the average anodizing voltage during a cycle. The initially applied sweep rate of a cycle (18V/min, 6V/min or 0,6V/min) is also indicated. Like observed before in Figure 50, outer surface pores and cells are larger when the average voltage during a run is higher. However, the initial voltage sweep seems to play even a bigger role. All specimens that were anodized with an initial voltage sweep of 18V/min have larger surfaces pores and cells than the other specimens (6V/min and 0,6V/min initial sweep rates).

For SAA, the relation between surface morphology and anodizing voltage is not displayed. Pore and cell diameters were equal for almost all anodizing cycles. So even if there were small differences, it could not be identified whether those were due to measurement errors or due to changing process parameters.

(a) pore diameter outer surface after 30min anodizing vs average anodizing voltage



(b) cell diameter outer surface after 30min anodizing vs average anodizing voltage

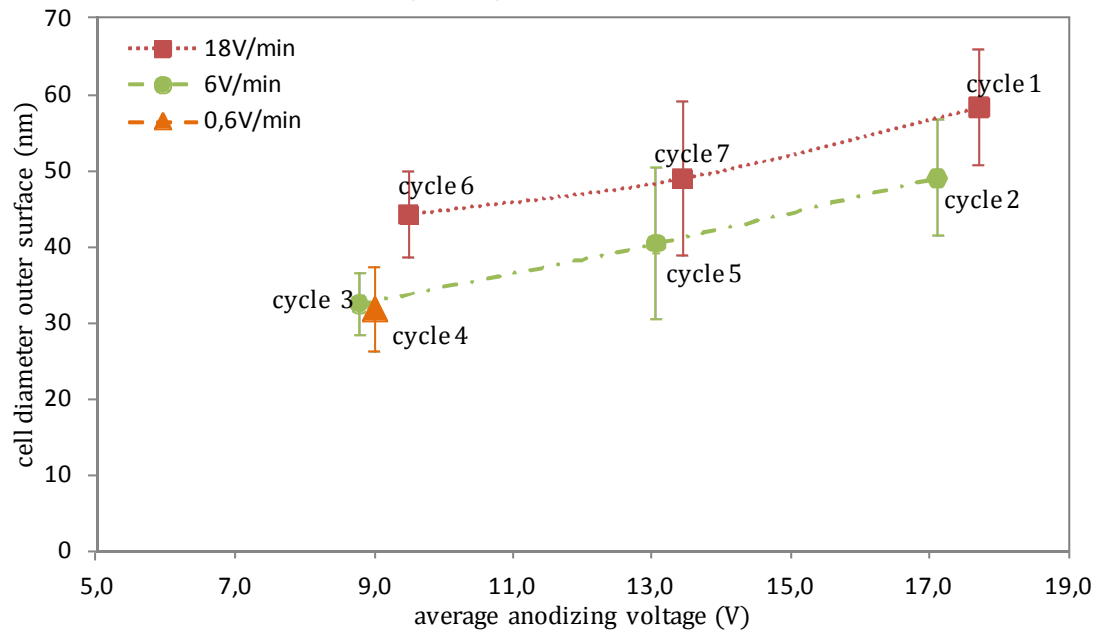


Figure 51. (a) pore diameter and (b) cell diameter after 30 min PSA anodizing of AA1050, vs the average voltage during a voltage cycle

4.4 Anodic oxide formation efficiency

The anodic oxide formation efficiency η_{ox} is the ratio of the measured film mass to the theoretical mass calculated from the charge passed, taking into account the charge efficiency. For porous anodic layers $\eta_{ox} < 1,0$ since a part of alumina that forms dissolves again in the electrolyte. The exact value of η_{ox} can be calculated according to:

$$\eta_{ox} = \frac{m_2 - m_3}{\eta_{charge} \cdot \frac{M_{ox} \cdot Q(t)}{n_{ox} \cdot F}} \quad (18)$$

where m_2 and m_3 are the weights of the specimen after anodizing (g dm^{-2}) and after oxide removal (g dm^{-2}), respectively, η_{charge} the charge efficiency, M_{ox} the molar mass of Al_2O_3 (102 g mol^{-1}), $Q(t)$ the cumulative charge transferred per dm^2 , n_{ox} is the number of electrons associated with oxide formation (6) and F is the Faraday's constant ($96\,500 \text{ C mol}^{-1}$).

The cumulative charge density $Q(t)$ is determined by integrating the current density over the anodizing time:

$$Q(t) = \int_0^t i(t) dt. \quad (19)$$

The charge efficiency η_{charge} is defined as the ratio of the amount of aluminum ions generated to the amount calculated from the charge passed [69]. It may be determined from the expression

$$\eta_{charge} = \frac{m_1 - m_3}{M_{Al} \cdot Q(t) / n_{Al} \cdot F}, \quad (20)$$

where m_1 and m_3 are the weights of the specimen before anodizing (g dm^{-2}) and after oxide removal (g dm^{-2}), respectively, M_{Al} the molar mass of aluminum (27 g mol^{-1}) and n_{Al} the number of electrons associated with Al^{3+} formation (3). Specimens could not be weighed before anodizing, so it was impossible to calculate η_{charge} . Since for small anodizing systems the charge efficiency η_{charge} is usually close to 1,0, this value will be used for further calculations.

Calculated anodic oxide formation efficiencies of 10 selected specimens are given in Table 11 on page 55. Please note that for calculation of PSA efficiencies, the charge passed Q during an AA1050-run was used while the coating weight was measured on an AA1230 specimen. This is not ideal, but since anodic films on both alloys have shown to be almost identical, this procedure will give a very good indication of the 'real' efficiencies. For calculation of SAA efficiencies, both the charge and coating weight were determined from AA1050 specimens.

The anodizing efficiency of SAA-anodizing turns out to be much higher than that of PSA-anodizing, for all voltage cycles. Voltage cycle 2 has the highest efficiency for both SAA and PSA. Since this is the voltage cycle with the highest average anodizing voltage, there might be a relation between average voltage and anodizing efficiency. Roughly, such a relation is indeed found when the efficiency is plotted against the average anodizing voltage (Figure 52). However, when the voltage is decreased during anodizing, the efficiency is always lower than when the voltage is increased, even though the average voltages are equal. This is clearly seen when cycle 4 is compared to cycle 6, and cycle 5 to cycle 7.

(a) Efficiency vs average anodizing voltage

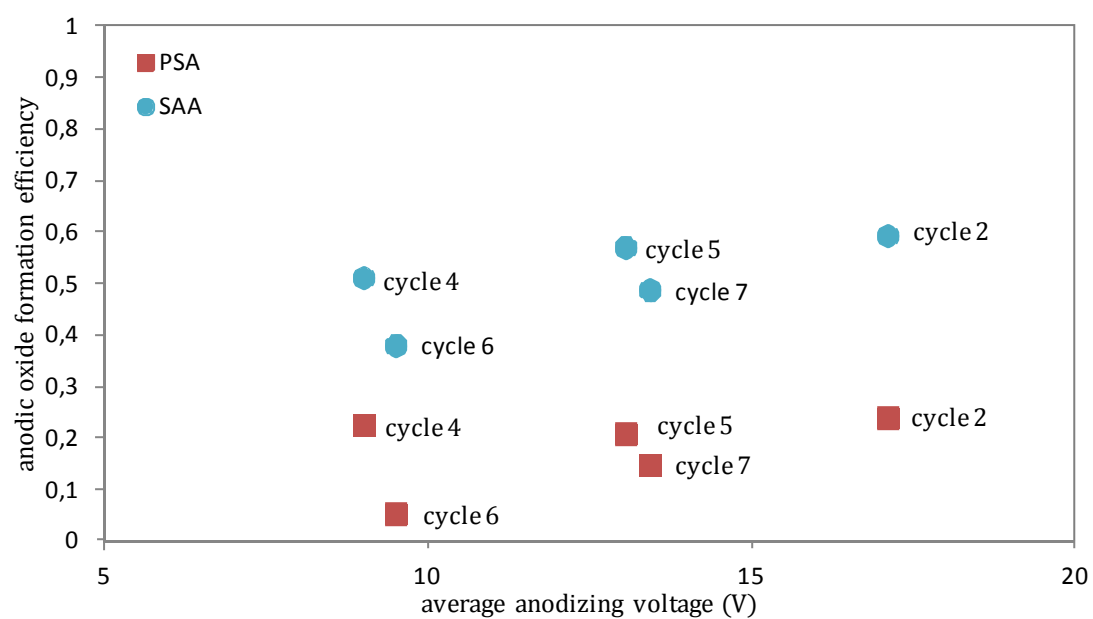


Figure 52. Anodic oxide formation efficiencies versus the average anodizing voltage.

5. Discussion

5.1 Expected versus measured morphologies

In this section it is discussed to what extent the experimental results (Chapter 4) match with previously formulated hypotheses (Chapter 2), and what could be the reasons for the observed differences.

On the next page, Figure 53 shows experimentally determined morphologies next to expected anodic film morphologies (schematic representations of cross sections). For SAA anodizing, the resemblance between expected and measured film morphologies is obvious. For PSA films, however, less resemblance is observed. Only the bottom film sections - close to the barrier layer – are in most cases consistent with the predictions. The upper film sections, on the other hand, show hardly any resemblance with expected morphologies. All experimental PSA films have large pores in the upper film section, while the expected films clearly exhibit a layer of small pores at the top. Another interesting finding is that for both PSA and SAA, the morphologies correspond better to the predictions for cycle 5 (increase in voltage half-way the process) than for voltage cycle 7 (decrease in voltage half-way the process).

As for the outer surface morphology (not shown in Figure 53) it was expected that pore diameters increase linearly with anodizing time. This showed to be the case for PSA, but not for SAA. Additionally, it was found for PSA that cell diameters increase with time as well, which was not previously reported in literature for any anodizing process.

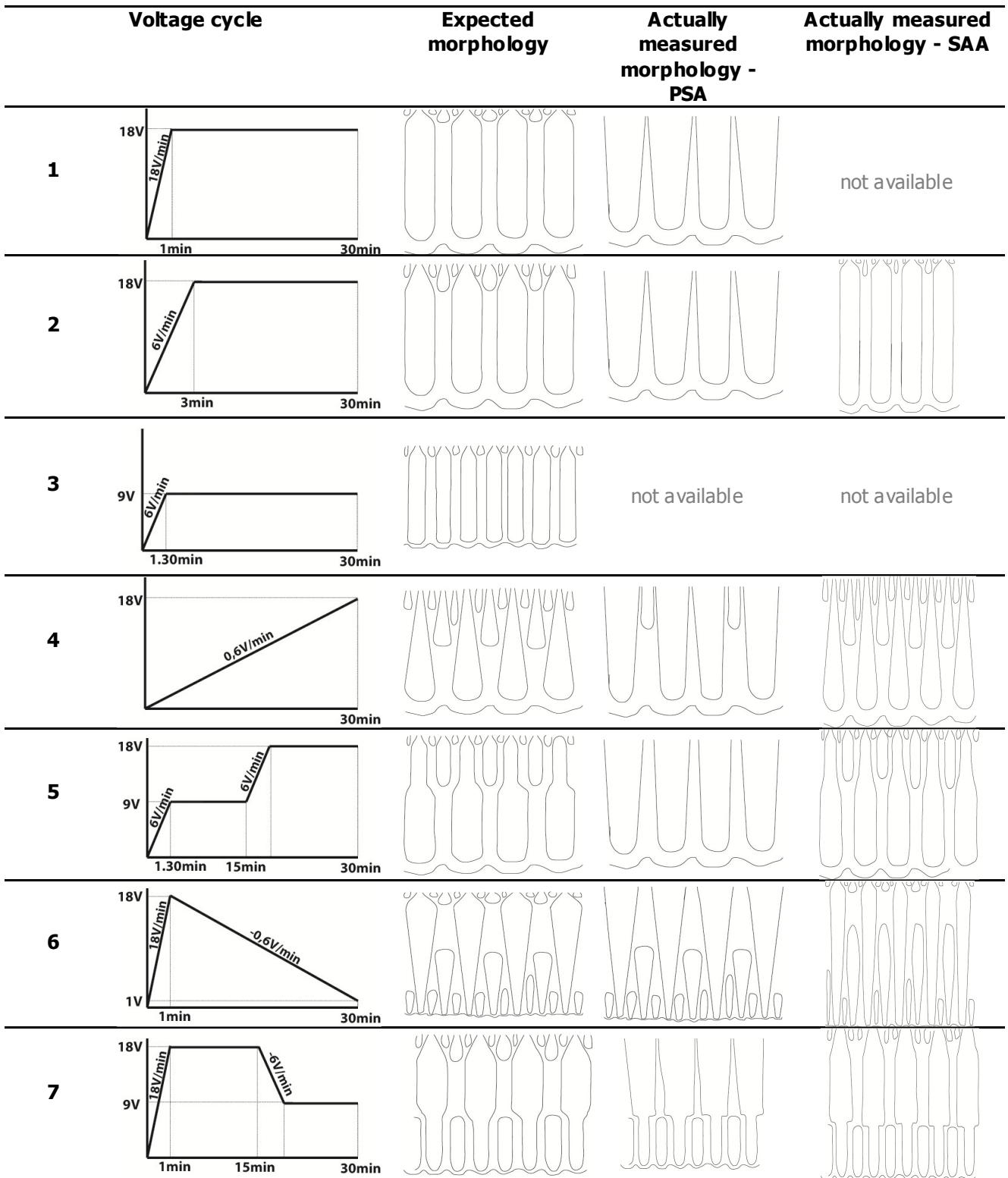


Figure 53. Expected vs measured anodic film morphologies

5.1.1 Barrier layer and bottom film section

The expected morphologies were based on previous work [8, 10] in which a linear relation was proposed between anodic voltage and pore diameters d , cell diameters c and barrier layer thickness b :

$$d = \delta \cdot V \quad (13)$$

$$c = \varepsilon \cdot V \quad (14)$$

$$b = \gamma \cdot V \quad (15)$$

As described above, experimental SAA films resemble the expected ones quite well. Whether the above relations are really valid is however hard to determine, since no detailed pore and cell measurements could be made on broken SAA films.

For PSA, the above relations only seem to be valid for the bottom sections of the anodic film, close to the barrier layer. Whether this part of the film really has a “Keller-Hunter-Robinson”-morphology can be tested by plotting pore diameters, cell diameters and barrier layer thicknesses measured in the bottom film section (Table 9, §4.3.1) against the final anodizing voltage (Figure 54). Only voltage cycles 2, 5 and 7, with a long period of constant voltage towards the end, were included in this plot.

(a) PSA morphology bottom film section vs final anodizing voltage

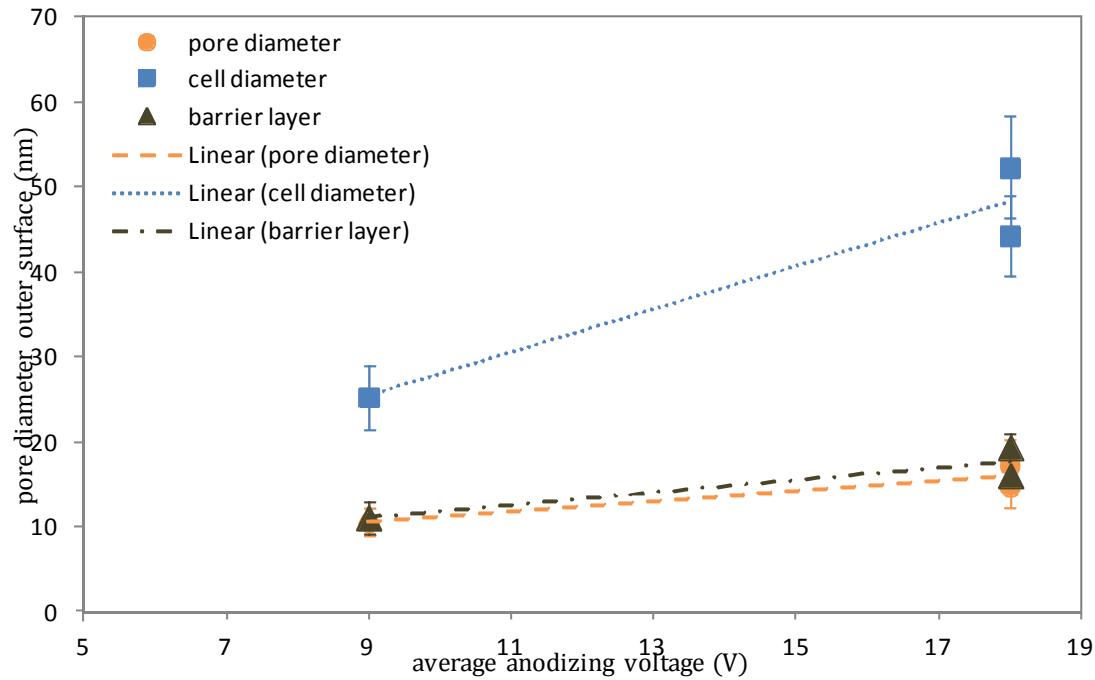


Figure 54. Pore diameters, cell distances and barrier layer thicknesses in PSA vs final anodizing voltage. Anodizing was done at 28°C for 30min, voltage cycles 2, 5 and 7.

It was possible to fit the data points to linear lines, as shown in Figure 54. The slopes of these lines represent the linearity constants δ , ε , and γ from eqn. 9, 10 and 11, in nm/V. The best fit to the measured data is given by:

$$d = 0,6 \cdot V \quad (21)$$

$$c = 2,6 \cdot V \quad (22)$$

$$b = 0,7 \cdot V \quad (23)$$

The value of $\varepsilon = 2,6 \text{ nm/V}$ corresponds well to values that are commonly found in literature. O'Sullivan and Wood [8], for instance, found a nm/V ratio of 2,77 for the variation of cell diameter with voltage in 0,4M phosphoric acid at 25°C. The other two linearity constants, $\delta = 0,6 \text{ nm/V}$ and $\gamma = 0,7 \text{ nm/V}$ are somewhat lower than values reported in literature (O'Sullivan and Wood found $\delta = 1,29 \text{ nm/V}$ and $\gamma = 1,04 \text{ nm/V}$). Since only three data points were used for each fitting, more tests are needed to check the accuracy of these relations.

5.1.2 Solubility of aluminum oxide in sulfuric acid and phosphoric acid

Especially for prolonged anodizing, the morphology of PSA films becomes very coarse, especially in the upper part of the film. This does not occur with SAA films. It was shown in Figure 50 that both the average pore diameter and the interpore distance increase with anodizing time for PSA. The SAA surface morphology did not depend on anodizing time.

Since the only difference between PSA and SAA is the presence of phosphoric acid in the electrolyte, differences are likely to be caused by dissolution of the outer pore walls in phosphoric acid. Previous work has shown that the chemical dissolution rate of Al_2O_3 depends on the concentration of phosphoric acid in the electrolyte [16]. In contrast, the solubility of Al_2O_3 in sulfuric acid has found to be very low [17].

The fact that both pore diameters *and* cell diameters increase with time, tells us that pore walls do not only get thinner but completely dissolve in the electrolyte (see Figure 55). If only pore wall thinning would occur, the distance between two pores would not be changing. Oxide film dissolution in phosphoric acid thus causes complete or partial disappearance of the fine-featured section that was formed during the initial voltage sweep.

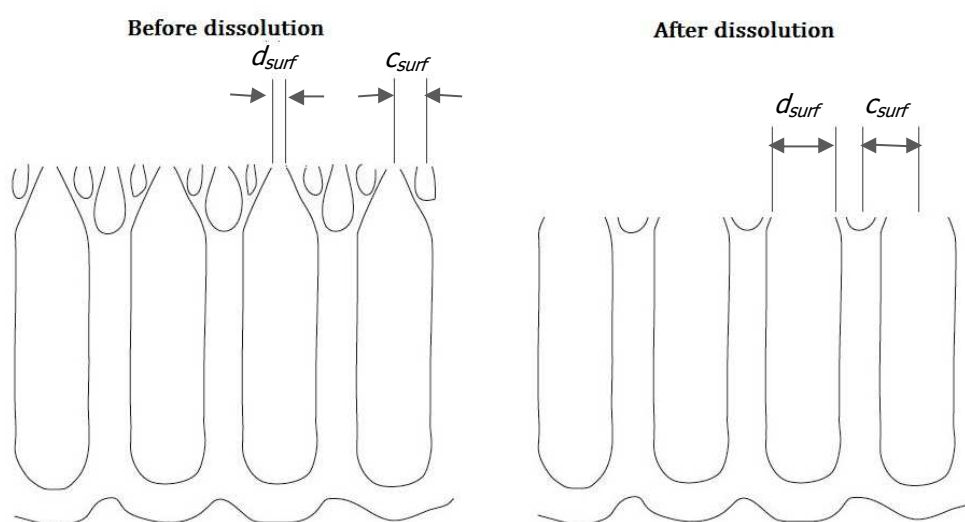


Figure 55. Dissolution of outer porewalls in phosphoric acid after prolonged anodizing in PSA

In literature, different opinions exist on the influence of the electric field on the oxide dissolution rate. It was suggested by some that the dissolution rate increases in the presence of a high external electric field at the tips of pores [8, 18], but experimental evidence for this has not been demonstrated [19]. Though no electric field strengths

were calculated in this study, the results presented in Figure 50 do suggest that the dissolution rate depends on the anodizing voltage, so probably on the electric field as well. Faster pore widening was namely found for cycles 1&2 (average voltage 17,7&17,1V, respectively) compared to cycle 3 (average voltage 8,8V).

Since film growth occurs at the aluminum/film interface, the bottom part of the anodic film has been in contact with the electrolyte only for a very short period. Therefore, it is not expected that dissolution significantly affects this part of the film. This also explains why PSA films resemble expected morphologies more in the bottom section than in the top section. Due to dissolution effects, the linear relations between anodizing voltage and pore and cell diameters are not valid for the upper section of PSA films.

5.1.3 Dependence of outer surface morphology on initial voltage sweep rate

All anodizing cycles applied during this study started with a voltage sweep. Larger pores and cells were found at the outer surface for PSA-cycles that had started with an 18V/min initial sweep rate, than for cycles that started with a 6V/min initial sweep rate (§ 4.3.2, Figure 51). To the author's knowledge, no previous work has been done on the relation between the initial voltage sweep rate dV/dt and the outer surface morphology.

To understand this phenomenon, a closer look will first be taken at the onset of pore formation during voltage sweeps.

For all cycles with an 18V/min or 6V/min initial voltage sweep followed by a period of constant voltage, it was shown that the i - t curve consists of five different stages (Figure 43 & Figure 56). Based on previous work by Ha and Jeong [20] and Curioni et al [13], an attempt is made to correlate each stage of the i - t curve to specific phases in the porous growth process:

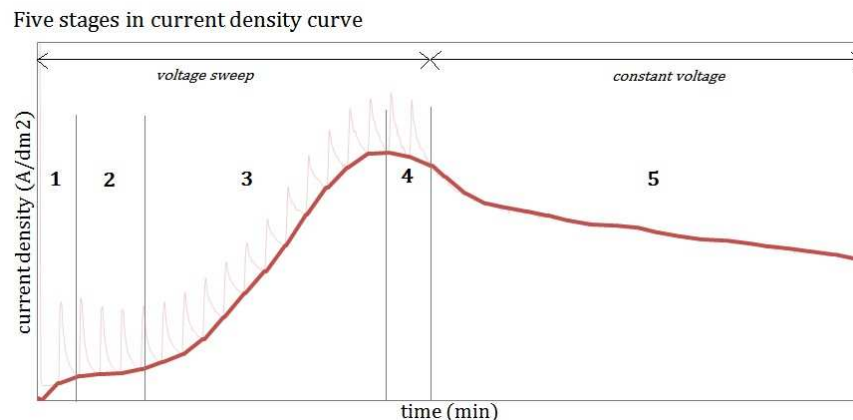


Figure 56. Five stages recognizable in current density curves for high voltage sweep rates followed by a constant voltage

1. A first increase in current density is attributed to the onset of ionic conduction across a pre-existing air-formed oxide film.
2. During the current plateau stage (constant current) a barrier layer is grown with a constant thickening rate. No pores have been formed yet at this stage. This seems reasonable, since a current plateau is *not* seen when a second voltage sweep is applied half-way the process (voltage cycle 5, Figure 44). This justifies

the statement that a current plateau belongs to a stage before pore initiation, since during the second voltage sweep pores already exist.

3. At the moment that the current plateau ends, pores start developing. The presence of pores eases current flow so the current increases again.
4. The porous structure continues to develop and since some pores stop growing due to competition among the pores, the current starts to decrease again.
5. When the final voltage has been reached, the current continues to decrease. Now, the decrease is not only attributed to redistribution of pores, but also due to limited flow of electrolyte in long pore channels diffusion, which decreases the amount of oxygen diffusing through the barrier layer for anodic oxide growth. Eventually, a steady-state value is reached.

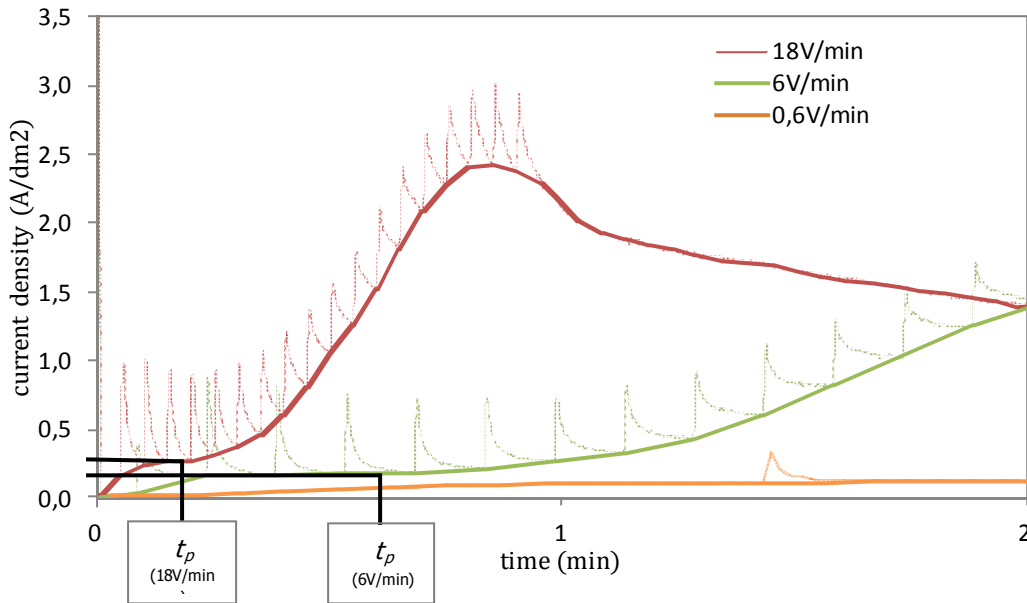


Figure 57. Identifying the moment at which the current plateau ends in i/t graphs (AA1050 PSA)

Pore formation commences when the current plateau ends at $t = t_p$, see Figure 57. In agreement with previous studies, e.g. [14, 70], plateaus were found earlier in time and at higher current densities for higher voltage sweep rates, due to the reduced time available for film generation. The current plateau of the 18V/min cycle ends at $t_p \approx 12$ sec. At that moment, the anodizing voltage was 4,4V. For the 6V/min cycle the current plateau ends at $t_p = 41$ sec, also at an anodizing voltage of 4,4V.

If the initial diameter of pores at the outer surface, $d_{surf,0}$ is linearly related to the potential V_p , at which pores start to form, the initial pore diameter is given by:

$$d_{surf,0} = \delta \cdot V_p, \quad (24)$$

where δ is a linearity constant. The same mechanism could be proposed for the initial surface cell diameter:

$$c_{surf,0} = \varepsilon \cdot V_p, \quad (25)$$

However, since the V_p -values were almost similar for both sweep rates, differences in outer pore diameter are still not explained.

An explanation for the differences in outer pore diameter could be that slower voltage sweeps last longer, which makes that a thicker part of the anodic film is formed during the sweep period. Figure 58 shows a 18V/min film with a thin 'sweep part', next to a 6V/min film with a thicker 'sweep part'. These 'sweep parts' of the anodic film are thought to exist of smaller pores and cells than the rest of the film, since they are formed at lower voltages. When the anodic film is subsequently attacked by the phosphoric acid electrolyte, the top layer of the film is dissolved. If the same amount of oxide is dissolved in both cases, the change in pore and cell diameter will be less for thicker 'sweep parts'. In other words, differences in outer surface morphology due to dissolution are expected to be less for low initial sweep rates than for high initial sweep rates.

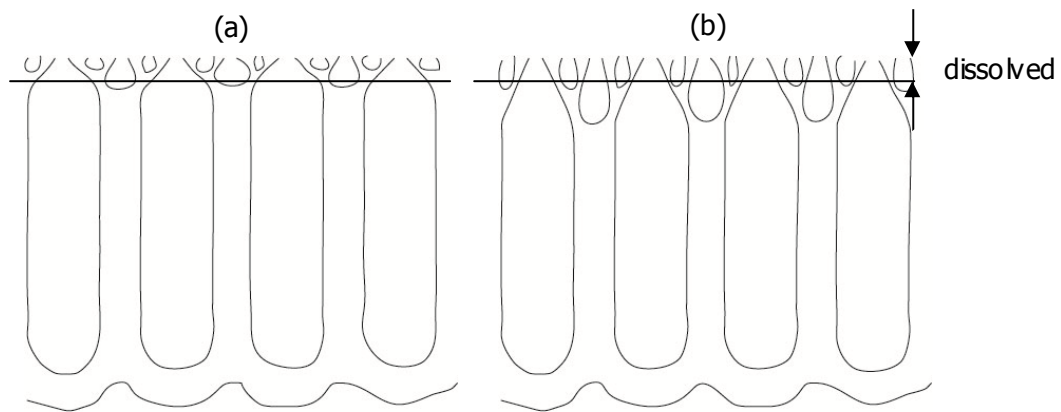


Figure 58. Anodic oxide films formed with a sweep rate of (a) 18V/min and (b) 6V/min, followed by a period of constant voltage $V=18V$

5.1.4 Recovery effect after half-way voltage step

During voltage cycles 5 and 7, the voltage was changed halfway the process in 1,5min from 9V to 18V, or the other way around. Previous studies, e.g. [8], have shown that when the anodizing voltage is changed very fast ($dV/dt \rightarrow \infty$), the system needs time to reach a new steady state situation with a new steady state current (recovery effect). In this study, the change in voltage was slower ($\pm 6V/min$), but a recovery effect was still observed (Figure 43).

O'Sullivan and Wood [8] described the underlying mechanisms of the recovery effect after a fast voltage change (§2.5.2). They describe that immediately after a voltage change, the barrier layer is thinner or thicker than its equilibrium value. Therefore, the current suddenly increases or decreases. The barrier layer needs to grow thicker or dissolve in the electrolyte, before the current can stabilize again. Also, pore diameters have to adapt to the new voltage. According to O'Sullivan and Wood [8], pore widening after a voltage increase happens through dissolution of the pore base, but no mechanism exists for decreasing pore sizes after a voltage decrease. This means that new pores with smaller diameters have to develop below existing pores.

Looking at the current density response curves (Figure 43) and SEM images of anodic film cross sections (Figure 46) of voltage cycles 5 and 7, O'Sullivan and Wood's ideas seem to be valid as well for the gradual voltage changes of 6V/min which were applied in this study. After an increase in voltage (Figure 46(c&d)), existing pores are widened at the pore base by chemical dissolution. Therefore, a gradual transition is seen between

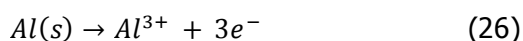
the region formed at 9V to the region formed at 18V. Such a transition region in the morphology is not seen after a decrease in voltage (Figure 46(a&b)). As explained above, no mechanism exists for decreasing the diameter of pores that are already formed, so the pore diameter of existing pores remains unaltered after a voltage change. Once the barrier layer has become thinner, new pores with a smaller diameter begin to grow below the larger existing pores. A clear border thus develops between the pores formed at 18V and those at 9V.

In previous studies [8], where the voltage was increased from 85 to 115V, or decreased from 115 to 85V, recovery times were found to be much shorter after a voltage increase than after a voltage decrease. The process of barrier layer thickening (oxide growth) was thought to be several orders of magnitude faster than barrier layer thinning (oxide dissolution) [21]. However, in this study the recovery time was longer after an increase in anodizing voltage than after a decrease. Possibly, when the process starts with a voltage of 9V, the pores that are formed then have such small diameters that electrolyte flow within the pores is difficult. When the voltage is subsequently increased to 18V, not enough water and oxygen can diffuse towards the barrier film/electrolyte interface. This slows down anodic film growth and increases the recovery time. When the process is started at a higher voltage, like 85V in the study by O'Sullivan and Wood [8], larger pores are formed. So when the voltage is then increased from 85 to 115V, diffusion of oxygen towards the barrier film is not hindered and the oxide growth rate can be very high. Limited diffusion of electrolyte in the pores might also explain why the recovery time is longer for SAA (small pores) than for PSA (large pores) after a half-way voltage step. After the initial voltage sweep, however, the recovery is longer for PSA. This could be due to higher oxide dissolution rate of anodic oxide in PSA, which makes that the system initially needs more time to find the balance between oxide growth and oxide dissolution.

5.2 Anodic oxide formation efficiency

During anodizing, a constant competition exists between oxide film growth and oxide dissolution in the electrolyte. If the film growth rate is high compared to the rate of dissolution, the efficiency of anodic oxide formation is high.

The results of this study have shown that a positive relation exists between the anodic oxide formation efficiency and the average anodizing voltage (Figure 52). The explanation for this is relatively simple: when the anodizing voltage is high, the current density through the system is usually also higher. The current density is a direct measure for the number of aluminum atoms being transformed into the corresponding cations, according to [22]:



Aluminum cations can subsequently react with oxygen-containing anions to form aluminum oxide, or be ejected to the electrolyte. The more aluminum cations are available for anodic film production, the faster the anodic film grows.

In §5.1.2, it was suggested that the oxide dissolution rate is also higher when the voltage increases. But apparently the effect of an increased voltage is larger on the oxide

growth rate than on the oxide dissolution rate. Otherwise, the anodic oxide formation efficiency would not be higher for increasing anodizing voltages.

A second interesting finding during this study was that the efficiency is lower for processes including a voltage decrease instead of a voltage increase, even when the average anodizing voltage was the same for both processes (Figure 52). The recovery effect, described in the previous section, could be a plausible explanation for this. After a decrease in anodizing voltage, the current density was temporarily lower than the steady state value. For an increase in anodizing voltage, the opposite was found. On average, the current density of the whole process is thus lower when the process includes a voltage decrease, which makes that the oxide growth rate is not so high anymore compared to the oxide dissolution rate.

6. Conclusions part A

Potentiodynamic anodizing experiments were performed on two aluminum alloys (AA1050 and AA2024-T3 clad) in two electrolytes (PSA and SAA) for different anodizing times (5min, 15min and 30min). Also, seven different voltage cycles were applied, which were based on common industrial voltages cycles. All voltage cycles included an initial voltage sweep (sweep rate dV/dt), followed either by a constant voltage or a dynamic voltage. It was analyzed how (1) the morphology of the anodic oxide films and (2) the oxide formation efficiency were dependent on the process parameters. Special attention was given to the influence of a changing (dynamic) anodizing voltage on the process.

6.1 Morphology of anodic film

In both SAA and PSA, porous anodic films were formed during all experiments. A first conclusion that can be drawn is that anodic films on AA1050 are almost identical to those on AA2024-T3 clad. This is in line with expectations, since the clad layer of AA2024-T3 is composed of AA1230, an alloy with a chemical composition which is very similar to that of AA1050. All other varied process parameters have a large influence on the anodic film morphology: the electrolyte, the anodizing time and the (dynamic) anodizing voltage

SAA pores have a much smaller diameter than PSA pores, which is consistent with data found in literature. The dimensions of SAA porous cells are – as expected on the basis of previous work – roughly proportional to the forming voltage. In contrast, PSA pores and cells are not always proportional to the forming voltage. Pores and cells can be larger in upper film sections than in bottom sections, even when they are formed at the same voltage. Also, SAA surface pore and cell diameters are independent of anodizing time, while the PSA film becomes very coarse after prolonged anodizing. These differences between PSA and SAA are caused by the higher solubility of Al_2O_3 in phosphoric acid than in sulfuric acid. The longer an PSA anodizing cycle lasts, the more dissolution of outer pore walls takes place which results in an increase in pore and cell diameters with time.

For PSA anodizing, the role of a dynamic anodizing voltage was studied in-depth. The voltage was found to influence the morphology as follows:

- In the film section close to the barrier layer, where dissolution does not play a role, dimensions of the porous cells and the barrier layer were found to be proportional to the anodizing voltage. However, the number of available data points for this analysis was very low, so more work is needed to confirm this statement.
- The higher the average anodizing voltage, the higher the rate of oxide dissolution in the electrolyte, which means that pore widening is more pronounced at higher average voltages. Dissolution is therefore likely to occur via a field-assisted mechanism.
- The faster the initial voltage sweep rate (dV/dt), the larger the pores and cells at the outer surface. A slower voltage sweep lasts longer, which leads to a thicker

'sweep part' in the top of the anodic film (existing of smaller pores and cells) than for faster sweep voltage sweeps. When pore walls subsequently dissolve in the electrolyte, this affects the pore and cell diameter less for thick 'sweep part' than for thin 'sweep parts'.

- After an increase in voltage half-way the anodizing cycle, existing pores are widened at the pore base by chemical dissolution. Therefore, a gradual transition is seen between the region formed at the lower voltage to the region formed at the higher voltage. Such a transition region in the morphology is not seen after a decrease in voltage. Since no mechanism exists for decreasing the diameter of pores that were already formed, new pores with a smaller diameter have to start growing below the larger existing pores. A clear border thus develops between the pores formed at the higher and the lower voltage.

6.2 Anodic oxide formation efficiency

The anodic oxide formation efficiency is the ratio of the measured film mass to the theoretical mass calculated from the charge passed. The efficiency is high when the oxide growth rate is high compared to the oxide dissolution rate.

For both SAA and PSA, it was found that the anodic oxide formation efficiency depends positively on the average anodizing voltage. When the anodizing voltage is high, the current density through the system is also higher. The current density is a direct measure of the number of aluminum cations that are being created, which are needed for anodic film production. So when the anodizing voltage increases, the film growth rate increases and the anodic oxide formation goes up.

However, when the process includes a decrease in voltage, the efficiency is lowered, even when the average voltage is equal to that of other processes. After a decrease in anodizing voltage, the current density is temporarily lower than the steady state value due to a recovery effect. On average, the current density of the whole process is thus lower when the process includes a voltage decrease, which negatively influences the anodic oxide formation efficiency. When the process includes an increase in anodizing voltage, the opposite is found.

PART B

ADHESIVE BONDING OF ANODIZED SUBSTRATES

7. Bibliography

7.1 Theories of fundamental adhesion

A fundamental understanding of adhesively bonded joints requires an understanding of the substrates and surfaces being bonded, the behavior of the adhesive, and stresses and strains within the bonded joint [71]. According to Packham [72], four “classic” theories of fundamental adhesion can be distinguished:

1. The adsorption theory
2. The mechanical theory
3. The electrostatic theory
4. The diffusion theory

The essential idea of the *adsorption theory* is that whenever two materials (usually a liquid adhesive and a solid substrate) come into contact on a molecular level, there will be an interaction between the two materials which we can call adhesion. A distinction can be made between primary bonds that involve sharing of electrons (ionic, covalent or metallic), and secondary bonds without sharing of electrons (hydrogen and van der Waals). The type of bond will depend on the chemical nature of the surfaces of the materials concerned [72].

The *mechanical theory* originates from a classical work by McBain and Hopkins that was published in 1925 [73]. McBain and Hopkins stated that “a good joint must result whenever a strong continuous film of partly embedded adhesive is formed in situ.” Basically, the mechanical theory tells us that the higher the surface roughness of the substrate, the higher the strength of the adhesive bond. This can be illustrated using [Figure 59](#), where a smooth surface is shown on the left and a rough surface on the right. Note that bulk atom (B) is bonded to six nearest neighbors, while surface atom (S) is only bonded to four and an atom on an asperity (A) to only two. When an atom has a number of nearest neighbors that deviates from the bulk value (in this case six), the atom finds itself in a higher energy state than the equilibrium value. A system always strives for the lowest possible energy state, so an atom on a rough surface with many asperities is more likely to bond to an adhesive than an atom on a smooth surface.

However, too much roughness also has its disadvantages. It can lead to incomplete wetting of the substrate by the adhesive. Voids will then be present at the interface, which will act as points of stress concentrations [72]. Using a viscous adhesive on a very rough surface can therefore lower the adhesive bond strength.

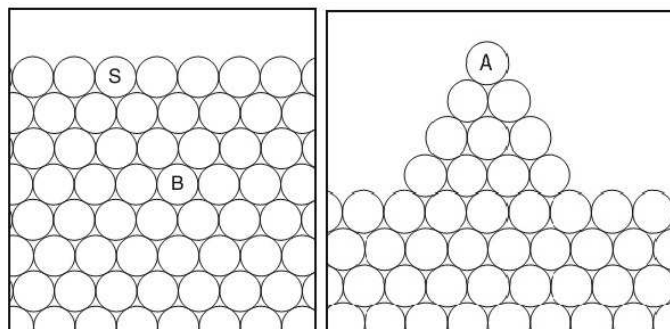


Figure 59. Schematic representation of an atom in the bulk of a material (B), on a plane surface (S), and on an asperity on a rough surface (A) [72].

The adsorption theory and mechanical theory are to a large extent interrelated. 'Adsorption' and 'mechanical' effects can rarely be considered isolated from one another. Both theories relate molecular dispositions in the region of the interface to macroscopic properties of an adhesive joint [74].

Both the *electrostatic* and *diffusion* theories originated in the Soviet Union and The Netherlands. The *electrostatic theory* was put forward by Deryagin and colleagues in 1940 [75]. The basis of this theory is that free charges exist to some extent in any condensed material, even in the best dielectrics. Therefore, an electrochemical potential will exist across the interface between adhesive and substrate material. Free electronic or ionic charge carriers will tend to move across the contact interface and an electric double layer is established. Many researchers, however, state that such electrostatic contributions are likely to be small compared to other forces involved in chemical bonding [72].

The *diffusion theory* was put forward by Voyutskii [76]. The theory postulates that molecules from two polymers in contact can interdiffuse, so that the interface becomes diffuse and eventually disappears. Since the theory has only been studied for polymer-polymer interaction it will not be further discussed here.

7.2 Initial bond strength

The question arises: which of the adhesion theories from section 7.1 apply to the interface between a porous anodic alumina film and an adhesive primer? In literature, two main theories are found regarding this matter.

The first theory is that penetration of the primer into the pores of the oxide is paramount in achieving superior adhesive bonds, e.g. [33, 56, 77]. An open pore structure, with pores wide enough to allow primer penetrating into them, would then be ideal. If this is true, oxide-primer adhesion could be explained using the mechanical theory that links good adhesion to a high surface roughness. This theory is questioned by Venables et al. [78] and Franz [79]. They used oxide surfaces of only 20-40nm thick as a substrate for adhesive bonding. High peel strength were found, which suggests that deep pore penetration is not a necessity.

A second theory on adhesive bond strength is that the chemical nature of primer and oxide determine the bond strength. It is considered that the molecular forces involved in

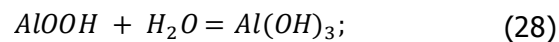
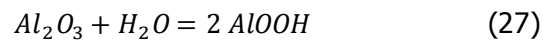
a primer/oxide bond include van der Waals forces (dipole forces), hydrogen bonds and ionic and covalent bonding [79-83]. Especially the presence of a hydrated form of the oxide - containing a high density of hydroxyls - would induce both improved wettability and chemical bonding [77]. According to Van den Brand et al. [84], the presence of hydroxyls gives a surface the capacity to form more bonds with organic functional groups. However, no attempts have yet been made to create anodic oxide films with different hydroxyl fractions to study the difference in bond strength with adhesive primers.

7.3 Durability

The most important environmental factors determining the durability of adhesive bonded aluminum joints are humidity, temperature and mechanical stress [85]. A high temperature and stress alone are usually not detrimental, but in the presence of water accelerated degradation takes place [85]. It has been shown that nearly all failures in aluminum adhesive joints in the aircraft industry have been initiated by moisture [86]. Water may enter the adhesive bond by bulk diffusion through the adhesive, by interfacial diffusion and through preferential paths such as cracks and defects [85].

Several failure modes for adhesively bonded aluminum joints were identified [85], which are schematically illustrated in Figure 60:

- A. cohesive failure within the adhesive. In the presence of water, the load bearing capacity of the adhesive can be lower due to plasticizing of the adhesive [87];
- B. disbonding at the interface between adhesive and primer.
- C. fracture within the primer layer, which is more likely to occur for thick primer layers or when the primer has been insufficiently dried or cured.
- D. disbonding at the interface between primer and anodic coating. In the presence of water the top monolayer of the oxide hydrates, which is believed to disrupt the chemical primer-oxide bond [88].
- E. Rupture of the anodic oxide film. This can happen as a result of the large volume increment of Al_2O_3 after hydration [89], according to the reactions



- F. bond line corrosion of the aluminum substrate, leading to fracture at the metal/oxide interface.

The adhesive type may also influence the durability of the bond, since components of the adhesive may leach out after the adhesive reacts with water. An alkaline environment is for instance formed in epoxies, which can attack of the aluminum oxide.

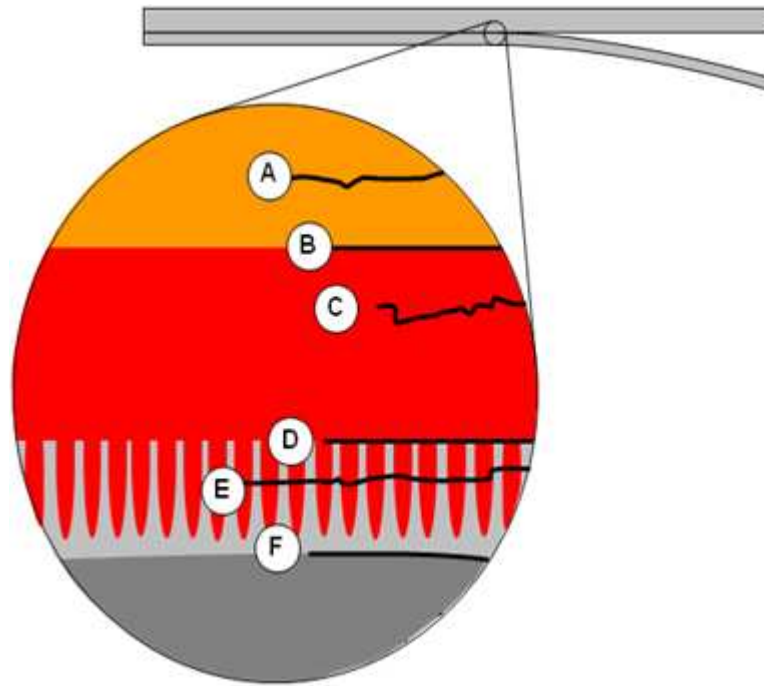


Figure 60. Possible failure mechanisms of an adhesive bond in the presence of moisture: (a) cohesive fracture of the adhesive film, (b) interfacial disbonding between adhesive and primer, (c) cohesive fracture of primer layer, (d) interfacial disbonding between primer and anodic coating, (e) fracture within anodic oxide coating and (f) corrosion of aluminum substrate at metal/oxide interface.

Failure paths of adhesive joints are often complex, but it has been shown that bond line corrosion (mechanism F in Figure 60) is the prime cause of environmental failure for clad aluminum joints [2]. Lunder [85] expects the corrosion mechanism to resemble that of filiform corrosion (FFC) of painted aluminum sheet material. The near surface microstructure of the aluminum substrate material is distinctly different from the bulk structure as a result of high shear and elevated temperatures during processing. This makes the material susceptible to superficial corrosion attack such as FFC. For the rest, little information is available on the role of corrosion mechanisms in aluminum adhesive joints [85].

8. Research approach

Anodic alumina films are thought to contribute to the performance of adhesively bonded structures in two ways [33, 90]:

1. the presence of a porous anodic film promotes adhesion between the primer and the aluminum substrate.
2. the thick anodic alumina film protects the aluminum substrate against corrosive environments,

However, the mechanisms behind adhesion promotion and corrosion resistance of adhesively bonded joints are not well understood. It is therefore unclear which anodic film morphology is optimal for adhesive bonding.

Part A of this report has shown that the voltage cycle applied during anodizing directly influences the morphology of anodic films. In this second part of the work, the performance of a bonded system was tested. Five bonded test panels were prepared. During pretreatment of aluminum before bonding, a different PSA anodizing voltage cycle was used for each panel.

The substrate material used to construct bonded specimens was AA2024-T3 clad, an alloy often used in adhesive bonds. The primer and adhesive materials were both Cr(VI)-free. The materials are chosen in such a way that results of the current work can be compared with results from other studies.

Analysis of the bond performance started with determination of the penetration of the primer into the anodic oxide film. Subsequently, the bond strength of the panels was tested under dry and wet conditions by means of a Floating Roller Peel Test ("Bell Peel" Test). The corrosion resistance was tested by means of a Bond Line Corrosion Test (BLC). The Bell Peel and BLC tests are commonly used in aerospace industry for process development and qualification.

9. Experimental procedure

9.1 Overview

An overview of the experimental work performed in part B is given in Figure 61.

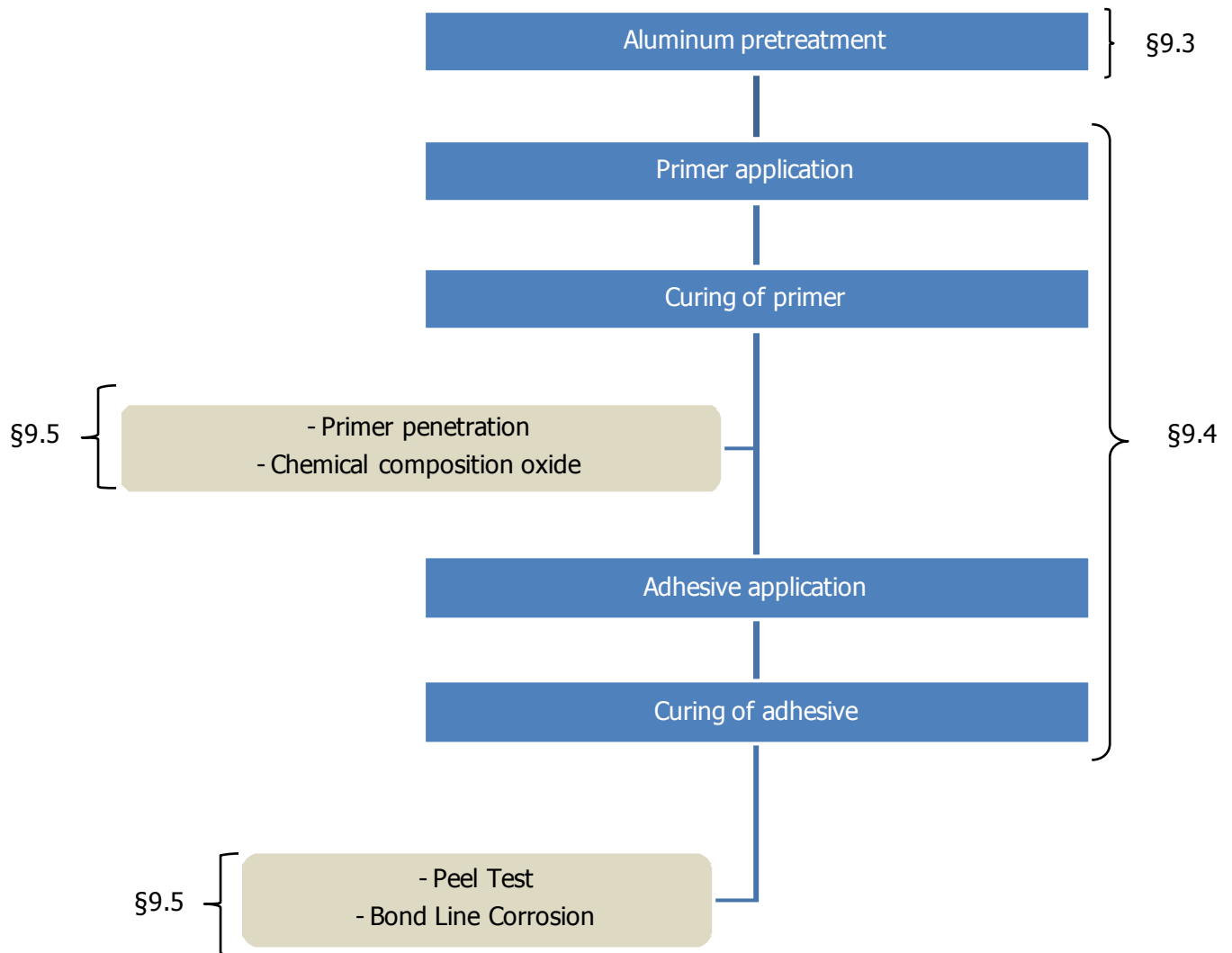


Figure 61. Overview experimental work part B

9.2 Materials

- a) Aluminum panels alloy AA2024-T3 clad (clad layer AA1230). For details: see §3.2
 - Specimen size:
 - 100x100x1.0mm for primer penetration study
 - 255x120x1.6mm
 - 300x120x0.5mm
- b) Structural adhesive primer Redux 101:
 - Chemical composition: 60-100% methanol, 1-5% phenol formaldehyde resin [91]
 - Supplier: Hexcel Composites
- c) Structural adhesive film AF 163-2K.06:
 - Chemical composition: 40-70wt% polymeric epoxy reaction product (M.W.>700), 10-30wt% epoxy resin (1), 3-7wt% epoxy resin (2), 3-7wt% dicyandiamide, 0,5-1,5 wt% N,N'-(Methyl-1,3-Phenylene)bis(N,N'-Dimethylurea), 0,1-1wt% 3-(Trimethoxysilyl)Propyl Glycidyl Ether [92]
 - Supplier: 3M

9.3 Aluminum pretreatment

Four plates AA2024-T3 clad were pretreated simultaneously per run: 2 pieces 100x100mm, 1 piece 255x120mm and 1 piece 300x120mm, which were clamped in a titanium rack. A detailed description of the pretreatment procedure can be found in part 1, §3.3. The voltage cycles applied during anodizing were cycle 2, 4, 5, 6 and 7. For clarity, these cycles are presented again below in Table 12.

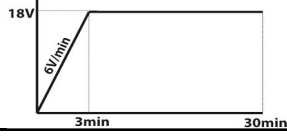
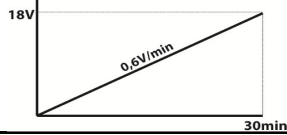
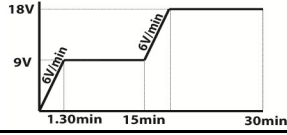
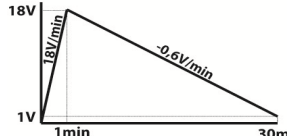
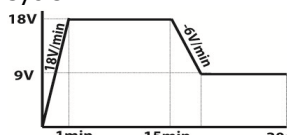
Voltage cycle	Al alloy	Electrolyte	Anodizing time (min)
Cycle 2 	AA2024-T3 clad	PSA	30
Cycle 4 	AA2024-T3 clad	PSA	30
Cycle 5 	AA2024-T3 clad	PSA	30
Cycle 6 	AA2024-T3 clad	PSA	30
Cycle 7 	AA2024-T3 clad	PSA	30

Table 12. Anodizing voltage cycles AA2024-T3 clad

9.4 Primer and adhesive application & curing of the system

All AA2024-T3 clad sheets were covered with structural primer, except for one sheet with dimensions 100x100x1.0mm which was used for SEM analysis (Part A). The primer was cured in an oven, starting at a temperature of 40°C, followed by an increase of 10°C/min and a subsequent period of 60-90min at 125±5°C.

The two largest Al primed sheets of each run (255x120x1.6mm and 300x120x0.5mm) were adhesively bonded with adhesive film according to the configuration shown in Figure 62. In total, five bonded panels were produced in total, one for each of the five voltage cycles. Curing of the adhesive was done in an autoclave under a pressure of 600±10kPa at 125±5°C.

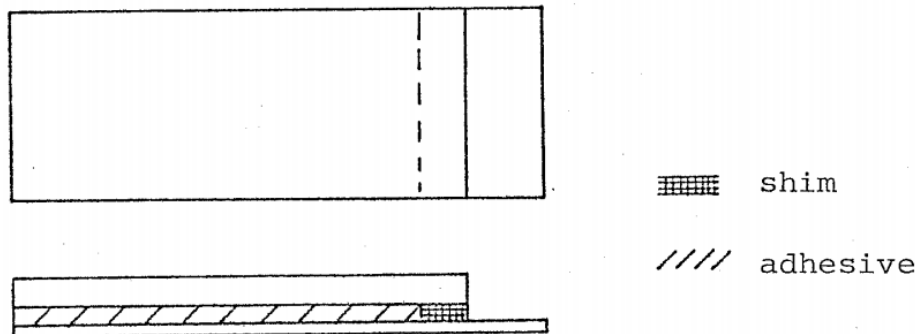


Figure 62. Two AA2024-T3 panels (255x120x1.6mm and 300x120x0.5mm) bonded with adhesive film

9.5 Analysis

9.5.1 Chemical composition by EDX

Of the 100x100x1,0mm sheets that were only primed, specimens were prepared for Energy Dispersive X-ray Spectroscopy (EDX) analysis. Of each primed sheet, a small piece was cut with a diamond saw (Figure 63) and placed under an angle of 10° in a polymer holder, which was especially designed for this purpose (Figure 64). The specimen was covered with resin and cured at ambient temperature. Subsequently, the surface of the specimen was polished to uncover a skewed cross section Al/oxide/primer (Figure 64). A layer of ±2nm of Pt was applied on the polished surface to prevent charging.

The EDX analysis was conducted with an X-MAX system from Oxford Instruments, embedded in Hitachi S-3700N SEM at the Energy Centre of The Netherlands (ECN) in Petten. The accelerating voltage was 15kV and the working distance 10mm.



Figure 63. Cutting of primed plates with diamond saw

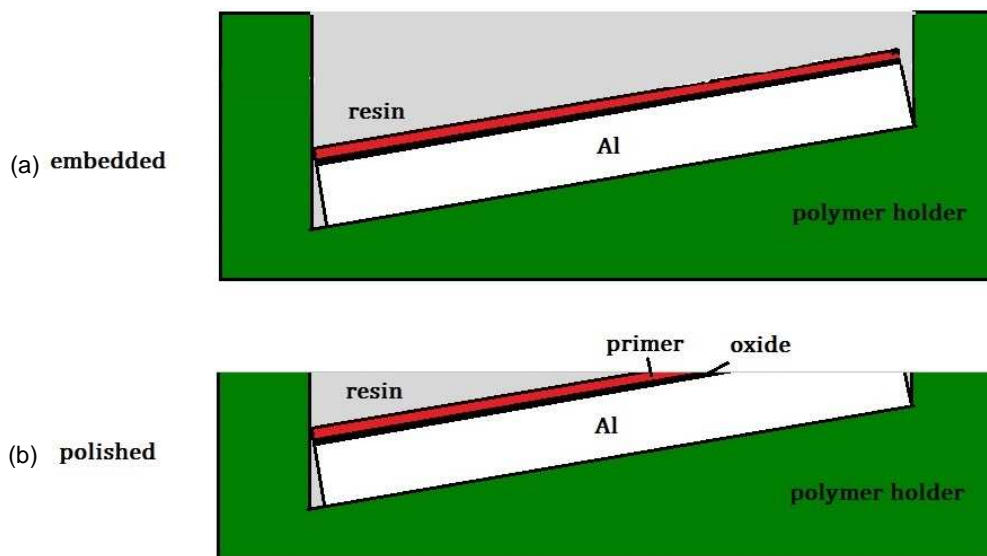


Figure 64. EDX sample preparation (a) before polishing and (b) after polishing, revealing a skewed cross section of a primed specimen.

9.5.2 Floating Roller ('Bell') Peel testing

Adhesive bond strength was tested by means of the Floating Roller Peel test, also called the Bell Peel test.

Of each bonded panel, three specimens were cut with a standard band saw to dimensions adequate for the Bell Peel testing (25x250mm). Of the remainder of the panel, two specimens were cut for BLC testing (§9.5.3). A detailed sawing scheme is shown in Appendix 4.

After fixing the Bell Peel specimen in the apparatus, the unbounded end of the specimen was attached to the lower head of the testing machine (Figure 65). The thin aluminium part was peeled off the thick part with a speed of 100mm/min. The peeling load versus

head movement (or load versus distance peeled) was recorded. All tests were performed at ambient temperature. The first half of the specimen was peeled under dry conditions and the second half under wet conditions.

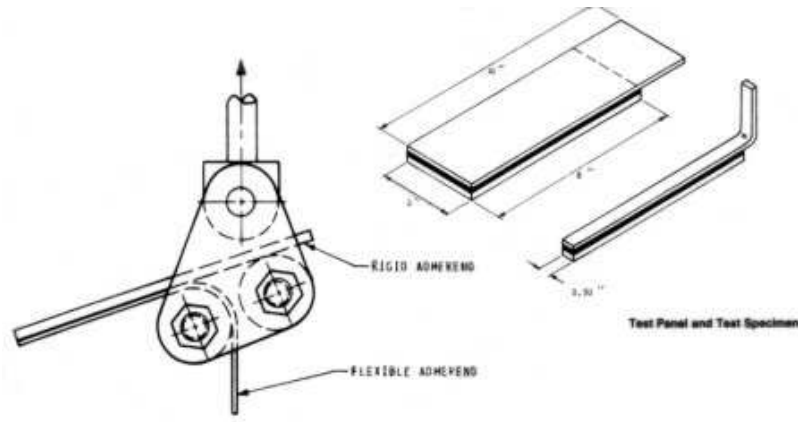


Figure 65. Bell Peel experimental set-up

9.5.3 Bond Line Corrosion

The resistance of the adhesive bond against bond line corrosion (BLC) was tested by placing bonded specimens for a prolonged period in a salt spray cabinet (Figure 66). Two specimens with a size of 18x200mm were cut of each bonded panel (detailed sawing scheme can be found in Appendix 4). This was done with a standard band saw. The first BLC sample was placed in the salt spray cabinet for 31 days, the second sample for 90 days. After these periods, the specimens were opened and corrosion percentages were measured on both the tick and the thin sheet of the bonded specimen. Only the results after 31 days of salt spray exposure are presented in the current report.



Figure 66. Bonded specimens in salt spray cabinet [93]

10. Results

10.1 EDX mappings of primed specimens

SEM micrographs of primed specimens (cross sections) are shown in Figure 67 (left side). The carbon distributions throughout the aluminum, anodic film and primer are shown in the same figure (right side). A red color in the images indicates a high carbon content at that specific location. The lines visible in the EDX image of cycle 2 are attributed to imperfect polishing of the specimen surface, and not to primer penetration into the pores. The width of the lines is namely much larger than the diameter of the pores.

Since the primer is a polymeric compound, it obviously contains a high amount of carbon. This explains the bright red areas at the top of each EDX image. Carbon is also detected in the anodic oxide for cycles 6 and 7, but hardly any carbon is found in the cycle 4 and 5 films. For cycle 2, it is hard to tell whether carbon is present in the oxide film due to the presence of the polishing lines on the surface. For all cycles, almost no carbon was detected in the aluminum substrate.

EDX was also used to determine the chemical composition of the anodic oxide film (see the 'spectrum' boxes in Figure 67). Next to aluminum, oxide and carbon - the main elements of a primed anodic film - small amounts of sulfur ($\leq 1,4$ wt%) and phosphor ($\leq 0,3$ wt%) were measured.

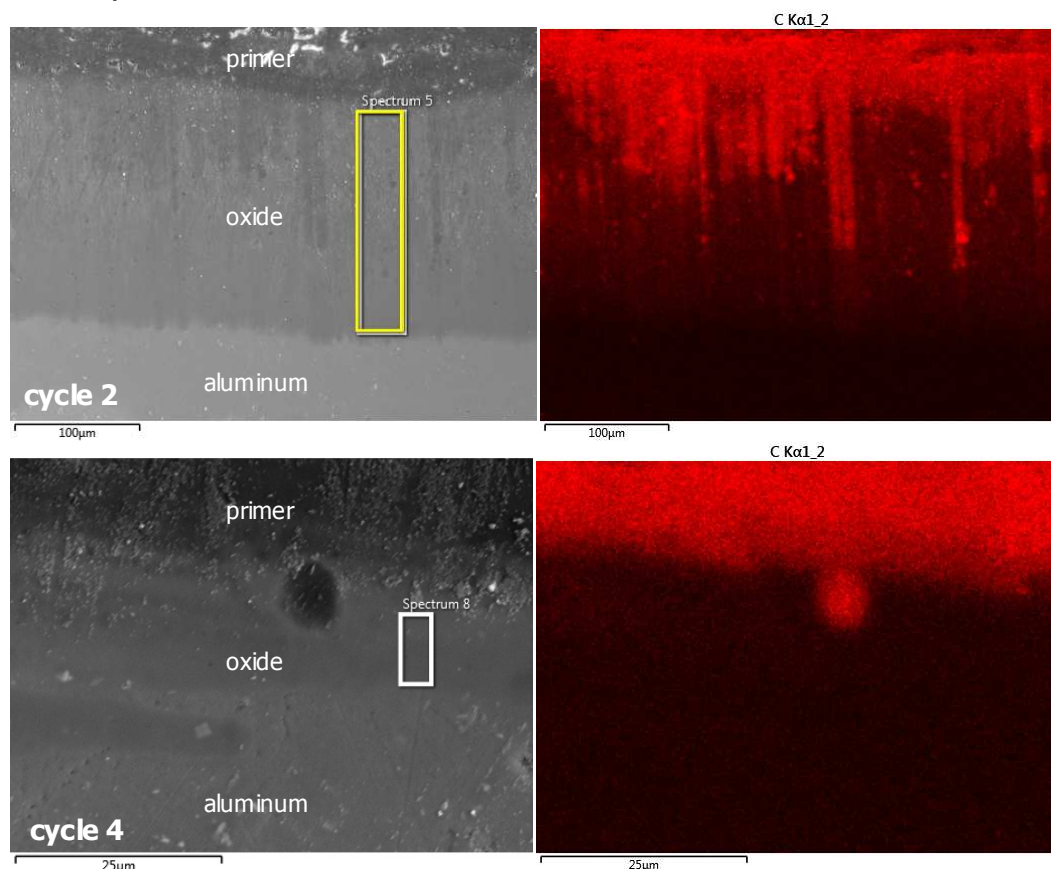


Figure 67 (part 1). SEM images (left) and EDX carbon mappings (right) of skewed cross sections of primed specimens.

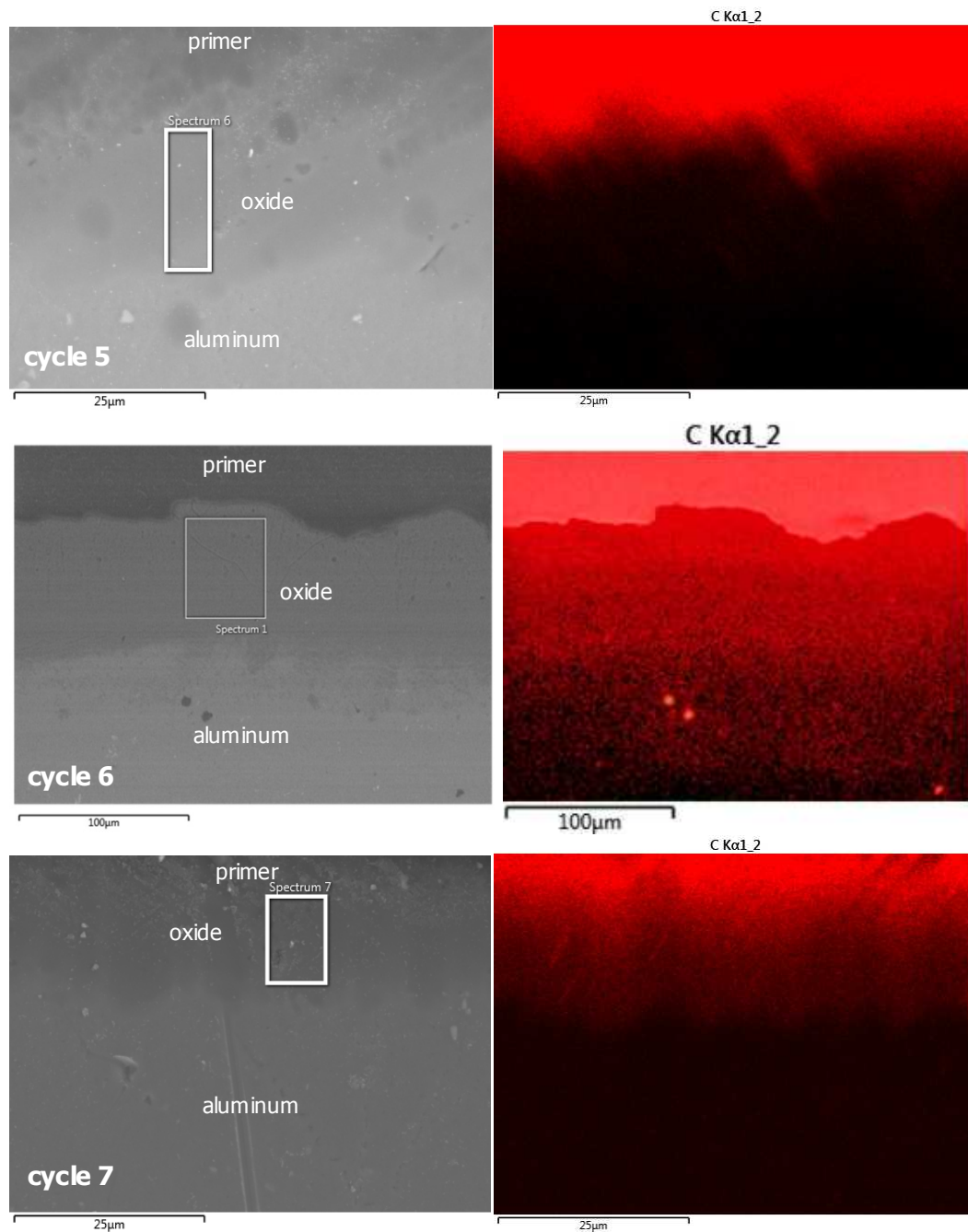


Figure 67 (part 2). SEM images (left) and EDX carbon mappings (right) of skewed cross sections of primed specimens.

10.2 Bell Peel testing of bonded specimens

Figure 68(a) shows a typical load vs displacement curve (cycle 5 specimens) as recorded during Bell Peel testing. The first couple of mm could be peeled easily (low load) due to the presence of a shim in this region. Afterwards the load needed for peeling increased quickly to a higher value. The variation in test results between the three Bell Peel specimens from one bonded panel was low.

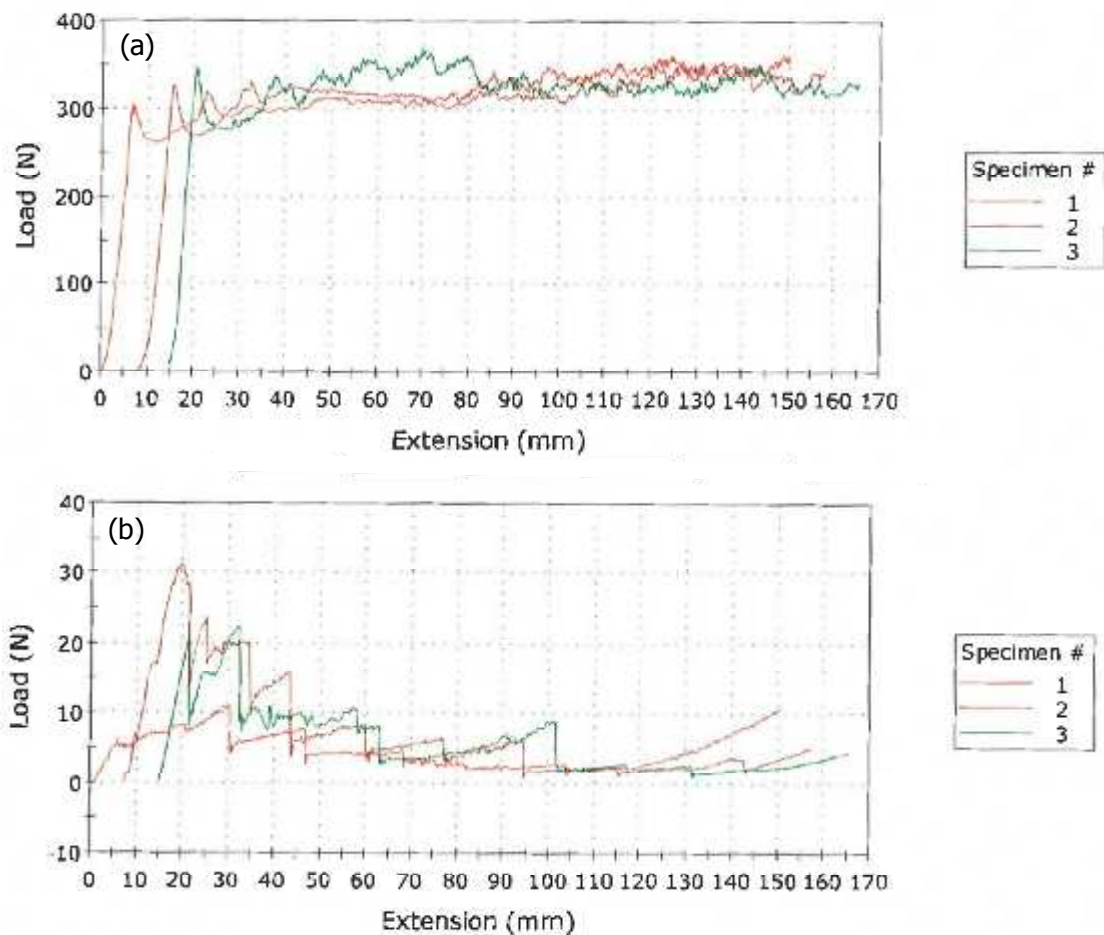


Figure 68. Load vs displacement curve of Bell Peel test (a) cycle 5 and (b) cycle 6

Table 13. Averaged Bell Peel results per run

Voltage cycle	Average bond line thickness (mm)	Average load dry (N)	Standard deviation load dry (N)	Fracture mode dry	Average load wet (N)	Standard deviation load wet (N)	Fracture mode wet
2	0,25	304,6	3,2	Cohesive	316,3	30,3	Cohesive
4	0,27	302,2	7,1	Cohesive	328,9	1,1	Cohesive
5	0,25	319,1	17,1	Cohesive	334,0	6,8	Cohesive
6	0,24	7,3	1,6	Adhesive	2,7	0,4	Adhesive
7	0,26	244,0	32,2	Cohesive	251,5	30,3	Cohesive

Average Bell Peel results, obtained under both dry and wet conditions, are summarized in Table 13. The panels from cycle 2, 4 and 5 show very similar behavior; average fracture

loads were $\pm 310\text{N}$ and $\pm 325\text{N}$ for the dry tests and wet tests, respectively. The peel strength of the last panel (cycle 7) was somewhat lower.

An interesting case is provided by cycle 6. These specimens failed at extremely low loads, as displayed in Figure 68(b). The average failure loads were 7N and 3N under dry and wet conditions, respectively. Inspection of the fracture surfaces (Figure 69(a)) showed that almost no adhesive or primer was left on the surface after peeling, which indicates that the bond failed adhesively. Specimens from all other cycles failed cohesively and had adhesive or primer left on the surface (Figure 69(b))

The majority of the specimens that failed cohesively had higher failure loads under wet conditions than under dry conditions.

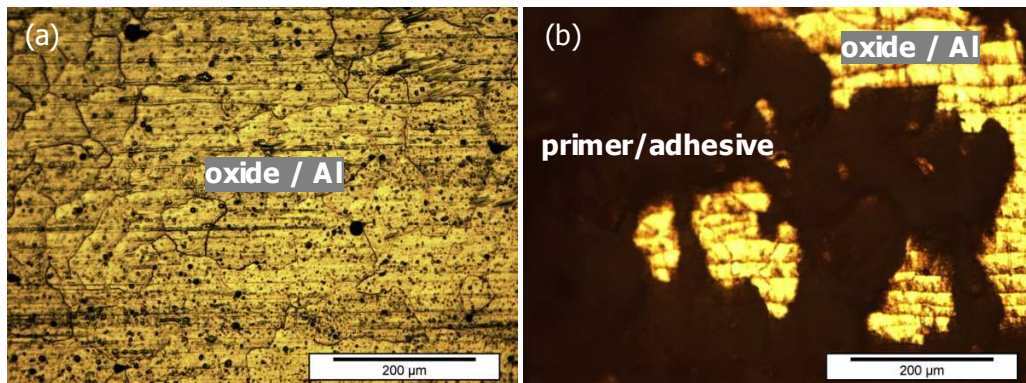


Figure 69. Aluminum surface of thin sheet after Bell Peel (a) voltage cycle 6 and (b) voltage cycle 2, representative of all cycles except for cycle 6

10.3 Bond Line Corrosion of bonded specimens

After 31 days of salt spray exposure, bonded specimens were opened and the amount of corrosion on the thin sheet was determined (Figure 70). A large part of the surface area of the voltage cycle 6 sheet was corroded, against only a small percentage for the other cycles.

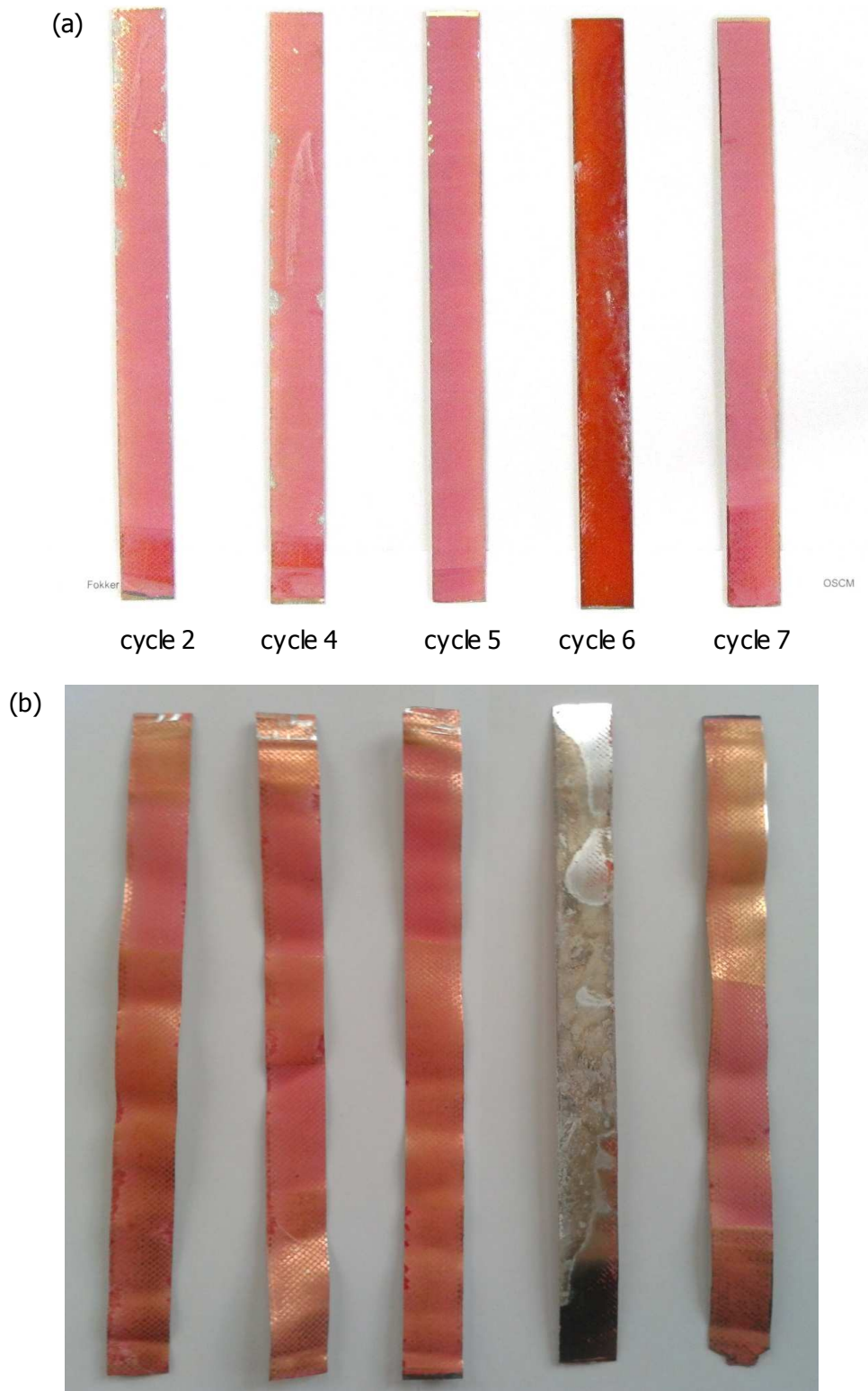


Figure 70. Bond line corrosion on (a) thick and (b) thin sheet of bonded panel after 31 days of salt spray exposure

10.4 Overview

Table 14 provides an overview of the results found in this part of the work (part B), together with anodic film morphologies of the substrate material (part A).

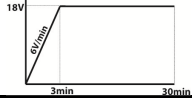
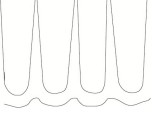
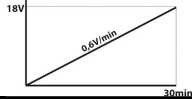
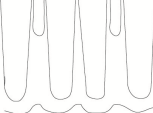

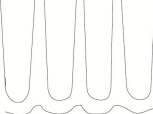

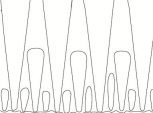

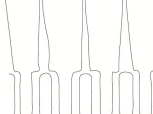
Voltage cycle	Measured morphology	Mean pore diam outer surface (nm)	Mean pore diam bottom section (nm)	Mean barrier layer thickness (nm)	Carbon content in film	Average peel strength dry (N)	Average peel strength wet (N)	Bond Line Corrosion
cycle 2 		32	15	16	high ⁶	304,6	316,3	low
cycle 4 		17	20	20	low	302,2	328,9	low
cycle 5 		17	17	20	low	319,1	334,0	very low
cycle 6 		19	12	6	high	7,3	2,7	high
cycle 7 		33	11	16	high	244,0	251,5	very low

Table 14. Overview of results part B, together with schematic presentation of anodic film morphologies from part A

⁶ Amount of carbon penetration uncertain due to problems with polishing of the surface

11. Discussion

11.1 Primer penetration

Since primers contain a lot of carbon, the amount of carbon in the anodic film indicates how much primer has penetrated into the film. However, it has to be emphasized that carbon measurements performed with EDX on skewed cross sections are not 100% reliable. This is due to the following reasons:

- there can be a significant carbon background signal, since hydrocarbon contamination is usually present at the chamber surfaces, vacuum pumps and specimen surface [94]
- cross sections of the anodic film are made in a skewed manner, which means that the thickness of the anodic coating is not the same at every location.

Nevertheless, the EDX mappings provide enough information for stating that the specimens from cycles 6, 7 and probably 2 contain more carbon in the oxide layer than those from cycles 4 and 5. So, it is reasonable to assume that more primer has penetrated into the anodic films of cycles 6 and 7, and probably 2 than into those of cycles 4 and 5.

From the results shown in Table 14 it is deduced that the carbon content in the oxide film, and thus the primer penetration, are related to the outer surface pore diameter. Apparently, the viscosity of the Redox 101 primer is too high to penetrate the film when the pores of the anodic film are very small.

11.2 Initial bond strength

A peel strength of $\pm 300\text{N}$ was measured for specimens of cycle 2, 4 and 5. The strength of the last panel (cycle 7) was somewhat lower, but this small load variation might be explained by the fact that the cycle 7-panel was primed and bonded on another day than the first three panels. Possibly, a different batch of adhesive - with a slightly lower tensile strength - was used on the second day.

A high peel strength indicates that cohesive failure of the bond has occurred, which in turn means that the adhesive bulk material fails before debonding of the primer/oxide bond or aluminum/oxide takes place. Interestingly, peel strengths under wet conditions were slightly higher than under dry conditions. Toughening of the adhesive material under influence of water might be an explanation for this.

One specimen (cycle 6) showed a completely different behavior during peel tests than the other specimens. For this specimen, peel strengths were never higher than 10N. It has been often stated in literature that peel strengths are mainly determined by the amount of primer penetration in the film, but this reasoning does not apply here. EDX mappings clearly show that primer has penetrated into the cycle 6 specimen.

But if primer penetration doesn't play a role, why then did one of the specimens fail at a much lower load? The low strength of the specimen might be caused by its anodic film

morphology, which deviates a lot from other morphologies. As shown in Table 14, the cycle 6-film has very small pores in the bottom section of the film, combined with a very thin barrier layer. No other anodic film has a region with such a fine-featured morphology. Most probably the oxide has ruptured at this location, causing adhesive failure instead of cohesive failure. This line of reasoning is supported by the optical micrographs shown in Figure 69, where no adhesive film or primer is seen on the aluminum surface after peel testing. This indicates that failure must have occurred either at the oxide/primer interface, within the oxide or at the oxide/metal interface.

11.3 Durability of the adhesive bond

All bonded specimens, except for the cycle 6 specimen, showed good resistance against bond line corrosion. Possibly, the low corrosion resistance of the cycle 6 specimen is related to the anodic film morphology (see Table 14), since the barrier thickness of this specimen is only 6nm. This is considerably thinner than for all the other voltage cycles.

Some believe that the bond line corrosion mechanism of adhesive bonds resembles the filiform corrosion mechanism (FFC) of coated aluminum [85]. The exact mechanism of FFC is unknown, but it has been shown that oxygen, aggressive ions such as chloride (Cl⁻) and a high relative humidity must all be present for FFC to occur [95, 96]. As explained in §7.3, water may enter the adhesive bond by bulk diffusion through the adhesive, by interfacial diffusion and via preferential paths such as cracks and defects [85]. Of these effects, bulk diffusion through the adhesive is expected to be the most prominent one. Since the edges of the BLC specimens are not coated, water can easily enter the adhesive layer from the side. It is proposed that water does not stay only in the adhesive but that it diffuses into the primer and eventually reaches the anodic oxide surface. It could be that the thickness of the barrier layer determines how quick the water reaches the aluminum substrate. The longer it takes for water to reach the aluminum substrate, the lower the corrosion rate will be. Specimens with a very thin barrier layer, like the cycle 6 specimen, are therefore expected to be less resistant against bond line corrosion.

However, the mechanically deformed surface layers on the aluminum substrate, caused during sheet production by the supplier, can also accelerate corrosion significantly. By using material from one batch for all experiments the intention was to minimize the influence of flaws in the substrate material, but differences within one batch might still exist. Further research is needed on the separate effects of the anodic film morphology and the characteristics of the aluminum substrate on the resistance against bond line corrosion.

12. Conclusions part B

In this part of the work five AA2024-T3 bonded specimens were analyzed. The aluminum sheets used to make the bonded specimens each received a different PSA anodizing pretreatment, such that they had different anodic oxide films on the surface.

It was found that anodic films having large diameters at the outer surface result in deeper primer penetration. Apparently, the viscosity of the applied primer was too high to penetrate very small pores.

Secondly, specimens having a fine-featured morphology failed at very low loads during peel testing. So if the pore and cell diameters are very small in a certain region of the oxide film, it is possible that the oxide ruptures before cohesive failure of the adhesive film occurs.

The rate of bond line corrosion seems to be related to the thickness of the barrier layer. Thick barrier layers can provide high resistance against hydration of the aluminum substrate, while water easily diffuses through thin barrier layers. However, the mechanically deformed layers present on top of the aluminum substrate can also decrease the corrosion resistance of the bond. This effect has not been examined here.

GENERAL CONCLUSIONS

In the first part of this work, potentiodynamic anodizing was performed on AA1050 and AA2024-T3 clad specimens in PSA and SAA. Subsequently, PSA anodized AA2024-T3 sheets were adhesively bonded in the second part of the work.

It has been shown that pore, cell and barrier layer dimensions are dependent on the anodizing voltage. The lower the anodizing voltage, the smaller the pores and cells and the thinner the barrier layer. By changing the anodizing voltage during the anodizing process, differences in morphology are developed across the film thickness. Film growth takes place at the aluminum/oxide interface, which means that the structure that develops first will eventually be at the outer surface. The final voltage determines what the structure close to the barrier layer looks like.

A large difference was observed between films that are formed in SAA compared to PSA. SAA-films were found to be very thick and pore diameters were very small ($\pm 10\text{nm}$). PSA pores and cells were larger, especially after prolonged anodizing. This difference is attributed to the higher solubility of aluminum oxide in phosphoric acid than in sulfuric acid.

All anodizing experiments started with a voltage sweep, during which the voltage was linearly raised to a final value. The voltage at which pores started to form was found to be independent of the voltage sweep rate. However, after prolonged anodizing in PSA, outer surface pores were smaller for specimens that received a slower initial voltage sweep. This is because the 'voltage sweep part' of the oxide (composed of small pores, formed at low voltages) is thicker for slow voltage sweeps than for fast ones, simply because slow sweeps last longer than fast sweeps. When the top layer of the film is affected by dissolution in phosphoric acid after prolonged anodizing, the fine-featured 'sweep part' of a fast-sweep oxide film is dissolved quicker than that of a slow-sweep film.

Also, the effect of a half-way voltage step was studied. Although the voltage was changed slower than in previous works, similar effects were found. Upon an increase in voltage, pore widening occurs through dissolution of pore walls at the pore base. No such mechanism exists for decreasing the pore diameter after a voltage decrease, so new pores have to develop below existing ones. As such, a clear border between small and large pores develops after a decrease in voltage, while such a border is absent after an increase in voltage.

Five pairs of aluminum sheet material, each pair having an anodic film with a completely different morphology, were selected to be bonded and further analyzed. A first interesting finding was that the amount of primer penetration into the anodic film was dependent on the pore diameter. For films with a large pore diameter at the outer surface, the primer could penetrate the film more easily.

The peel strength and corrosion resistance of the bonded panels were also tested. Peel strength was not, as proposed by many authors, determined by the amount of primer penetration. Even films that showed almost no primer penetration could have good peel results. The only bond that failed at very low loads was the one having both very small pores and a thin barrier layer in the bottom section of the film. It is thus possible that having a very fine featured region in the film (formed at low voltages) is not beneficial for adhesive bond performance, since rupture of the oxide could occur at this location.

The corrosion mechanism of bonded systems is very complex and it is hard to draw conclusions from the conducted experiments. It seems like the rate of bond line corrosion is related to the thickness of the barrier layer, since the barrier layer provides resistance against hydration of the aluminum substrate. Other parameters, like the initial surface characteristics of the aluminum substrate, might however also influence the corrosion resistance of the bond. This has not been examined in this work and needs further attention.

In summary, this work has shown that anodic film morphologies can be 'customized' by choosing specific anodizing process parameters. Desired pore and cell diameters can be obtained throughout the film thickness by choosing the right voltage profile. However, the effect of the high rate of oxide dissolution in phosphoric acid has to be taken into account, because this leads to pore widening after prolonged anodizing. By constructing the right anodic film morphology, it seems possible to influence the strength and corrosion resistance of adhesively bonded aluminum joints. Based on the results of this work, it is suggested that the optimum voltage cycle for PSA meets the following requirements:

- a fast initial voltage ramp, to have large surface pore diameters which facilitates primer penetration;
- no long periods of low voltage, especially not at the end of the cycle, since this leads to a thin, weak oxide structure around the barrier layer;
- include an increase in voltage in the cycle rather than a decrease in voltage, to maximize the efficiency of the process.

RECOMMENDATIONS

Experimental set-up

A semi-industrial scale anodizing test system was used for a fundamental investigation of the anodizing process. Many adjustments had to be made to the experimental set-up so that process parameters could be accurately controlled and recorded. A datalogger was connected for accurate data acquisition of the anodizing voltage and current, the temperature control was improved and it was made sure that the level of agitation was kept constant for all experiments. Despite these efforts, it remains questionable whether a large set-up is suitable for fundamental materials science studies. For future work, it is therefore recommended to do experiments in a lab-scale environment, where process parameters can be better controlled. For instance, most of the experiments were now done using a two-electrode set-up without reference electrode, while a three-electrode set-up could be used at all times in a lab-scale environment. Also, lab potentiostats are able to apply almost linear voltage sweeps instead of the step-wise voltage increases of $\pm 1\text{V}$ which were applied in this work. It would also be easier to keep the level of agitation and the electrolyte temperature constant in a small-scale set-up. In future studies it is recommended to not only measure temperature variations of the electrolyte, but to connect a thermocouple to the actual anodizing specimen as well.

If experiments are done in a semi-industrial set-up after all, it is advisable to do an in-depth study on the effect of the titanium rack on the anodic film growth. Preferably, experiments are done without the rack, but when one wants to anodize multiple sheets in one run it is difficult to do this without the rack. In that case, one should at least know to what extent the rack and the number of sheets in the rack influence the results.

Pretreatment prior to anodizing

In the current work, AA1050 specimens were only degreased before anodizing, while AA20240-T3 clad specimens were degreased, etched and de-smutted. More work is needed on the effect of the pretreatment prior to anodizing on the anodic oxide film morphology. Though differences in chemical composition between AA1050 and AA1230 (clad layer of AA2024-T3) are very low, it is recommended to vary either the alloy or the pretreatment during experiments, and not both at the same time.

Voltage sweep rates

In this work, the fastest voltage sweep rate applied was 18V/min . Due to limitations of the power supply, the voltage could not be increased faster. Studying faster initial voltage sweeps might be interesting, since the outer surface diameter showed to be related to the initial voltage sweep rate in PSA. Also, it would be interesting to study the relation between voltage sweep rate (either at the beginning of the cycle or during a voltage step) and the recovery rate more in-depth.

Transmission Electron Microscopy (TEM)

For the analysis of anodic oxide films it is suggested to use Transmission Electron Microscopy (TEM) instead of Scanning Electron Microscopy (SEM) whenever possible. TEM has a higher resolution, which would make it possible to study film characteristics in further detail. Now, it was hard to measure the very small pore diameters ($\pm 10\text{nm}$) of SAA films, which should not be a problem with TEM. Also, the fine featured oxide structure which is expected to form during the voltage sweep can be better displayed with TEM.

Relation between film morphology and bond performance

The fundamental failure mechanisms of adhesive joints are not yet understood. Some first steps towards determining the adhesion and corrosion mechanisms have been taken in this work, but there is still a lot to be done. To fully understand the relation between the anodic film morphology and bond performance, it is necessary to use aluminum substrate material with a perfectly smooth surface in experiments. As such, it is avoided that deformed aluminum surface layers – caused by processing by the aluminum supplier – negatively influence the corrosion resistance of the bond. Electropolishing could be introduced in the experimental procedure to obtain perfectly smooth aluminum substrate material. Also, it is recommended to perform future experiments on the relation between morphology and bond performance in SAA rather than in PSA. Since the oxide dissolution rate is much lower in sulfuric acid than in phosphoric acid, it is easier to control oxide morphologies in SAA than in PSA. Optionally, post/etching steps and-or two step anodizing process could be used to create big pore size differences on one substrate.

REFERENCES

1. Wernick, S., R. Pinner, and P.G. Sheasby, *The surface treatment and finishing of aluminium and its alloys*. 5 ed. Vol. 1. 1987, Ohio and Middlesex: ASM International and Finishing Publications LTD.
2. Brockmann, W., et al., *Adhesion in bonded aluminium joints for aircraft construction*. International Journal of Adhesion & Adhesives, 1986. **6**.
3. Norseth, T., *The Carcinogenicity of Chromium*. Environmental Health Perspectives, 1981. **40**: p. 121-130.
4. Matz, C.W., et al. *Phosphoric Sulfuric Acid Anodizing (PSA) - a Heavy Metal Free Alternative for High Quality Surface Pretreatment of Aluminium*. in *Environmentally Compliant Surface Treatments of Materials for Aerospace Applications*. 1996. Florence, Italy.
5. Critchlow, G.W., et al., *Strategies for the replacement of chromic acid anodising for the structural bonding of aluminium alloys*. International Journal of Adhesion & Adhesives, 2005. **26**: p. 419-453.
6. Sheasby, P.G. and R. Pinner, *The surface treatment and finishing of aluminium and its alloys*. 6 ed. Vol. 1. 2001, UK: Finishing Publications Ltd.
7. Thompson, G.E., *Porous anodic alumina: fabrication, characterization and applications*. Thin Solid Films, 1997. **297**: p. 192-201.
8. O'Sullivan, J.P. and G.C. Wood, *Morphology and mechanism of formation of porous anodic films on aluminum*. Proceedings of the Royal Society of London Series A - Mathematical and Physical Sciences, 1970. **317**: p. 511-543.
9. Setoh, S. and A. Miyata, Sci. Pap. Inst. Phys. Chem. Res., 1932. **189**.
10. Keller, F., M.S. Hunter, and D.L. Robinson, *Structural features of oxide coatings on aluminum*. Journal of The Electrochemical Society, 1953. **100**: p. 411-419.
11. Rahman, M.M., et al., *Effect of the anodization voltage on the pore-widening rate of nanoporous anodic alumina*. Nanoscale Research Letters, 2012. **7**.
12. Huang, Y., et al., *Kinetic Models of Controllable Pore Growth of Anodic Aluminum Oxide Membrane*. Met. Mater. Int., 2012. **18**(3): p. 433-438.
13. Curioni, M., et al., *Optimization of anodizing cycles for enhanced performance*. Surface and Interface Analysis, 2013.
14. Curioni, M., P. Skeldon, and G.E. Thompson, *Anodizing of Aluminum under Nonsteady Conditions*. Journal of The Electrochemical Society, 2009. **156**(12): p. 407-413.
15. Ma, Y., et al., *Anodic Film Formation on AA 2099-T8 Aluminum Alloy in Tartaric-Sulfuric Acid*. Journal of The Electrochemical Society, 2011. **158**(2): p. C17-C22.
16. Exalto, R., *Anodizing in chromic acid - phosphoric acid solutions as pretreatment for adhesive bonding - third phase (7075-T6 clad)*. 1985, Fokker.
17. Ćurković, L., M. Fudurić, and S. Kurajica. *Kinetic study of the corrosion of alumina ceramics in sulphuric acid aqueous solution*. in *1st International Conference Corrosion and Material Protection*. 2007. Prag, Ceska.
18. Hoar, T.P. and N.F. Mott, *A mechanism for the formation of porous anodic oxide films on aluminium*. J. Phys. Chem. Solids, 1959. **9**: p. 97-99.
19. Oh, J. and C.V. Thompson, *The role of electric field in pore formation during aluminum anodization*. Electrochimica Acta, 2011. **56**: p. 4044-4051.

20. Ha, Y.-C. and D.-Y. Jeong, *Fast fabrication of a High-aspect-ratio, Self-ordered Nanoporous Alumina Membrane by Using High-field Anodization*. Journal of the Korean Physical Society, 2010. **57**(6): p. 1661-1666.
21. Hunter, M.S. and P. Fowle, *Factors Affecting the Formation of Anodic Oxide Coatings*. Journal of The Electrochemical Society, 1954. **101**(10): p. 514-519.
22. Yerokhin, A. and R.H.U. Khan, *Anodising of Light Alloys*, in *Surface Engineering of Light Alloys: Aluminium, Magnesium and Titanium Alloys*, H. Dong, Editor. 2010, Woodhead Publishing, Ltd.: Cambridge. p. 83-109.
23. Henley, V.F., *Anodic oxidation of aluminium and its alloys*. 1982, England: Pergamon Press.
24. New Zealand Institute of Chemistry. *Anodising of Aluminium*. [cited 2013 April 8th]; Available from: <http://nzic.org.nz/ChemProcesses/metals/8E.pdf>.
25. Zhou, F., *Growth mechanism of porous anodic films on aluminium*, in *Faculty of Engineering and Physical Sciences*. 2011, University of Manchester: Manchester.
26. Parkhutik, V.P. and V.I. Shershulsky, *Theoretical modelling of porous oxide growth on aluminium*. J. Phys. D: Appl. Phys, 1992. **25**: p. 1258-1263.
27. Paternarakis, G. and K. Moussoutzanis, *Transformation of porous structure of anodic alumina films formed during galvanostatic anodising of aluminium*. Journal of Electroanalytical Chemistry, 2011. **659**: p. 176-190.
28. Bengough and Stuart, *British patent number 223 994*. 1923.
29. Minford, J.D., *Handbook of aluminum bonding technology and data*. 1993, New York: Marcel Dekker.
30. Thrall, E.W. and R.W. Shannon, *Adhesive bonding of aluminium alloys*. 1985, New York: Marcel Dekker.
31. Kwakernaak, A., *Overview of candidate anodising processes for continuous surface treatment for structural bonding*. 2007, Adhesion Institute, Delft University of Technology: Delft.
32. The Boeing Company, *BAC 5632 Boric Acid - Sulfuric Acid Anodizing, Revision D*. 2004.
33. Yendall, K.A. and G.W. Critchlow, *Novel methods, incorporating pre- and post-anodising steps, for the replacement of the Bengough–Stuart chromic acid anodising process in structural bonding applications*. International Journal of Adhesion & Adhesives, 2009. **29**: p. 503-508.
34. Silvex Surface Technology. *Sulfuric Acid Anodizing*. [cited 2013 April 9th]; Available from: <http://www.silvexinc.com/anodizing/sulfuric-acid-anodizing.php>.
35. The Boeing Company. *Preferred Materials and Processes: Tankline Processes*. 2010 [cited 2013 April 10th]; Available from: <http://www.boeingsuppliers.com/environmental/chromic.html>.
36. Museux, F. and R. Theilmann, *Introducing more eco-efficient chemical treatments for aircraft structure*, in *Flight Airworthiness Support Technology; Airbus Technical Magazine*. 2009, Bruno Piquet: France. p. 2-9.
37. Koch, E., *Verfahren zur anodischen Oxidation*, E.P. Office, Editor. 1993, Erich Kock: Germany.
38. Carter, E.A., *High current anodization of magnesium and magnesium alloys*. 1996, The University of Auckland.

39. Guntherschultze, A. and H. Betz, *ElectrolytKondensatoran*. 2 ed. 1952, Berlin: Herbert Cram.
40. Lohrengel, M., *Thin anodic oxide layers on aluminum and other valve metals - high field regime*. Materials Science & Engineering R-Reports, 1993. **11**: p. 243-294.
41. Choi, J., *Fabrication of monodomain porous alumina using nanoimprint lithography and its applications*, in *Mathematisch-Naturwissenschaftlich-Technischen Fakultät*. 2003, Martin-Luther-Universität: Halle-Wittenberg.
42. Zhu, X.F., et al., *The study on oxygen bubbles of anodic alumina based on high purity aluminum*. Materials Letters, 2005. **59**(24-25): p. 3160-3163.
43. Zhu, X., et al., *Oxygen evolution and porous anodic alumina formation*. Materials Letters, 2008. **62**(24): p. 4038-4040.
44. Garcia-Vergara, S.J., et al., *A flow model of porous anodic film growth on aluminium*. Electrochim. Acta, 2006. **52**: p. 681-687.
45. Garcia-Vergara, S.J., et al., *Compositional evidence for flow in porous anodic alumina*. Electrochem. Soc., 2007. **154**: p. C540-C545.
46. Terryn, H., *Electrochemical investigation of AC electrograining of aluminium and its porous anodic oxidation*, in *Facultiet Toegepaste Wetenschappen, Dienst Metallurgie*. 1987, Vrije Universiteit Brussel: Brussel.
47. Hebert, K.R., et al., *Morphological instability leading to formation of porous anodic oxide films*. Nature Materials, 2012. **11**: p. 162-166.
48. Shimizu, K., et al., *Novel marker for the determination of transport numbers during anodic barrier oxide growth on aluminium*. Philosophical Magazine B: Physics of Condensed Matter; Electronic, Optical and Magnetic Properties, 1991. **64**(3): p. 345-353.
49. P.Skeldon, et al., *Mobile tracers: their use in understanding key features of anodic alumina film formation*. Philosophical Transactions - Royal Society of London, A, 1994. **348**(1687): p. 295-314.
50. Sulka, G.D., *Highly Ordered Anodic Porous Alumina Formation by Self-Organized Anodizing*, in *Nanostructured Materials in Electrochemistry*, A. Eftekhari, Editor. 2008, WILEY-VCH Verlag GmbH & Co.: Weinheim.
51. Ebihara, K., H. Takahashi, and M. Nagayama, *Structure and density of anodic films formed on aluminium in oxalic acid solutions*. J. Met. Finish Soc. Jpn, 1983. **34**: p. 548-554.
52. Schneider, M., et al., *Interplay between parameter variation and oxide structure of a modified PAA process*, in *Surface and Interface Analysis*. 2013, John Wiley & Sons, Ltd.
53. Ye, J., Q. Yin, and Y. Zhou, *Superhydrophilicity of anodic aluminum oxide films: From "honeycomb" to "bird's nest"*. Thin Solid Films, 2009. **517**: p. 6012-6015.
54. Terryn, H., J. Vereecken, and J. Landuyt, *Influence of Aluminium Pretreatment on the Growth of Porous Oxide Films*. Transactions of the Institute of Metal Finishing, 1990. **68**: p. 33-37.
55. Abdel Rahim, S.S., H.H. Hassan, and M.A. Amin, *Galvanostatic anodization of pure Al in some aqueous acid solutions Part I: Growth kinetics, composition and morphological structure of porous barrier-type anodic alumina films*. Journal of Applied Electrochemistry, 2002. **32**: p. 1257-1264.
56. Curioni, M., et al., *Graded Anodic Film Morphologies for Sustainable Exploitation of Aluminum Alloys in Aerospace*. Advanced Materials Research, 2008. **8**: p. 48-55.
57. Cheng, W., et al., *Tree-like alumina nanopores generated in a non-steady state anodization*. Journal of Materials Chemistry, 2007. **17**: p. 3493-3495.

58. Diggle, J.W., T.C. Downie, and C.W. Goulding, *Anodic oxide films on aluminum*. Chemical Review, 1969. **69**: p. 365-405.
59. Kim, Y.S., et al., *The effects of applied potential and pH on the electrochemical dissolution of barrier layer in porous anodic oxide film on pure aluminium*. Corrosion Science, 1996. **38**(2): p. 329-336.
60. Murphy, J.F., in *Symposium on Anodizing Aluminium*. 1967, Aluminium Federation: Birmingham. p. 3-16.
61. Takahashi, H., et al., *Electron microscopy of porous anodic oxide films on aluminium by ultrathin sectioning technique. Part I. The structural change of the film during the current recovery period*. J. Electron Microscopy, 1973. **22**(2): p. 149-157.
62. Airbus Industrie, *AIMS 03-04-014*. 1998, Airbus Industrie: Blagnac Cedex, France.
63. Aalco Metals Ltd, *Aluminium Alloy 1050 'O' (Soft)*. 2013: Cobham, Surrey.
64. Stokroos, I., et al., *A comparative study of thin coatings of Au/Pd, Pt and Cr produced by magnetron sputtering for FE-SEM*. Journal of Microscopy, 1998. **189**(1): p. 79-89.
65. Schutter, T.K., *Phosphoric-Sulphuric Acid Anodising of AA7075-T6 Clad*. 2004, Adhesion Institute, Delft University of Technology: Delft.
66. Arrowsmith, D.J., A.W. Clifford, and D.A. Moth, *Fracture of anodic oxide formed on aluminium in sulphuric acid*. Journal of Materials Science Letters, 1986. **5**: p. 921-922.
67. Booker, C.J.L., J.L. Wood, and A. Walsh, *Electron Micrographs from Thick Oxide Layers on Aluminium*. Nature, 1955. **176**: p. 222-223.
68. Wu, H. and K.R. Hebert, *Electrochemical transients during the initial moments of anodic oxidation of aluminum*. Electrochimica Acta, 2002. **47**: p. 1373-1383.
69. De Graeve, I., H. Terry, and G.E. Thompson, *AC-anodising of aluminum: Contribution to electrical and efficiency study*. Electrochimica Acta, 2006. **52**: p. 1127-1134.
70. Hasenay, D. and M. Šeruga, *The growth kinetics and properties of potentiodynamically formed thin oxide films on aluminium in citric acid solutions*. J Appl Electrochem, 2007. **37**: p. 1001-1008.
71. Dillard, D.A., *Fundamentals of stress transfer in bonded systems*, in *The Mechanics of Adhesion*, D.A. Dillard and A.V. Pocius, Editors. 2002.
72. Packham, D.E., *Theories of Fundamental Adhesion*, in *Handbook of Adhesion Technology*, L.F.M. Da Silva, A. Öchsner, and R.D. Adams, Editors. 2011, Springer-Verlag: Berlin Heidelberg.
73. McBain, J.W. and D.G. Hopkins, *On Adhesives and Adhesive Action*. The Journal of Physical Chemistry, 1925. **29**(2): p. 188-204.
74. Packham, D.E. *The mechanical theory of adhesion - A seventy year perspective and its current status*. in *First International Congress on Adhesion Science and Technology*. 1995. Amsterdam: VSP.
75. Deryagin, B.V. and N.A. Krotova, *Doklady Akademii Nauk SSSR*, 1948. **61**.
76. Voyutskii, S.S., *Autohesion and adhesion of high polymers*. 1963, New-York: Wiley Interscience.
77. Spadaro, C., C. Dispenza, and C. Sunseri, *Influence of nanoporous structure on mechanical strength of aluminium and aluminium alloy adhesive structural joints*. Journal of Physics: Condensed Matter, 2006. **18**: p. S2007-S2018.

78. Venables, J.D., et al., *Oxide morphologies on aluminium prepared for adhesive bonding*. Applications of Surface Science, 1979. **3**(1): p. 88-98.
79. Franz, H.E., *Karakterisierung von aluminium oxid Schichten*. Z. Werkstofftech., 1983. **14**: p. 290-298.
80. Venables, J.D., *Adhesion and durability of metal-polymer bonds*. Journal of Materials Science 1984. **19**(8): p. 2431-2453.
81. Kollek, H., *Chemical reactions on technical metal surfaces and their influence on adhesion*, in *Adhesion and adhesives: science, technology and application*.
82. Brockmann, W., *Untersuchungen von Adhäsionsvorgängen zwischen Kunststoffen und Metallen*. Adhesion, 1975. **1**.
83. Gent, A.N. and G.R. Hamed, *Science of Adhesion*. 1983, Ohio: Akron University.
84. Brand, J.v.d., *On the adhesion between aluminium and polymers*. 2004, Delft University of Technology: Delft.
85. Lunder, O., *Chromate-free pre-treatment of aluminium for adhesive bonding*, in *Department of Materials Technology*. 2003, Norwegian University of Science and Technology: Trondheim.
86. *ASM Specialty Handbook: Aluminum and Aluminum Alloys*, ed. J.R. Davis. 1993: ASM International.
87. Wyde, J.W. and J.K. Spelt, *Measurement of adhesive joint fracture properties as a function of environmental degradation*. International Journal of Adhesion & Adhesives, 1998. **18**(4).
88. Davis, J.R., ed. *ASM Specialty Handbook: Aluminum and aluminum alloys*. 1993, ASM International.
89. Kozma, L. and I. Olefjord, *Basic processes of surface preparation and bond formation of adhesively joined aluminum*. Materials Science and Technology, 1987. **3**.
90. Velterop, L., *Phosphoric sulphuric acid anodising: an alternative for chromic acid anodising in aerospace applications?* 2003, National Aerospace Laboratory (NLR).
91. Hexcel, *Redux 101 Safety Data Sheet*. 2008.
92. 3M, *Material Safety Data Sheet 3M Scotch-Weld Structural Adhesive Film AF 163-2*. 2011.
93. De Regt, P.A. and A. Van den Berg, *Phosphoric - Sulphuric Acid anodising (Exploratory phase)*. 2002, Adhesion Institute, Delft University of Technology: Delft.
94. Rolland, P., V.L. Carlino, and R. Vane, *Improved Carbon Analysis with Evactron Plasma Cleaning*, in *Microscopy and Microanalysis*. 2004: Savannah.
95. Ruggeri, R.T. and T.R. Beck, *An Analysis of Mass Transfer in Filiform Corrosion*. Corrosion, 1983. **39**(11): p. 452-465.
96. Bautista, A., *Filiform corrosion in polymer-coated metals*. Progress in Organic Coatings, 1996. **28**(1): p. 49-58.

Appendix 1

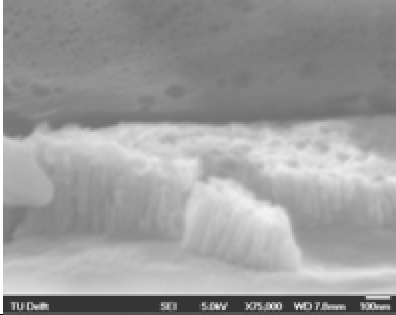
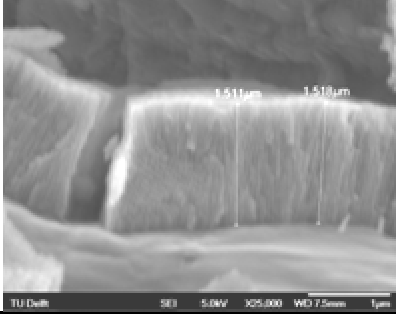
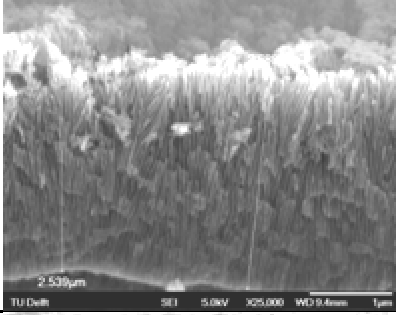
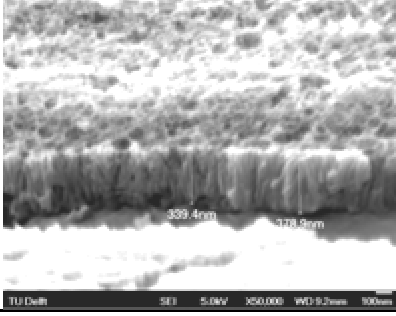
Average temperatures anodizing experiments

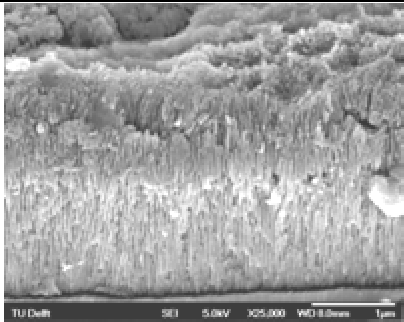
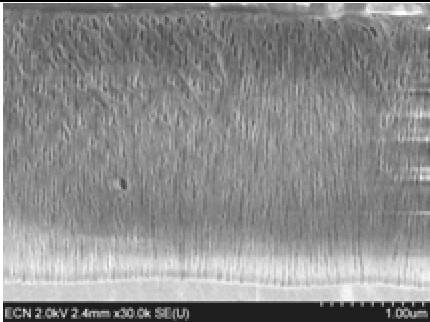
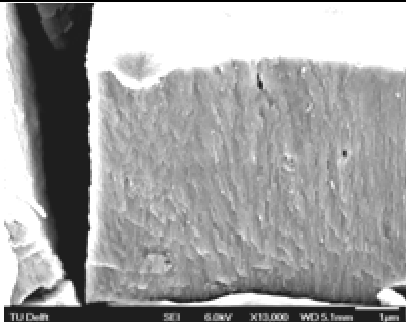
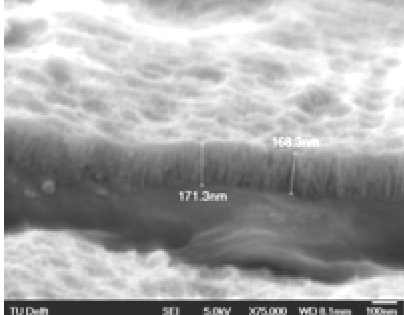
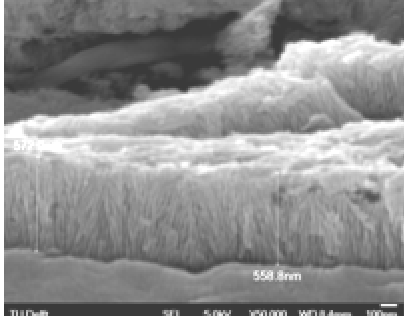
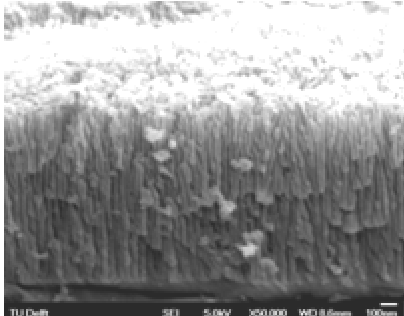
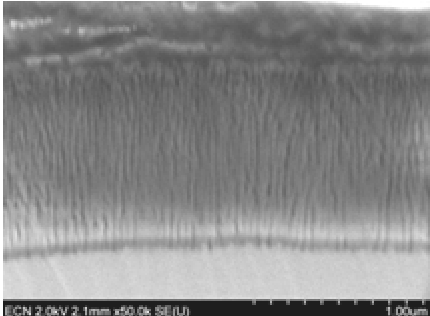
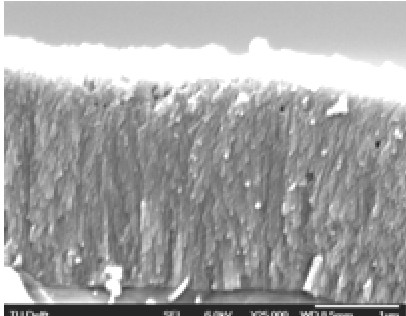
Voltage cycle nr.	Anodizing time (min)	Average temperature electrolyte (°C)		
		PSA AA1050	PSA AA2024- T3 clad	SAA AA1050
1	5	27,9	-	28,5
	15	28,0	-	27,9
	30	28,2	-	28,0
2	5	28,0	-	27,8
	15	unknown	-	27,9
	30	27,9	27,0	27,9
3	5	28,0	-	27,9
	15	27,9	-	27,9
	30	unknown	-	28,0
4	30	29,0	27,9	27,9
5	30	27,9	28,1	28,0
6	30	27,9	27,2	27,9
7	30	27,9	27,8	27,8

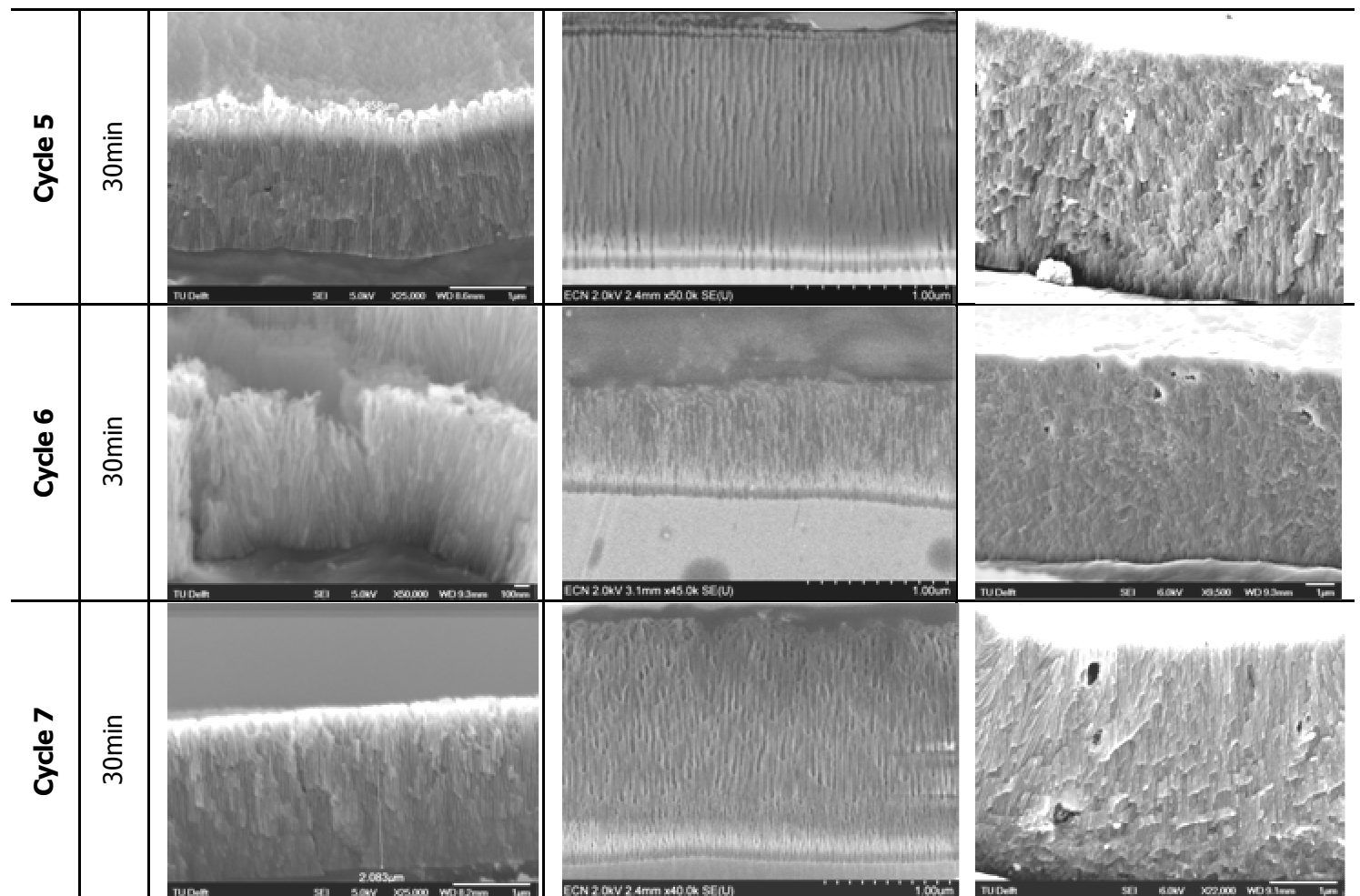
Appendix 2

SEM images anodic film cross sections

FE-SEM images of anodic oxide film cross sections. Magnification is indicated below each image. AA1050 cross sections are made by breaking the specimen, AA2024-T3 clad cross sections by ion milling.

Voltage cycle	Anodizing time	PSA AA1050	PSA AA2024-T3 clad	SAA AA1050
Cycle 1	5min		-	not available
	15min		-	not available
	30min		-	not available
Cycle 2	5min		-	not available

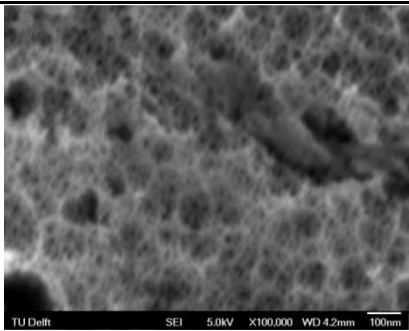
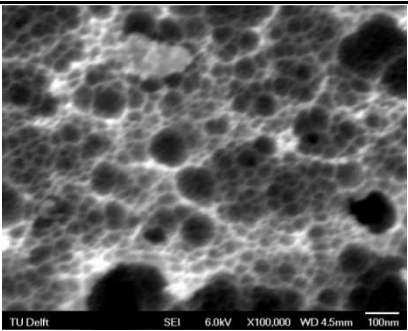
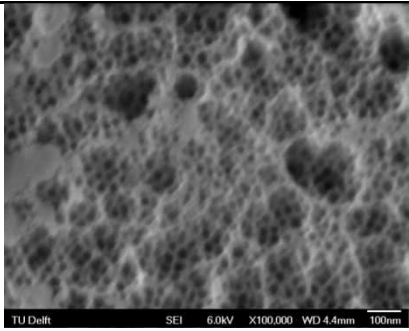
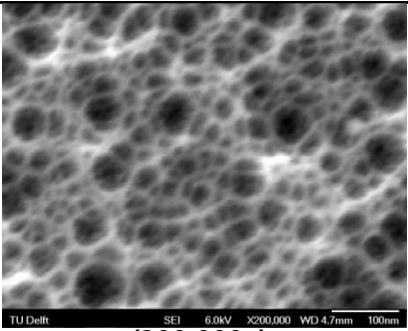
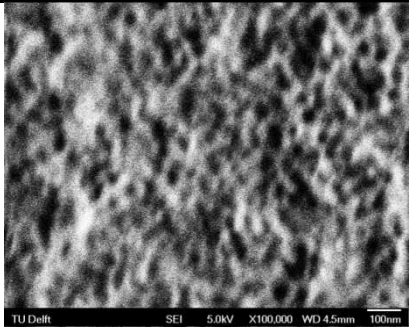
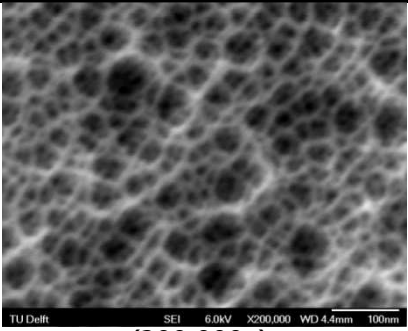
	15min	not available	-	not available
	30min			
Cycle 3	5min		-	not available
	15min		-	not available
	30min	not available	-	not available
Cycle 4	30min			

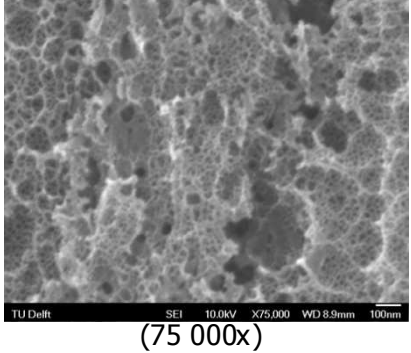
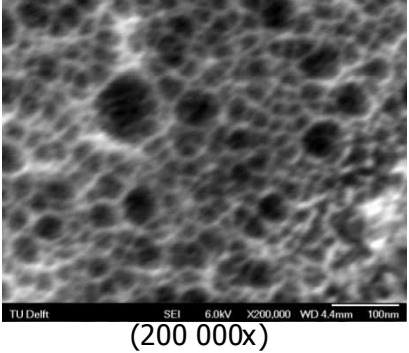
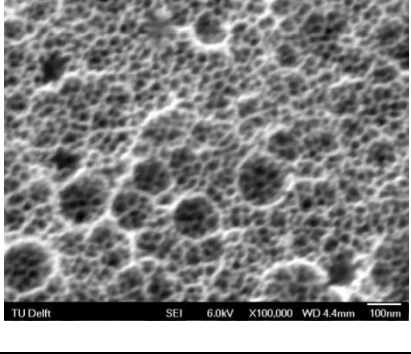
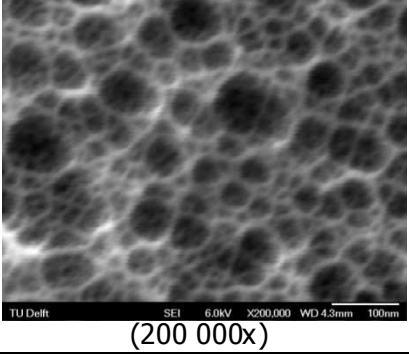
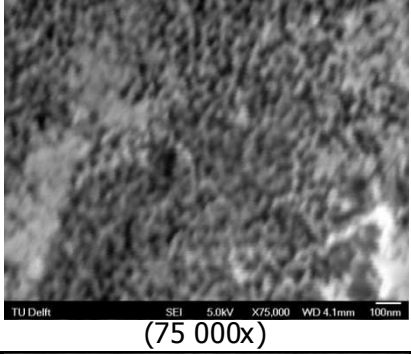
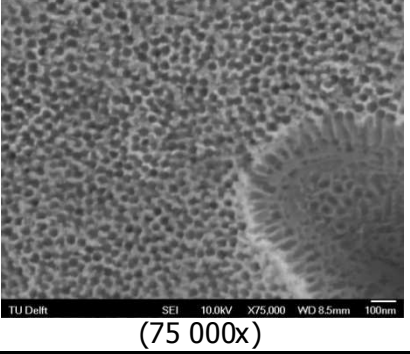
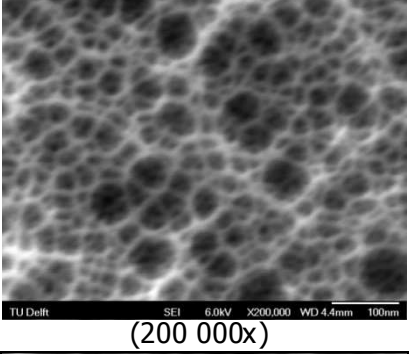
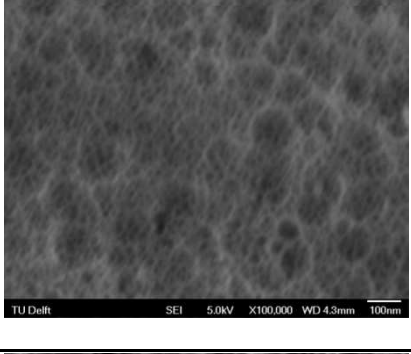
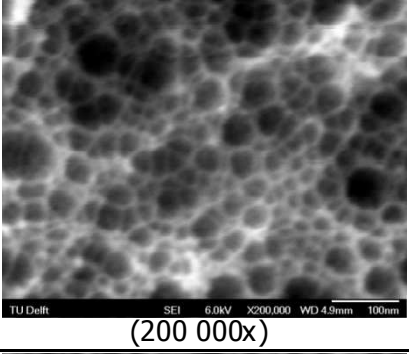
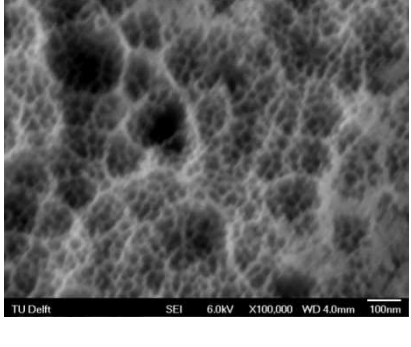
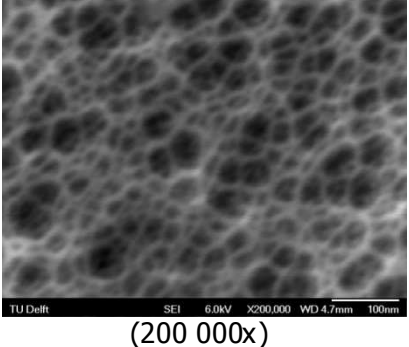


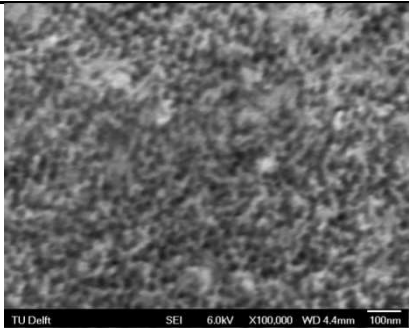
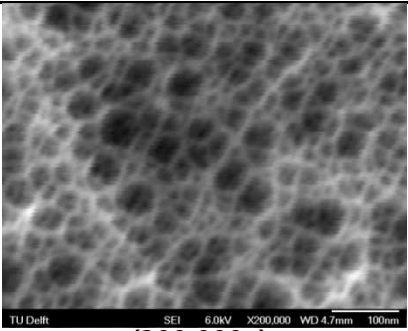
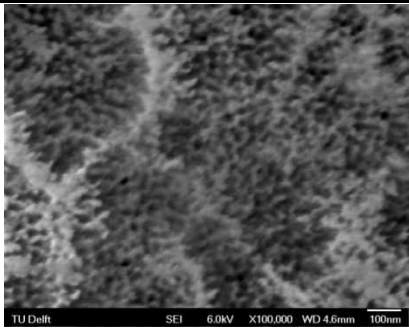
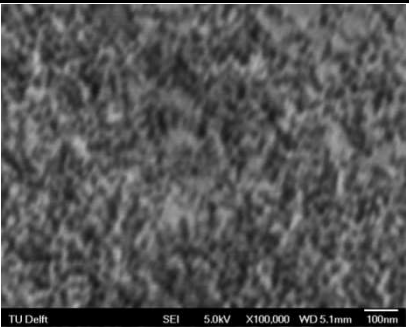
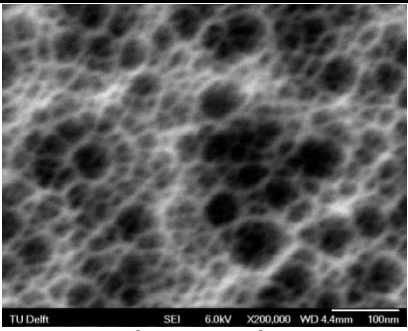
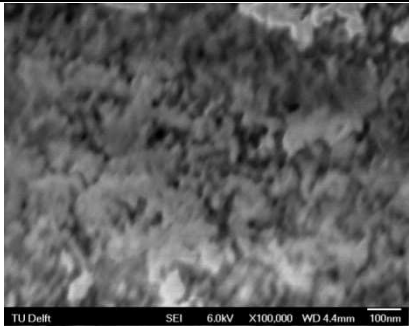
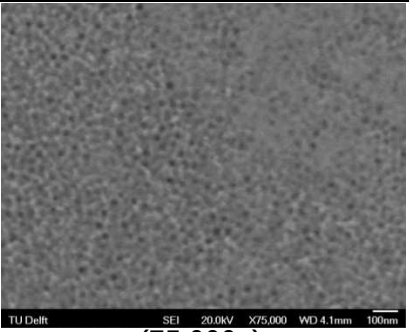
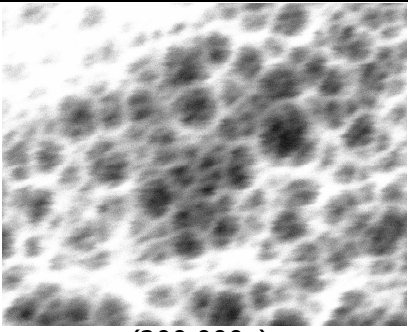
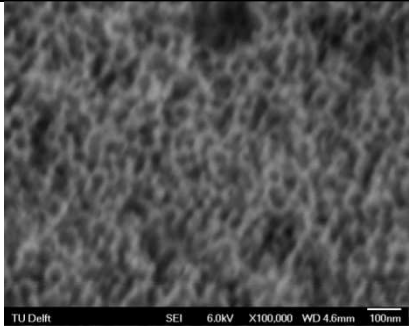
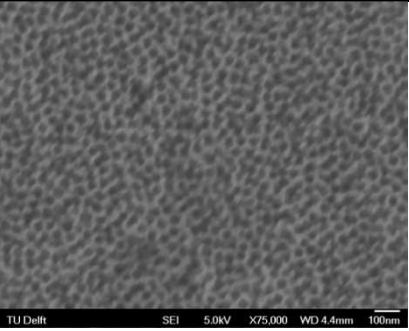
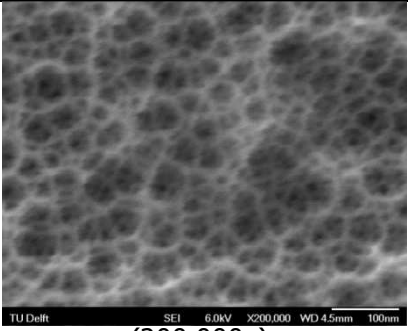
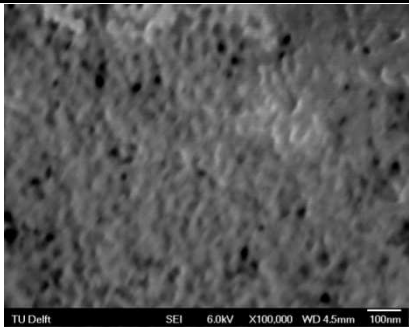
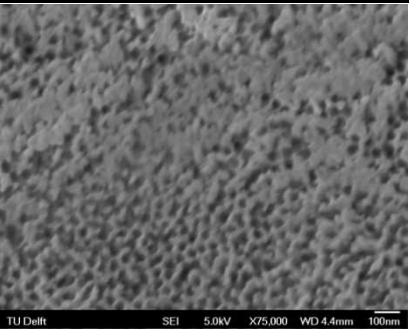
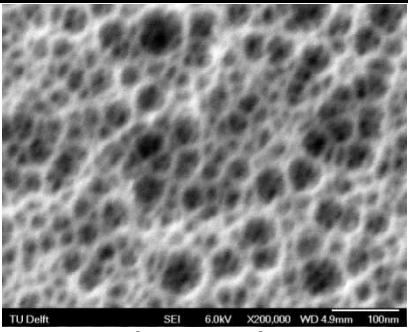
Appendix 3

SEM images anodic film outer surface

FE-SEM images of the outer surface of anodic oxide films. Magnification is 100 000x, unless indicated otherwise.

Voltage cycle Anodizing time		PSA AA1050	PSA AA2024-T3 clad	SAA AA1050
Cycle 1	5min		-	 (200 000x)
	15min		-	 (200 000x)
	30min		-	 (200 000x)

Cycle 2	5min		-	
	15min		-	
Cycle 2	30min			
Cycle 3	5min		-	
	15min		-	

	30min		-	 (200 000x)
Cycle 4	30min			 (200 000x)
Cycle 5	30min		 (75 000x)	 (200 000x)
Cycle 6	30min		 (75 000x)	 (200 000x)
Cycle 7	30min		 (75 000x)	 (200 000x)

